LAKEHEAD UNIVERSITY

ATTITUDE CONTROL OF A QUADROTOR UAV: EXPERIMENTAL RESULTS

by

Miaomiao Wang

Under the Supervision of Dr. Abdelhamid Tayebi

A Thesis Submitted in Partial Fulfillment of the Requirements
for the Degree of Master of Science
in Control Engineering

Lakehead University, Thunder Bay, Ontario, Canada

December 2015

Lakehead
U N I V E R S I T Y

FACULTY OF GRADUATE STUDIES

NAME OF STUDENT: Miaomiao Wang

DEGREE: Master's degree in Control Engineering

ACADEMIC UNIT: Engineering

TITLE OF THESIS: Attitude Control of a Quadrotor UAV: Experimental results

This thesis has been prepared

under my supervision and

the candidate has complied with

the Master's thesis process regulations.

_____

Signature of Supervisor

December 18, 2015

_____

Date

ABDELHAMID TAYEBI

Supervisor's Name (Printed) _____

Abstract

The quadrotor is a type of unmanned aerial vehicles (UAVs) which is gaining popularity over the past few years for its potential applications. Quadrotor UAVs are used, for instance, for surveillance, search and rescue missions, monuments inspection, and aerial photography. The crucial step towards a reliable application is the development of efficient attitude estimation and control algorithms. The primary focus of this thesis consists in investigating various attitude control techniques and their applications.

A nonlinear attitude estimator and a PD-like controller have been successfully implemented on a Quadrotor UAV. However, the stability proof of the attitude observer/controller combination is not obvious as the system is nonlinear. To solve this problem, an attitude controller directly relying on inertial vector measurements and angular velocity has been proposed. Some practical methods such as filtering and vector decoupling were developed and discussed. Moreover, an inertial measurements based velocity-free attitude controller has been designed.

Finally, real-time implementation has been conducted on a small-scale low-cost quadrotor UAV. Experimental results have been carried out to show the effectiveness of the proposed controllers and some experimental problems and further approaches of the velocity-free controller are discussed.

Acknowledgments

I sincerely thank my advisor, Dr. Abdelhamid Tayebi during my graduate studies at Lakehead University. He has proven to be an excellent supervisor and was always happy to share his considerable experience and knowledge. I want to thank him for his patience, support and guidance, and for instilling in me a genuine passion for control engineering.

I also thank my co-advisor Dr. Xiaoping Liu and his research team for fun memories and valuable research feedback. I want to thank my fellow graduate students Munir Enbaia and Kurtis W. Schram for their friendship and insights. I thank my undergraduate advisor and teammate, Prof. Housheng Su and Mrs Miaomiao Zhao for their continuous guidance and cooperation.

Finally, I would like to thank my wife, Caiping Zhang, for her love and understanding during our entire stay in Thunder Bay. I would also like to thank my family for their endless love and support.

Miaomiao Wang

Contents

List of Figures

List of Tables

List of Abbreviations

UAV	–	Unmanned Aerial Vehicle.
SVD	–	Singular Value Decomposition.
QUEST	–	Quaternion Estimation.
KF	–	Kalman Filter.
EKF	–	Extended Kalman Filter.
MEKF	–	Multiplicative Extended Kalman Filter.
AEKF	–	Additive Extended Kalman Filter.
GPS	–	Global Positioning System.
PID	–	Proportional Integral Derivative.
PD	–	Proportional Derivative.
LQR	–	Linear-Quadratic Regulator.
SE($\mathbf{3}$)	–	Special Euclidean group of dimension 3.
SO($\mathbf{3}$)	–	Special Orthogonal group of dimension 3.
FFT	–	Fast Fourier Transform.
DCM	–	Direction Cosine Matrix.
APM	–	ArduPilot Mega.
ADC	–	Analog-to-Digital Converter.
SPI	–	Serial Peripheral Interface.
I^{2}C	–	Inter-Integrated Circuit.
PWM	–	Pulse Width Modulation.
PPM	–	Pulse Position Modulation.
ESC	–	Electronic Speed Controller.
DC	–	Direct Current.
AC	–	Alternating Current.
EMF	–	Electro-Motive Force.
IGRF	–	International Geomagnetic Reference Field.
WMM	–	World Magnetic Model.
IMU	–	Inertial Measurement Unit.
DLPF	–	Digital Low Pass Filter.
LIPO	–	Lithium Polymer.

Chapter 1

Introduction

The quadrotor unmanned aerial vehicle (UAV) is a flying robotic vehicle without a human operator on board. The quadrotor has some interesting capabilities, such as vertical take-off and landing, hover capability, high maneuverability and agility. These advantages make the quadrotor ideally suited for many civilian and military applications.

Recent advances in electronics, microcontrollers and low-cost sensors have revived interest in the quadrotor among academic researchers and hobbyists. A lot of highly capable quadrotor platforms have begun to move out of university laboratories and into widespread commercial use, like photography and videography, for example Fig. 1.1 [1]. These models offer a ready-to fly solution that does not require the advanced knowledge in avionics and flight control systems from the operator. A reliable and robust quadrotor UAV platform is required to be sufficiently flexible for research use [1,2].

The main objective of this thesis is to develop a reliable and robust quadrotor platform and improve the performance of our quadrotor UAV by implementing advanced nonlinear attitude controllers.

(a) (b)

Figure 1.1: Quadrotors for photography and videography (a) DJI Phantom 3; (b) 3DR Solo

---

[1] DJI Phantom 3, www.dji.com; 3DR Solo, 3drobotics.com

1.1 Overview of Quadrotor UAV Control Approaches

Attitude estimation and attitude control are two main tasks associated with developing an autonomous quadrotor aerial robot. To control the flight of a quadrotor, in most of the cases, it is required to estimate the orientation of the quadrotor UAV. The estimated orientation is then used in the attitude control law. Recently developed attitude estimation algorithms and attitude controllers are briefly discussed in the remainder of this section.

1.1.1 Attitude Estimation

The development of reliable attitude estimation algorithms that can run on the low-cost computational hardware and low-cost sensing systems, is the key for the development of successful quadrotor UAVs. A number of attitude estimation/filtering techniques have been discussed in the literature [3, 4].

Theoretically, one of the easy ways is to integrate the rigid body attitude kinematics equations using angular velocity measurements data provided by gyroscopes. However, such a solution may diverge beyond a few hundred milliseconds because of the existence of noise and bias in the gyroscope measurements. An alternative way is to construct the attitude algebraically using inertial measurements [5]. Several attempts were proposed to solve the attitude reconstruction problem from inertial vector measurements as an optimization problem, known as Wahba's problem, such as QUEST algorithm [6], Singular Value Decomposition (SVD) [7] and their extensions. However, significant errors may be generated from imperfect measurements provided by accelerometers and magnetometers, and/or imprecise knowledge of the considered inertial vectors.

The emergence of Kalman Filter (EK) theory and its subsequent advantages in the real-time applications led to a broad class of attitude filtering methods for the aircraft systems. Kalman filtering is performed in two steps: the first step predicts the current state variables from the previous estimated variables based on the dynamics; another step updates the estimated state variables with the weighted predicted states and noisy sensor measurements. Since the attitude dynamics are nonlinear and the Kalman filter is originally designed for linear systems, extensions of the Kalman filter to nonlinear systems, known as Extended Kalman Filter (EKF) were proposed in [8–10]. Nevertheless, poor performances or even divergence arising from the real-time linearization in the EKF have led to the development of Multiplicative EKF (MEKF) [11] and Additive EKF (AEKF) [12]. Various versions of the Kalman filter have proven their effectiveness in real-time applications. However, the main drawback is their computational complexity and the fact that it is difficult to prove closed-loop stability.

In recent decades, a class of new and powerful techniques relying on nonlinear observers have brought new hopes for the attitude estimation problem [13–23]. There are some significant advantages of the nonlinear observers compared to Kalman-like filtering techniques, such as rigorous stability proofs and strong mathematical arguments for their performance. Moreover, some of the nonlinear attitude observers have been successfully implemented

on low-cost microprocessors using the rotation matrix representation [15, 18, 19], and unit quaternion representation [17, 22, 23]. A common assumption used in the design of attitude observers, using inertial vector measurements, is that the accelerometer measures the gravity vector in the body frame (see, for instance, [15, 18, 20]). This assumption is realistic in near-hover operations (*i.e.,* low translational accelerations). However, in the case of relatively high translational accelerations, the accelerometer does not measure the gravity vector anymore, and the attitude estimators, relying on the above mentioned assumption, are not guaranteed to provide a reliable estimated attitude. To overcome this problem, an alternative attitude observer, known as velocity-aided observer, relying on some additional measurements (such as the linear velocity obtained from a GPS) has been proposed in the literature (*e.g.,* [22]). Another problem that has been dealt with in the literature is the attitude estimation with gyro-bias [15, 18, 20, 23]. Another issue in practical applications, is that the magnetometer readings can be affected by the magnetic fields generated by motors, as well as other magnetic fields generated by other electrical equipments in the environment. To solve this problem, a vector decoupling strategy has been proposed in [20] and [24] to locally remove the disturbances of the magnetometers from the estimation dynamics of the roll and pitch. In [23], the authors extended the results to global vector decoupling and fully tested the estimation algorithm in real-time applications. This modification shows that the global vector decoupling estimation algorithm improved the overall quality of the nonlinear attitude estimators. However, only almost-global stability and local exponential stability have been achieved. The issue of global stability for attitude nonlinear estimation algorithms has remained unsolved in the literature.

1.1.2   Attitude Control

For autonomous quadrotor UAV control, one of the most important parts is to design efficient attitude stabilization and/or attitude tracking schemes. Many control techniques have been proposed in the literature, see for instance [25–27] and the references therein.

One of the widely used methods known as the Proportional-Integral-Derivative (PID) controller has been implemented in [28] and [29]. However, the PID controller, as well as other linear controllers such as LQR [30], fail to work while dealing with aggressive maneuvers or large attitude errors, since the stability of these methods is only guaranteed in a restricted domain. Another approach has been proposed by introducing a decomposition of the quadrotor system into an outer-loop for attitude control and an inner-loop for body rates control [1] and [31], while the frequency of the inner-loop system is much higher than that of the outer-loop system. This approach has been successfully implemented in the real-time quadrotor systems. The main advantage of this approach is that the process of the controller design is simplified. Similarly, it is not easy to show the stability of the overall system and the stability of each subsystem is only guaranteed in a restricted domain.

Various nonlinear control methods, such as feedback linearization, backstepping and sliding mode control have been proposed in the literature [32–36]. However, only ideal dynamics without considering aerodynamics effects and sensor measurements were studied and only simulation results were presented. In [37–39], some practical nonlinear controllers

with experimental results have been proposed. For example, a nonlinear PID-like controller designed directly on SE(3) for quadrotor UAV was tested in [38]. In [37], the authors proposed a nonlinear control scheme based on Euler angles using a backstepping-like linearization method. However, in order to cancel the nonlinear terms in the time derivative of the Lyapunov function candidate, the control law requires the information of model parameters like moment of inertia. In [39], a new quaternion-based PD-like feedback control scheme was proposed for quadrotor stabilization. The PD feedback structure involves vector quaternion and angular velocity without any system model parameters, which is known as a model-independent controller. The proposed PD-like controller guarantees almost global asymptotic stability.

The attitude control problem, with full state feedback (*i.e.,* attitude and angular velocity) is well understood in the literature. Another performance and implementation-cost optimization issue that arises is to design an attitude controller without angular velocity. Several attempts have been made by introducing an observer-like passive system to reconstruct the angular velocity in [40–43]. Even though, these control algorithms do not directly involve the angular velocity, the latter is required to construct the attitude in the attitude estimation algorithms. In [44], a true velocity-free attitude controller was firstly proposed based on inertial measurements and the unwinding phenomenon was avoided. The authors in [45–47] improved the result by introducing a modified observer-like passive system based on inertial measurements, which reduces the set of unstable equilibria. However, some practical issues related to these angular velocity-free attitude control schemes, in the presence of measurement noise, will be discussed later.

1.2   Thesis Contribution

The thesis contributions are as follows:

- Improved the parameter identification of moments of inertia in Chapter 3 by using the attitude estimation algorithm proposed in [23] to collect the oscillation data around the roll, pitch and yaw axes, respectively. The Fast Fourier Transform (FFT) has been applied to find the natural frequencies of the oscillation tests.

- Implemented a PD-like unit quaternion based nonlinear attitude controller (proposed in [39]) in Chapter 4. The orientation of the quadrotor was estimated by a nonlinear attitude estimation algorithm proposed in [23]. Indoor flying testing results of the quadrotor UAV have been presented.

- Implemented an inertial measurements based attitude controller for indoor real-time testing of the quadrotor UAV in Chapter 5. The technique of vector decoupling was introduced to improve the performance of the quadrotor stabilization.

- Analyzed the implementation issues of inertial measurements based velocity-free controller proposed in [44] (see Chapter 6). Some linear dynamic analysis techniques have been applied to study the performance of the control scheme.

1.3 Thesis Outline

This thesis is divided into 7 chapters. Chapter 1 provides an introduction to quadrotor UAVs, attitude estimation and attitude control.

Chapter 2 consists of a collection of mathematical background used throughout the rest of this thesis. Chapter 3 gives a detailed description of the quadrotor hardware setup, parameter identification and useful calibration techniques. A PD-like unit quaternion based attitude controller has been implemented in Chapter 4, with a non-linear attitude estimation algorithm. In Chapter 5, we developed an inertial measurements based attitude controller with vector filtering and vector decoupling techniques. Chapter 6 provides a detailed discussion about the implementation issues of the inertial measurements based velocity-free controller.

Finally, Chapter 7 summarizes the work in this thesis and provides some suggestions for future possible research work.

Chapter 2

Background and Preliminaries

2.1 Attitude Representations

When describing the rotational motion of the quadrotor, or more generally any rigid body, it is often needed to known the orientation with respect to a reference frame attached to the Earth, the Sun, or other stars. The aim of this section is to review some commonly used attitude parameterizations (see [48] for more details).

As show in Fig. 2.1, let $\mathcal{I}$ denote the inertial (fixed) frame and $\mathcal{B}$ denote the body-attached frame. The inertial frame is commonly attached to the Earth with the unit vector $\hat{z}_{\mathcal{I}}$ orthogonal to the ground and the unit vector $\hat{x}_{\mathcal{I}}$ pointing to the North direction. The body frame is attached to the quadrotor with the unit vector $\hat{z}_{\mathcal{B}}$ orthogonal to the platform and the unit vector $\hat{x}_{\mathcal{B}}$ pointing to the forward direction.
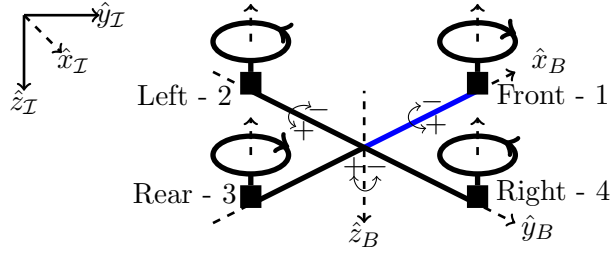

Figure 2.1: Quadrotor model with the inertial frame and body-attached frame

2.1.1 Euler Angles Representation

The Euler angles, introduced by Leonard Euler, are designed to describe the attitude of reference frame relative to inertial frame by three successive rotation (Euler) angles about the body fixed axes. The orientation of a rigid body in three dimensional Euclidean space

7

is given by

$$(\phi, \, \theta, \, \psi) \, (rad) \tag{2.1}$$

where, the three parameters (ϕ, θ, ψ) are known as roll, pitch and yaw, respectively.

Euler angles are the classical minimum parameter attitude representation, and they are easy to visualize because of their clear physical definitions. However, there exists an inherent problem in the Euler angles representation known as the singularity problem. The Euler angles encounter singularity for $\theta = \pm k\pi$, where k is any integer $(k = 1, 2, \cdots)$. This geometric singularity further induces the singularity in the corresponding Euler angles kinematic differential equations [49].

2.1.2 Rotation Matrix Representation

The rotation matrix, also known as the Direction Cosine Matrix (DCM), is the most popular representation of the attitude of a rigid body. Consider the orientation of frame $\mathcal{B}$ with respect to the inertial frame $\mathcal{I}$. It can be described by three vectors:

$$^{\mathcal{I}}\hat{X}_{\mathcal{B}} = \begin{pmatrix} \hat{x}_{\mathcal{B}} \cdot \hat{x}_{\mathcal{I}} \\ \hat{y}_{\mathcal{B}} \cdot \hat{x}_{\mathcal{I}} \\ \hat{z}_{\mathcal{B}} \cdot \hat{x}_{\mathcal{I}} \end{pmatrix} \quad ^{\mathcal{I}}\hat{Y}_{\mathcal{B}} = \begin{pmatrix} \hat{x}_{\mathcal{B}} \cdot \hat{y}_{\mathcal{I}} \\ \hat{y}_{\mathcal{B}} \cdot \hat{y}_{\mathcal{I}} \\ \hat{z}_{\mathcal{B}} \cdot \hat{y}_{\mathcal{I}} \end{pmatrix} \quad ^{\mathcal{I}}\hat{Z}_{\mathcal{B}} = \begin{pmatrix} \hat{x}_{\mathcal{B}} \cdot \hat{z}_{\mathcal{I}} \\ \hat{y}_{\mathcal{B}} \cdot \hat{z}_{\mathcal{I}} \\ \hat{z}_{\mathcal{B}} \cdot \hat{z}_{\mathcal{I}} \end{pmatrix}$$

where, $\hat{x}_{\mathcal{I}}, \hat{y}_{\mathcal{I}}$ and $\hat{z}_{\mathcal{I}}$ are the coordinate vectors attached to the frame $\mathcal{I}$, $\hat{x}_{\mathcal{B}}, \hat{y}_{\mathcal{B}}$ and $\hat{z}_{\mathcal{B}}$ are the coordinate vectors attached to the frame $\mathcal{B}$, and $^{\mathcal{I}}\hat{X}_{\mathcal{B}}, {}^{\mathcal{I}}\hat{Y}_{\mathcal{B}}$ and $^{\mathcal{I}}\hat{Z}_{\mathcal{B}}$ are unit vectors and orthogonal to each other. $u \cdot v = \|u\|\|v\| \cos \vartheta$ represents the dot product and ϑ is the angle between the vectors u and v. The rotation matrix of frame $\mathcal{B}$ with respect to frame $\mathcal{I}$ is defined as

$$^{\mathcal{I}}_{\mathcal{B}}R = \begin{pmatrix} ^{\mathcal{I}}\hat{X}_{\mathcal{B}}^{\top} & ^{\mathcal{I}}\hat{Y}_{\mathcal{B}}^{\top} & ^{\mathcal{I}}\hat{Z}_{\mathcal{B}}^{\top} \end{pmatrix} = \begin{pmatrix} \hat{x}_{\mathcal{B}} \cdot \hat{x}_{\mathcal{I}} & \hat{y}_{\mathcal{B}} \cdot \hat{x}_{\mathcal{I}} & \hat{z}_{\mathcal{B}} \cdot \hat{x}_{\mathcal{I}} \\ \hat{x}_{\mathcal{B}} \cdot \hat{y}_{\mathcal{I}} & \hat{y}_{\mathcal{B}} \cdot \hat{y}_{\mathcal{I}} & \hat{z}_{\mathcal{B}} \cdot \hat{y}_{\mathcal{I}} \\ \hat{x}_{\mathcal{B}} \cdot \hat{z}_{\mathcal{I}} & \hat{y}_{\mathcal{B}} \cdot \hat{z}_{\mathcal{I}} & \hat{z}_{\mathcal{B}} \cdot \hat{z}_{\mathcal{I}} \end{pmatrix}$$

The rotation matrix belongs to the *special orthogonal group* of dimension three $\mathsf{SO}(3)$. Let $R \in \mathsf{SO}(3)$ be a rotation matrix, then one has that

$$R^{\top}R = RR^{\top} = I_3 \quad \det(R) = 1$$

where, I_3 is the 3×3 identity matrix. We restrict our analysis to $\det(R) = 1$, since rotation matrices for which $\det(R) = -1$ are not rigid-body transformations [50]. Assume that R denotes a rotation from the inertial frame $\mathcal{I}$ to the body-attached frame $\mathcal{B}$. Let $v_{\mathcal{I}} \in \mathbb{R}^3$ be the coordinates of a vector attached in the frame $\mathcal{I}$, then the coordinates of this vector expressed in the frame $\mathcal{B}$ are given by

$$v_{\mathcal{B}} = R^{\top}v_{\mathcal{I}}$$

where $v_{\mathcal{B}} \in \mathbb{R}^3$. The rotation matrix allows for easy computation of multiple rotations through simple matrix multiplication.

2.1.3 Unit Quaternion Representation

Another representation of the attitude of a rigid body is the unit quaternion, which is defined as

$$Q = \begin{pmatrix} \eta \\ q \end{pmatrix}, \qquad (\eta^2 + q^\top q = 1) \tag{2.2}$$

where, $\eta \in \mathbb{R}$ and $q \in \mathbb{R}^3$ are the scalar part and the vector part of the quaternion, respectively. The unit quaternion can also be written as

$$Q = \begin{pmatrix} \cos(\varphi/2) \\ \sin(\varphi/2)\hat{k} \end{pmatrix} \tag{2.3}$$

which represents a rotation by an angle φ about an arbitrary unit vector $\hat{k}$. The unit quaternion belongs to the set of unit quaternions given by

$$\mathbb{Q} = \{Q \in \mathbb{R}^4 \mid \ |Q| = 1\} \tag{2.4}$$

Define two unit quaternions Q_1 and Q_2 as:

$$Q_1 = \begin{pmatrix} \eta_1 \\ q_{v1} \end{pmatrix} \quad Q_2 = \begin{pmatrix} \eta_2 \\ q_{v2} \end{pmatrix}$$

Then, the quaternion multiplication is given by

$$Q_1 \odot Q_2 = \begin{pmatrix} \eta_1\eta_2 - q_{v1}^\top q_{v2} \\ \eta_1 q_{v2} + \eta_2 q_{v1} + q_{v1} \times q_{v2} \end{pmatrix} \tag{2.5}$$

where, $\odot$ denotes the quaternion product and $\times$ denotes the vector cross product. The unit quaternion multiplication is non-commutative, since the cross product is non-commutative. The inverse of a unit quaternion Q is given by

$$Q^{-1} = \begin{pmatrix} \eta \\ -q \end{pmatrix} \tag{2.6}$$

and one has

$$Q \odot Q^{-1} = Q^{-1} \odot Q = Q_I = \begin{pmatrix} 1 \\ 0 \\ 0 \\ 0 \end{pmatrix} \tag{2.7}$$

where Q_I is the identity quaternion, which can be viewed as a rotation by a zero angle about an arbitrary unit vector. The unit quaternion multiplication can also be used to transform a vector from one reference frame to another. Let $v_\mathcal{I} \in \mathbb{R}^3$ be a vector in the inertial frame $\mathcal{I}$ and $v_\mathcal{B} \in \mathbb{R}^3$ be a vector projection of $v_\mathcal{I}$ in the body-attached frame $\mathcal{B}$. Then

$$\begin{pmatrix} 0 \\ v_\mathcal{B} \end{pmatrix} = Q^{-1} \odot \begin{pmatrix} 0 \\ v_\mathcal{I} \end{pmatrix} \odot Q \tag{2.8}$$

where, Q represents the attitude of the body frame. The quaternion representation has some advantages over the other attitude representations. Its reduced number of parameters makes it more suitable for real-time implementations. The main drawback of the quaternion representation is its non-uniqueness. In particular, this is a twofold covering map, where there exist a pair of antipodal unit quaternions $\pm Q \in \mathbb{Q}$ for each attitude $R \in \mathsf{SO}(3)$. Without careful designing, quaternion-based controllers may cause undesirable phenomena such as unwinding [51].

2.1.4 Comparison of the Attitude Representations

From the above discussion, we can conclude that each attitude representation has its own advantages and disadvantages. The comparison of the above attitude representations is given by Table 2.1 (see [**?**] for more details).

Representation	Parameters	Global	Unique
Euler Angles	3 parameters	No	No
Quaternion	4×1 unit vector	Yes	No
Rotation Matrix	3×3 Matrix	Yes	Yes

Table 2.1: Comparison of attitude representations

In practical applications, different attitude representations may be combined for specific requirements. Some useful equalities used in the remainder of the thesis are presented as follows:

- *Unit Quaternion and Euler Angles*
  The unit-quaternion can be generated by the Euler angles as follows:

$$Q = \begin{pmatrix} \eta \\ q \end{pmatrix} = \begin{pmatrix} c(\phi/2)c(\theta/2)c(\psi/2) + s(\phi/2)s(\theta/2)s(\psi/2) \\ s(\phi/2)c(\theta/2)c(\psi/2) - c(\phi/2)s(\theta/2)s(\psi/2) \\ c(\phi/2)s(\theta/2)c(\psi/2) + s(\phi/2)c(\theta/2)s(\psi/2) \\ c(\phi/2)c(\theta/2)s(\psi/2) - s(\phi/2)s(\theta/2)c(\psi/2) \end{pmatrix} \tag{2.9}$$

  with c and s denoting the cosine and sine operators. The quaternion can also be converted to Euler angles as follows:

$$\begin{pmatrix} \phi \\ \theta \\ \psi \end{pmatrix} = \begin{pmatrix} \text{atan2}(2(\eta q_1 + q_2 q_3), 1 - 2(q_1^2 + q_2^2)) \\ \arcsin(2(\eta q_2 - q_3 q_1)) \\ \text{atan2}(2(\eta q_3 + q_1 q_2), 1 - 2(q_2^2 + q_3^2)) \end{pmatrix} \tag{2.10}$$

  where, $\text{atan2}(\cdot) : \mathbb{R} \times \mathbb{R} \rightarrow (-\pi, \pi]$ denotes the four-quadrant inverse tangent. It is easy to check that $Q = Q_I$ for $\phi = 0, \theta = 0$ and $\psi = 0$.

- *Rotation Matrix and Euler Angles*
  The function that maps a vector of Euler angles to its rotation matrix from $(x - y - z)$ is given by

$$R = R_x(\phi)R_y(\theta)R_z(\psi) = \begin{pmatrix} c\theta c\psi & s\phi s\theta c\psi - c\phi s\psi & c\phi s\theta c\psi + s\phi s\psi \\ c\theta s\psi & s\phi s\theta s\psi + c\phi c\psi & c\phi s\theta s\psi - s\phi c\psi \\ -s\theta & s\phi c\theta & c\phi c\theta \end{pmatrix} \tag{2.11}$$

  where $R_x(\phi)$, $R_y(\theta)$ and $R_z(\psi)$ denote rotations around the x, y and z axes by angles ϕ, θ and ψ, respectively.

$$R_x(\phi) = \begin{pmatrix} 1 & 0 & 0 \\ 0 & c\phi & -s\phi \\ 0 & s\phi & c\phi \end{pmatrix} \quad R_y(\theta) = \begin{pmatrix} c\theta & 0 & s\theta \\ 0 & 1 & 0 \\ -s\theta & 0 & c\theta \end{pmatrix} \quad R_z(\psi) = \begin{pmatrix} c\psi & -s\psi & 0 \\ s\psi & c\psi & 0 \\ 0 & 0 & 1 \end{pmatrix}$$

  where, it is easy to check that $R = R_x(0)R_y(0)R_z(0) = I_3$

- *Unit Quaternion and Rotation Matrix*
  The rotation matrix is related to the unit-quaternion through the Rodriguez formula $R = \mathcal{R}(Q)$ [48]. The mapping $\mathcal{R} : \mathbb{Q} \to \mathsf{SO}(3)$ is given by

$$\mathcal{R}(Q) = I_3 + 2\eta S(q) + 2S(q)^2 = (\eta^2 - q^\top q)I_3 + 2qq^\top + 2\eta S(q) \qquad (2.12)$$

  where, $S : \mathbb{R}^3 \to \mathfrak{so}(3)$, and

$$S(x) = \begin{bmatrix} 0 & -x_3 & x_2 \\ x_3 & 0 & -x_1 \\ -x_2 & x_1 & 0 \end{bmatrix}$$

  with $x = [x_1, x_2, x_3]^\top$, and $\mathfrak{so}(3) = \{S \in \mathbb{R}^{3\times3} \mid S^\top = -S\}$ denotes the set of 3×3 skew symmetric matrices. Given a rotation matrix R and two vectors $x, y \in \mathbb{R}^3$, we have the following useful properties: $S(x)y = -S(y)x = x \times y$, $S(x)x = 0, S(x)S(y) = yx^\top - (x^\top y)I_3$, $S(S(x)y) = S(x)S(y) - S(y)S(x) = yx^\top - xy^\top$ and $S(Rx) = RS(x)R^\top$. The rotation matrix (2.12) can be further expanded in a matrix form as

$$\mathcal{R}(Q) = \begin{pmatrix} 1 - 2(q_2^2 + q_3^2) & 2(q_1q_2 - \eta q_3) & 2(\eta q_2 + q_1q_3) \\ 2(q_1q_2 + \eta q_3) & 1 - 2(q_1^2 + q_3^2) & 2(q_2q_3 - \eta q_1) \\ 2(q_1q_3 - \eta q_2) & 2(\eta q_1 + q_2q_3) & 1 - 2(q_1^2 + q_2^2) \end{pmatrix}$$

  where, it is easy to check that $\mathcal{R}(Q_I) = I_3$.

  Note that the quaternion representation is an over parameterization of the rotation space $\mathsf{SO}(3)$, which means that the mapping from $\mathsf{SO}(3)$ to $\mathbb{Q}$ is not a one-to-one mapping. There are two unit quaternions Q and $-Q$ (not Q^{-1}) represent the same rotation matrix R (*i.e.*, $\mathcal{R}(Q) = \mathcal{R}(-Q)$).

2.2 Dynamic Model of the Quadrotor UAV

The general motion of a quadrotor UAV in space is a combination of translational and rotational motions. The dynamical model of a quadrotor described in [52] and [39] is given by

$$\dot{p} = v \qquad (2.13)$$

$$\dot{v} = ge_3 - \frac{1}{m}\mathcal{T}Re_3 \qquad (2.14)$$

$$\dot{R} = RS(\omega) \qquad (2.15)$$

$$I_f\dot{\omega} = -\omega \times I_f\omega - G_a + \tau \qquad (2.16)$$

$$I_r\dot{\varpi}_i = \tau_i - Q_i, \quad i \in \{1, 2, 3, 4\} \qquad (2.17)$$

where

$p \in \mathbb{R}^3$: position of the origin of the airframe (frame $\mathcal{B}$) with respect to the frame $\mathcal{I}$,

$v \in \mathbb{R}^3$: linear velocity of the quadrotor expressed in frame $\mathcal{I}$,

$m \in \mathbb{R}$: mass of the quadrotor,

$g \in \mathbb{R}$: acceleration of the quadrotor due to gravity,

$e_3 = [0, 0, 1]^\top \in \mathbb{R}^3$: unit vector expressed in frame $\mathcal{I}$,

$\mathcal{T} \in \mathbb{R}$: total thrust generated by the four motors,

$R \in \mathsf{SO}(3)$: orientation of the airframe,

$\omega \in \mathbb{R}^3$: angular velocity of quadrotor expressed in the body-fixed frame $\mathcal{B}$,

$I_f \in \mathbb{R}^{3 \times 3}$: symmetric positive-definite constant inertial matrix around the center of mass expressed in frame $\mathcal{B}$,

$\tau \in \mathbb{R}^3$: airframe torque generated by the rotors,

$\varpi_i \in \mathbb{R}$: angular velocity of the motor i,

$\tau_i \in \mathbb{R}$: torque produced by the motor i,

$I_r \in \mathbb{R}$: the moment of inertia of the motor i,

The gyroscopic torque G_a generated by the combination of the rotations of the airframe and the four rotors, is give by

$$G_a := \sum_{i=1}^{4} (-1)^{i+1} I_r (\omega \times e_3) \varpi_i$$

The reactive torque Q_i generated by the motor i due to rotor drag, in free air, is given by

$$Q_i := -\kappa \varpi_i^2$$

where, κ is a positive coefficient. The airframe torques $\tau = [\tau_\phi, \tau_\theta, \tau_\psi]^\top$ and total thrust $\mathcal{T}$ generated by the rotors are given by

$$
\begin{align}
\tau_\phi &= db(\varpi_2^2 - \varpi_4^2) \tag{2.18} \\
\tau_\theta &= db(\varpi_1^2 - \varpi_3^2) \tag{2.19} \\
\tau_\psi &= \kappa(\varpi_2^2 + \varpi_4^2 - \varpi_1^2 - \varpi_3^2) \tag{2.20} \\
\mathcal{T} &= b(\varpi_1^2 + \varpi_2^2 + \varpi_3^2 + \varpi_4^2) \tag{2.21}
\end{align}
$$

where, b is a positive coefficient and d is the distance between the rotor and the the center mass of the quadrotor aircraft. The coefficients κ and b are dependent on the density of air, size and shape of blades, as well as other factors(see [53] and [27] for more details). These two parameters will be identified in Section 3.2.

The main objective of this thesis is to control the orientation of the quadrotor in the flight. Hence, the translational dynamics are not considered in this thesis. Note that the gyroscopic torque is a passive term in the sense that it does not contribute to the variation of the rotational kinetic energy of the quadrotor and can be handled as zero *i.e.,* $G_a \approx 0$, in

near hover-conditions (*i.e.,* small pitch and roll angles). Therefore, the attitude kinematics using the unit quaternion representation are given by:

$$\dot{Q} \;=\; \frac{1}{2}Q \odot Q_\omega = \frac{1}{2}\begin{bmatrix} -q^\top \\ \eta I_3 + S(q) \end{bmatrix}\omega \tag{2.22}$$

$$I_f\dot{\omega} \;=\; -\omega \times I_f\omega + \tau \tag{2.23}$$

which can also be written by the Euler angles representation [54] as

$$\dot{\phi} \;=\; \omega_1 + \omega_2 \sin\phi\tan\theta + \omega_3 \cos\phi\tan\theta$$

$$\dot{\theta} \;=\; \omega_2 \cos\phi - \omega_3 \sin\phi$$

$$\dot{\psi} \;=\; \omega_2 \sin\phi\sec\theta + \omega_3 \cos\phi\sec\theta$$

$$\dot{\omega}_1 \;=\; \frac{(I_\theta - I_\psi)}{I_\phi}\omega_2\omega_3 + \frac{1}{I_\phi}\tau_\phi$$

$$\dot{\omega}_2 \;=\; \frac{(I_\psi - I_\phi)}{I_\theta}\omega_1\omega_3 + \frac{1}{I_\theta}\tau_\theta$$

$$\dot{\omega}_3 \;=\; \frac{(I_\phi - I_\theta)}{I_\psi}\omega_1\omega_2 + \frac{1}{I_\psi}\tau_\psi \tag{2.24}$$

where, the inertia matrix $I_f = diag(I_\phi, I_\theta, I_\psi)$, angular velocity $\omega = [\omega_1, \omega_2, \omega_3]^\top$, and control torque $\tau = [\tau_\phi, \tau_\theta, \tau_\psi]^\top$.

Chapter 3

Experimental Platform

Recently, various open-source platforms dealing with quadrotor UAVs have been developed. A comparative study of these quadrotor UAV platforms is given in [55]. Our experimental platform is designed based on the Arducopter [56] provided by 3DR-robotics [57] as shown in Fig. 3.1. The setups of our quadrotor platform for the experiments are the airframe, the autopilot system, and other electronic parts. The control algorithms are programed using C/C++ with the open-source Arduino software.

3.1 General Overview of Airframe and Electronics
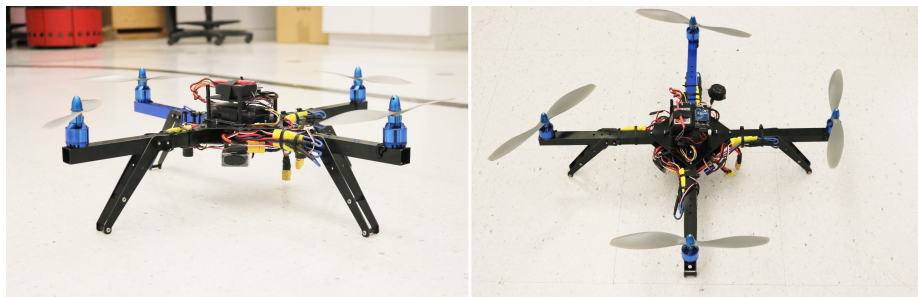
Figure 3.1: Experimental platform

As shown in Fig. 3.1, the quadrotor consists of a cross frame with 4 aluminum arms and 4 motors attached to the end of each arm, fibreglass mounting platforms and fibreglass landing legs. Its hardware include micro-processors, inertial sensors, electronic speed controllers (ESCs), actuators and other necessary parts. All the parts are widely available and easy to be replaced. Details about the individual components will be provided in the remainder of this section. An overview of the experimental hardware has been shown in Fig. 3.2, and a diagram of the quadrotor hardware is presented in Fig. 3.3.
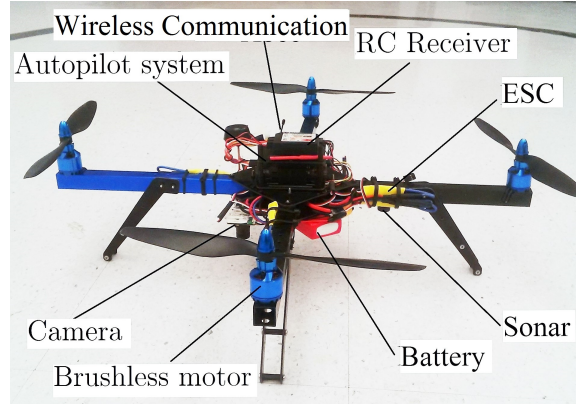
Figure 3.2: Overview of the quadrotor hardwares
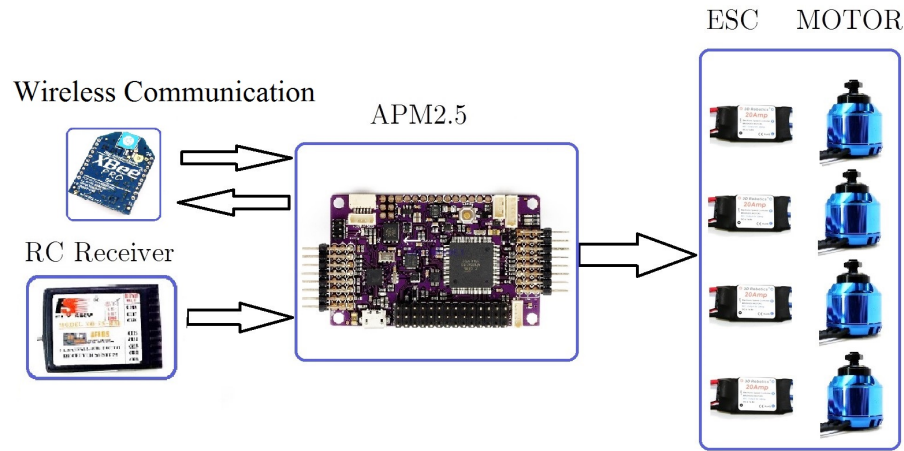
Figure 3.3: Diagram of the quadrotor hardwares

3.1.1   Autopilot System

The ArduPilotMega (APM) 2.5 is the main on-board controller equipped in our quadrotor UAV. The APM 2.5 is a low-cost system and is available as a ready-to-fly solution. As shown in Fig. 3.4, it contains two microprocessors (Atmel Atmega 2560 and Atmel Atmega 32U-2) and an Inertial Measurement Unit (IMU: a MPU6000 and a HMC5883L). The details are provided as follows:

- *Atmel Atmega 2560* [1]:

  A high-performance, low-power 8-bit AVR RISC based microprocessor with 256kB flash memory, 8KB SRAM and 4KB EEPROM. It has 86 general purpose I/O lines, 4 USARTs and serial peripheral interface (SPI) and I^{2}C interface to communicate with the sensors and peripherals. Also, it contains real-time counters, six flexible timer/counters with compare modes and hardware and software generated PWM sig-

---

[1]http://www.atmel.com/devices/atmega2560.aspx
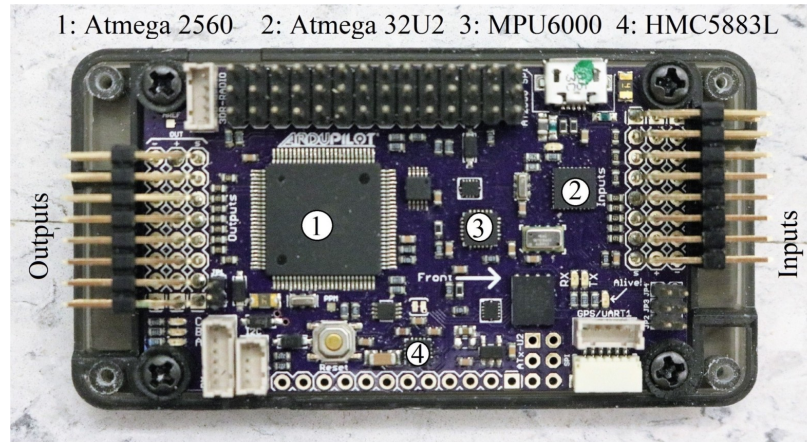
Figure 3.4: Autopilot system APM 2.5

nals for generating motor output and demodulating input radio signals. This device operates at 16MHz between 4.5-5.5 volts input source which is sufficient for the implementation of hardware setup and control algorithms as well as communication functions. For more details, please refer to [58].

- *Atmel Atmega 32U2* [2]:

  Atmega32U2 is a secondary microcontroller on-board of the APM2.5, which is a high performance, low power 8-bit microcontroller with 32K bytes of ISP flash and USB controller. Its primary function consists of offloading the radio inputs and motor outputs generated by Atmega2560. Up to eight radio input channels can be fed to the general pupose pins of Atmega32U2 and are converted to PPM (Pulse Position Modulation) signals to be decoded by Atmega2560. It also acts as the in-line programmer for the Atmega2560. The Atmega32U2 is connected to USB header and serves as a programmer via the UART0 pin of the Atmega2560. It is the main source of communication between the base-station computer and the APM2.5. Further details are provided in [59].

- *Invensense MPU6000:*

  MPU-6000 from Invense Inc. combines a 3-axis accelerometer and a 3-axis gyroscope on the chip with an onboard digital motion processor capable of processing complex 9-axis MotionFusion algorithms. It is connected to the Atmega2560 through the SPI lines and is fully programmable. It is a highly versatile device offering a large variety of gyroscope full-scale range of ± 250, ± 500, ± 1000, and ± 2000 degrees/sec (dps) and a user-programmable accelerometer full-scale range of $\pm 2g$, $\pm 4g$, $\pm 8g$, and $\pm 16g$.

  The output of the accelerometer is sampled by 16-bit ADC on each axis and conditioned by a low pass filter with variable configuration. Another set integrated 16-bit ADCs sample each gyroscope axis from 8000 to 1000 samples per second and a configurable low-pass filter can be set to a wide range of cut-off frequencies (see Table 3.1 for details). Both the gyroscope and accelerometer reading are stored in data registers

---

and can be recovered by Atmega 2560 via SPI protocol. More details can be found in [60].

Accelerometer (Fs = 1kHz)		Gyroscope		
Bandwidth(Hz)	Delay (ms)	Bandwidth (Hz)	Delay (ms)	Fs(khz)
260	0	256	0.98	8
184	2.0	188	1.9	1
94	3.0	98	2.8	1
44	4.9	42	4.8	1
21	8.5	20	8.3	1
10	13.8	10	13.4	1
5	19.0	5	18.6	1

Table 3.1: Low pass filter specifications for the accelerometer and gyroscope

- *Honeywell HMC5883L*

  The Honeywell HMC588L magnetometer is a 3-axis digital compass measuring its surrounding magnetic field. Since there is no on-board regulator, a regulated voltage of 2.16-3.6V should be supplied. The magnetometer has a full scale reading of ± 8 gauss that is scalable through a 3-bit gain control ranging the output from ± 1 gauss to ± 8 gauss. The output of the magnetometer is sampled on-chip by 12-bit ADC which enables 1° to 2° compass heading accuracy. The reading is stored in a data register and accessed by the I^2C digital interface. The output rates can be varied from 0.75Hz to 75Hz with the default being 15Hz. Since the quadrotor platform is designed for agile performance, the magnetometer is configured to run at the maximum output rate of 75Hz. See [61] for more details.

3.1.2 Communication

The RC radio transmitter (FS-TH9X [3]) and the RC radio receiver (FS-R8B) set used for radio communication in our quadrotor platform is a 2.4 GHz system with 8 channels as shown in Fig. 3.5. However, only 5 channels have been used in our quadrotor system for sending the commands (PPM signals) of the roll, pitch, yaw, throttle, and mode-switch.

The throttle stick does not return to the middle position when the finger is removed, while the roll and pitch control sticks do return to the center. The PPM signals from the transmitter vary while changing the angles of control sticks having a value between 900-2200. The maximum and minimum throttle values vary slightly and must be recorded in order to properly generate desired thrust. The PPM values of the pitch and yaw at the center are designed as zero angles, since the pitch and roll sticks can return to the center automatically. In order to properly generate the desired roll and pitch angles, the PPM values at the center must be recorded. For the yaw command, it is a little different from the roll/pitch. The position of the yaw stick provides the rotation rate of the yaw and zero rotation rate at the center.

---

[3]http://www.flysky-cn.com/products_detail/&productId=42.html

Figure 3.5: Transmitter FS-TH9X (left) and receiver FS-R8B (right)

The wireless serial connectivity is provided to make a communication between the ground base-station computer and the quadrotor UAV. The wireless serial communication system operates at 2.4GHz using an Xbee Series 1 module connected to the quadrotor and an XStick USB module connected to the computer (see Fig. 3.6). Experimental data, for example the sensor measurements, are sent to the ground station for analysis. The baud rate of the serial communication has been set as 57600bps in our quadrotor system.

Figure 3.6: Xbee serial 1 module (left) and XStick USB module (right)

3.1.3 Power Module and Actuators

The entire platform is powered by a 3300mAh 3-cell lithium polymer battery. The battery voltage when fully charged is 12.4V, and 9.9 V when discharged.

The brushless motor and electronic speed controller (ESC) pairs, as shown in Fig. 3.7, serve as actuators for the quadrotor. The ESCs are driven by the PWM signals of the desired motor speeds sent from the APM 2.5. The ESC convert the DC voltage provided by the battery to a 3-phase AC current to drive the motor working at the designed speed. Since, the speed of the motor is controlled by the ESC, a feedback from the motor is embedded. Earlier speed controller employed Hall effect sensors but more recent ones measure the back-EMF generated in the un-driven coils. The motor A2830 used in our quadrotor is an out-runner brushless motor. Its specifications provided by the manufacturer are given in

Figure 3.7: 20Amp ESC (left) and brushless motor (right)

Table 3.2.

Model	Volts	KV (rpm/V)	Max Pull	Weight	Max power	ESC
A2830-12	7.5-15V	850	880g	52g	200watt	20A

Table 3.2: Motor specification

One can obtain the max speed of motor A2830 powered by our battery (at 12 Voltage) as

$$\varpi_{max} = 12 \times 850 \times \frac{2\pi}{60} rad/s = 1.0681 \times 10^3 rad/s$$

3.2 Model Identification

3.2.1 Propeller Aerodynamics

Based on the aerodynamics model, the steady-state thrust generated by the propeller while hovering (*i.e.,* a rotor that is not translating horizontally or vertically) in free air can be modeled using momentum theory (see [62] and Section 2.2.6 in [63] for mere details) as

$$\mathcal{T} = C_T \rho n^2 D^4 = b\varpi^2 \tag{3.1}$$

where, C_T is the coefficient of thrust dependent on the propeller geometry and aerodynamics characteristics, ρ is the density of air, n is the speed revolutions per sec, D is the diameter of the propeller, ϖ is the angular velocity of the motor, and b denotes the thrust factor.

The propeller reactive torque is generated by the propeller motion as follows

$$Q = C_Q \rho n^2 D^5 = \kappa \varpi^2 \tag{3.2}$$

where $C_Q = C_P/2\pi$ and C_P are the power coefficients of the propeller dependent on the propeller geometry and aerodynamics characteristics, and κ denotes the torque coefficient.

The propellers used in our experiments are the APC $10\times$ 4.7 propellers with a 10-inch diameter and a pitch of 4.7-inch per revolution. The thrust and power coefficients are

Name	Parameter	Value	Units
Diameter	D	0.2540	m
Thrust coefficient	C_T	0.1223	$-$
Power coefficient	C_P	0.0494	$-$
Air density (15℃)	ρ	1.225	kg/m^3

Table 3.3: Propeller thrust parameters

determined by static thrust tests done in [64]. From (3.1) and (3.2), and the parameters provided in Table 3.3, one can obtain the thrust coefficient b and torque coefficient κ as

$$b = \frac{C_T \rho D^4}{4\pi^2} = 1.5796e^{-5} \tag{3.3}$$

$$\kappa = \frac{C_P \rho D^5}{8\pi^3} = 2.5792e^{-7} \tag{3.4}$$

3.2.2 Moment of Inertia

Motivated by the work done in [65], a similar pendulum experiment setup has been realized by hanging the aircraft from one end, and allowing it to swing around the axis of interest (see [65] for more details). The kinetic energy is given by

$$K = \frac{1}{2}I_i\dot{\vartheta}^2 + \frac{1}{2}m(\dot{\vartheta}l)^2 \tag{3.5}$$

where, ϑ is the oscillation angle, I_i is the moment of inertia, l is the distance from the center of gravity of the quadrotor to the hanging point, and m is the mass of the quadrotor. The potential energy is given by

$$V = mg(l - l\cos\vartheta) \tag{3.6}$$

Then, we obtain the Lagrangian as follows:

$$L = K - V = \frac{1}{2}I_i\dot{\vartheta}^2 + \frac{1}{2}m(\vartheta l)^2 - mg(l - l\cos\vartheta) \tag{3.7}$$

Applying Euler-Lagrange equation,

$$\frac{d}{dt}\left(\frac{\partial L}{\partial \dot{\vartheta}}\right) - \frac{\partial L}{\partial \vartheta} = 0 \tag{3.8}$$

one obtains the following second-order dynamics

$$(I_i + ml^2)\ddot{\vartheta} + mgl\sin\vartheta = 0 \tag{3.9}$$

Since the oscillation occurs in small angles, let us assume that ϑ is small enough, *i.e.*, $\sin\vartheta \approx \vartheta$, then we can rewrite (3.9) as

$$(I_i + ml^2)\ddot{\vartheta} + mgl\vartheta = 0 \tag{3.10}$$

The natural frequency of the second-order dynamics (3.9) is given by

$$\omega_{n,i} = \sqrt{\frac{mgl}{I_i + ml^2}} \tag{3.11}$$

On the other hand, the natural frequency can also be obtained from the experimental test. With the natural frequency obtained from the test, one obtains the moment of inertia as follows:

$$I_i = \frac{mgl}{\omega_{n,i}^2} - ml^2 \tag{3.12}$$

Three tests are reported, and the oscillation responses around the roll, pitch and yaw axes have been shown in Fig. 3.8-3.10 respectively.
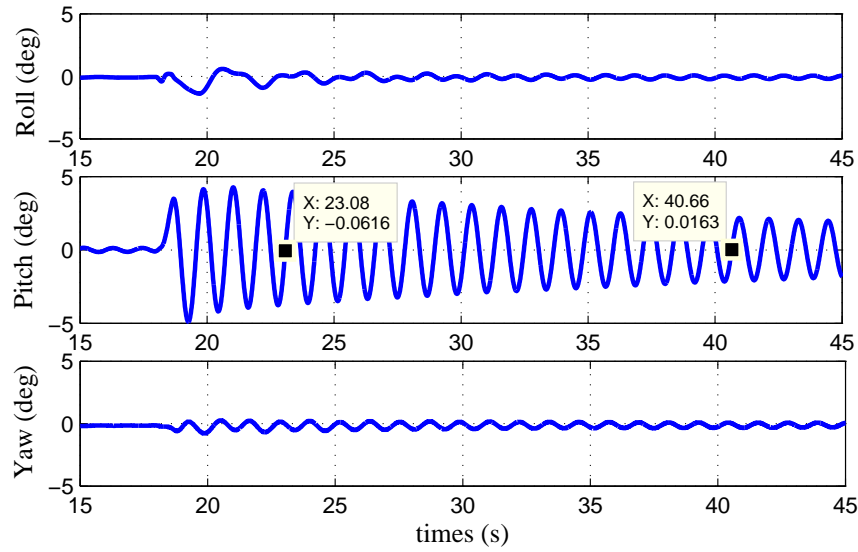
Figure 3.8: Test 1: oscillation around x axis

Instead of manually calculating the natural frequencies, the Fast Fourier Transform (FFT) is applied using MATLAB to find the natural frequencies of the oscillations around the roll, pitch and yaw axes, respectively. As shown in Fig. 3.11, the natural frequencies can be obtained as follows:

$$\omega_{n,\phi} = 5.3426 \; rad/s \quad \omega_{n,\theta} = 5.3627 \; rad/s \quad \omega_{n,\psi} = 5.0762 \; rad/s. \tag{3.13}$$

Substituting these natural frequencies in (3.12) with the mass provided in Table 3.4, we have the following moment of inertia around the roll, pitch and yaw axes respectively as

$$I_\phi = 0.0159 \; kg \cdot m^2 \quad I_\theta = 0.0150 \; kg \cdot m^2 \quad I_\psi = 0.0297 \; kg \cdot m^2 \tag{3.14}$$

3.2.3   Other Parameters

To generate the exact thrust for hovering where the total thrust is equal to the gravity, the knowledge about the weight of the quadrotor aircraft is required. Unlike the gas powered aircraft and spacecraft, the mass of our electric powered quadrotor does not change
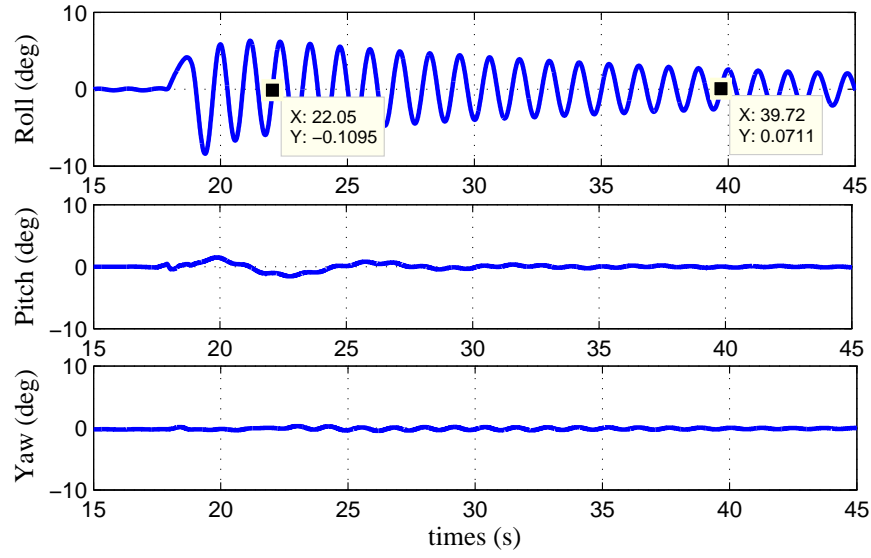
Figure 3.9: Test 2: oscillation around y axis
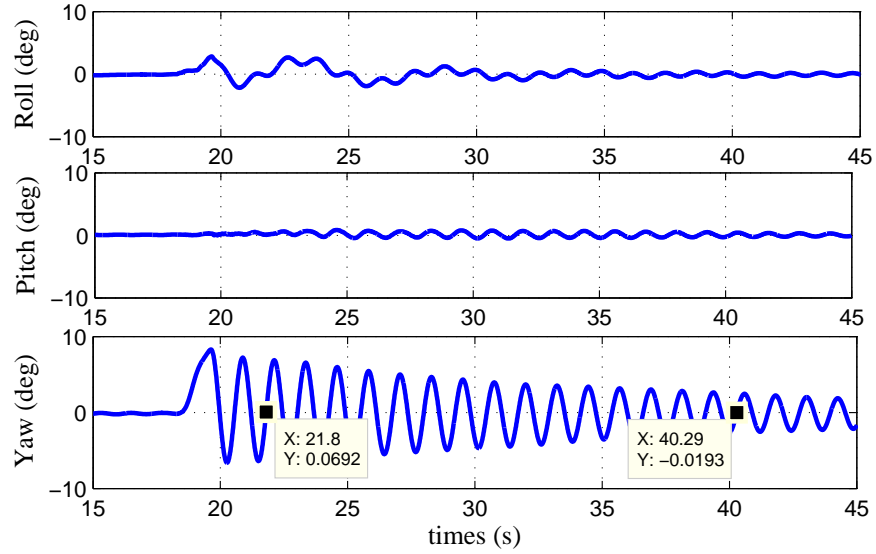
Figure 3.10: Test 3: oscillation around z axis

throughout the flight. The mass of our quadrotor is 1.234 kg measured by a digital hanging scale.

From (2.18) - (2.21), the distances from the center mass of the quadrotor to the center of each motor are required to find the actual torque applied to the quadrotor. Assuming careful design, the center of gravity can be considered as the intersection point of the four arms. So we measured the distance between a pair of motors and divided it by two. The distance d is given by 0.259 m.
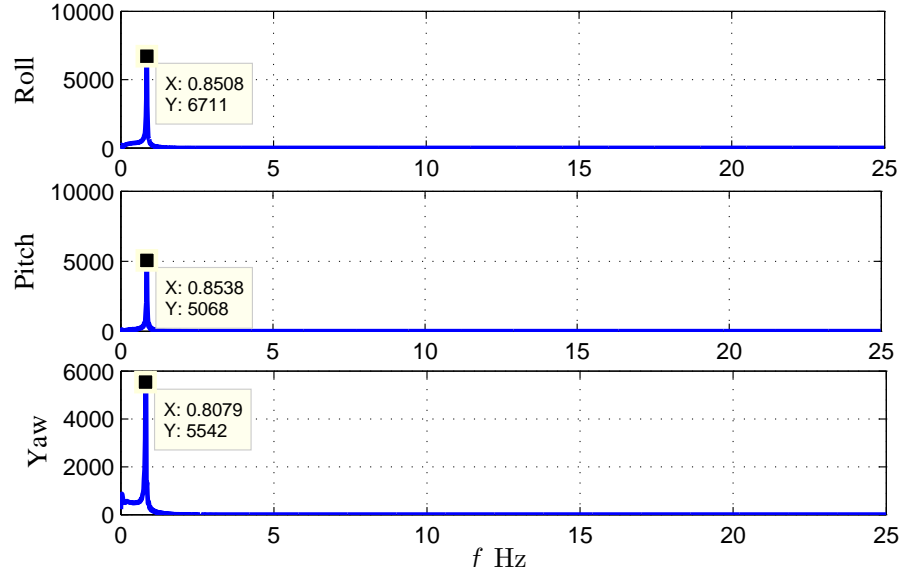
Figure 3.11: Oscillation results with FFT

Finally, the model parameters involved in our quadrotor model are given in Table 3.4.

Parameter	Description	Value	Units
I_ϕ	Roll Inertia	0.0159	$kg \cdot m^2$
I_θ	Pitch Inertia	0.0150	$kg \cdot m^2$
I_ψ	Yaw Inertia	0.0297	$kg \cdot m^2$
b	Thrust coefficient	1.5796e-05	$N \cdot s^2/rad^2$
κ	Torque coefficient	2.5792e-07	$N \cdot m \cdot s^s/rad^2$
d	Distance	0.259	m
m	Mass	1.234	kg
g	Gravity Constant	9.81	m/s^2

Table 3.4: Quadrotor system parameters

3.3 Calibration Techniques

3.3.1 Sensors Calibration

The sensors used in our quadrotor, for example, the gyroscope, the accelerometer, and the magnetometer, are prone to have biases in the measurements. Since the changes of these biases during one flight are negligible, this allows us to estimate them once at the beginning of a mission and then keep them constants. For the sensors calibration, we assume that the noise in the measurements have zero mean. The details of the sensors calibration are as follows:

- *Gyroscope Calibration:* The gyroscopes measure the angular velocity of the quadrotor relative to the inertial frame expressed in the body-fixed frame $\mathcal{B}$.

$$\omega_{\mathcal{B}} = \omega + b_g + n_g \tag{3.15}$$

where b_g is a constant (or slowly time-varying) gyro bias, n_g denotes the additive measurement noise, and ω is the actual angular velocity expressed in the body-fixed frame. We can average the gyroscope measurements over N samples at the beginning (before take-off *i.e.,* $\omega = 0$) to estimate the gyroscope measurement bias b_g, which is given by

$$\hat{b}_g = \frac{1}{N} \sum_{k=1}^{N} \omega_{\mathcal{B}}(k)$$

- *Accelerometer Calibration:* The accelerometers measure the instantaneous linear acceleration of the quadrotor expressed in body-fixed frame $\mathcal{B}$.

$$a_{\mathcal{B}} = R^{\top}(a - ge_3) + b_a + n_a \tag{3.16}$$

where, R is the rotation matrix, b_a is a bias term, n_a denotes the additive measurement noise, and a is the derivative of the linear velocity expressed in the inertial frame. Similarly, the accelerometer measurements can also be averaged over N samples before take-off *i.e.,* $R = I_3$ given by

$$\hat{b}_a = \frac{1}{N} \sum_{k=1}^{N} a_{\mathcal{B}}(k) + g$$

When performing the sensor biases calibration, we sampled the IMU reading over a $6s$ period, which is enough to provide accurate estimates of the biases. The accelerometers and gyroscopes are highly susceptible to vibration, therefore, they are mounted on a foam tape or gel to reduce the noise in the sensor measurements. Moreover, a Digital Low Pass Filter (DLPF) has also been implemented to further clean the sensor signals.

- *Magnetometer Calibration:* The magnetometers provide measurements of the ambient magnetic field, which is defined by

$$m_{\mathcal{B}} = DR^{\top}m_{\mathcal{I}} + b_m + n_m \tag{3.17}$$

where, D is the distortion, $m_{\mathcal{I}}$ denotes the Earth's magnetic field vector (expressed in the inertial frame), b_m is a body-fixed frame expression for the local magnetic disturbance, and n_m denotes the measurement noise. The noise n_m is usually low for magnetometer reading; however, the local magnetic disturbance b_m can be significant, especially if the sensor is placed near the power wires and/or the motors.

The compensation approach proposed in [66] and [67] has been implemented in our quadrotor system. Define

$$D = \begin{bmatrix} \epsilon_x & 0 & 0 \\ \epsilon_y \sin \delta_x & \epsilon_y \cos \delta_x & 0 \\ \epsilon_z \sin \delta_y \cos \delta_z & \epsilon_z \sin \delta_z & \epsilon_z \cos \delta_y \cos \delta_z \end{bmatrix} \qquad b_m = \begin{bmatrix} \varrho_x \\ \varrho_y \\ \varrho_z \end{bmatrix}$$

with $(\epsilon_x, \epsilon_y, \epsilon_z)$ are the total scale errors, $(\delta_x, \delta_y, \delta_z)$ are the sensor misalignment angles, and $(\varrho_x, \varrho_y, \varrho_z)$ are the sensor offsets. In the absence of noise, one can solve the (3.17) for $R^\top m_{\mathcal{I}}$ as

$$R^\top m_{\mathcal{I}} = D^{-1}(m_{\mathcal{B}} - b_m) \tag{3.18}$$

Using the fact that $m_{\mathcal{B}} = [m_{\mathcal{B}_x}, m_{\mathcal{B}_y}, m_{\mathcal{B}_z}]^\top$, and taking the norm of (3.18) on both sides, one has

$$C_1 m_{\mathcal{B}_x}^2 + C_2 m_{\mathcal{B}_x} m_{\mathcal{B}_y} + C_3 m_{\mathcal{B}_x} m_{\mathcal{B}_z} + C_4 m_{\mathcal{B}_y}^2 + C_5 m_{\mathcal{B}_y} m_{\mathcal{B}_z}$$
$$+ C_6 m_{\mathcal{B}_z}^2 + C_7 m_{\mathcal{B}_x} + C_8 m_{\mathcal{B}_y} + C_9 m_{\mathcal{B}_z} = C_{10} \tag{3.19}$$

where, the coefficients C_k, $1 \leq k \leq 10$ are the functions of the 10 parameters $\epsilon_i, \delta_i, \varrho_i, i \in \{x, y, z\}$ and $\|m_{\mathcal{I}}\|$. The value of $\|m_{\mathcal{I}}\|$ can be found from the local magnetic field, and the best estimates of C_k in a least-square sense can be found by restructuring (3.19), putting it in matrix form with N samples

$$\mathbb{X}\mathbb{C} = \mathbb{W} \tag{3.20}$$

where

$$\mathbb{X} = \underbrace{\begin{bmatrix} m_{\mathcal{B}_{x1}}^2 & m_{\mathcal{B}_{x1}} m_{\mathcal{B}_{y1}} & \cdots & m_{\mathcal{B}_{z1}} \\ m_{\mathcal{B}_{x2}}^2 & m_{\mathcal{B}_{x2}} m_{\mathcal{B}_{y2}} & \cdots & m_{\mathcal{B}_{z2}} \\ \vdots & \vdots & \ddots & \vdots \\ m_{\mathcal{B}_{xN}}^2 & m_{\mathcal{B}_{xN}} m_{\mathcal{B}_{yN}} & \cdots & m_{\mathcal{B}_{zN}} \end{bmatrix}}_{N \times 9} \quad \mathbb{C} = \underbrace{\begin{bmatrix} C_1/C_{10} \\ C_2/C_{10} \\ \vdots \\ C_9/C_{10} \end{bmatrix}}_{9 \times 1} \quad \mathbb{W} = \underbrace{\begin{bmatrix} 1 \\ 1 \\ \vdots \\ 1 \end{bmatrix}}_{N \times 1}$$

where, the magnetometer data set $\{m_{\mathcal{B}}\}$ consisting of N data points (at least 1000 samples) are collected by rotating the quadrotor along all the axes, and recorded them using the serial communication. Finally, $\mathbb{C}_{est}$, a least-squares best fit estimate for $\mathbb{C}$, can be generated as

$$\mathbb{C}_{est} = (\mathbb{X}^\top \mathbb{X})^{-1} \mathbb{X}^\top \mathbb{W} \tag{3.21}$$

Now the estimates of $\mathbb{C}$ have been found, solutions for $\epsilon_i, \delta_i, \varrho_i, i \in \{x, y, z\}$ can be obtained by solving nine nonlinear equations with nine unknowns. In this case, MAT-LAB is used to solve for the parameters from the measured data. See Appendix C for more details.

The nine parameters involved in our test are solved and given by

$$\epsilon = \begin{bmatrix} 0.8027 \\ 0.8218 \\ 0.7213 \end{bmatrix} \qquad \delta = \begin{bmatrix} 0.0001 \\ 0.0205 \\ 0.0068 \end{bmatrix} \qquad \varrho = \begin{bmatrix} 0.0528 \\ 0.0181 \\ -0.0007 \end{bmatrix} \tag{3.22}$$

Fig. 3.12 shows the calibration results. The calibrated 3-axis magnetometer measurements trace out a sphere centered at the origin, since the magnitude of the magnetic vector is constant. The uncalibrated magnetometer measurements appear elliptical instead of spherical. With the estimated distortion D and local magnetic disturbance b_m, the future magnetometer measurements can be corrected as follows:

$$\hat{m}_{\mathcal{B}} = D^{-1}(m_{\mathcal{B}} - b_m) \tag{3.23}$$

Note that the magnetometer measurements need to be calibrated again once the environment is changed.
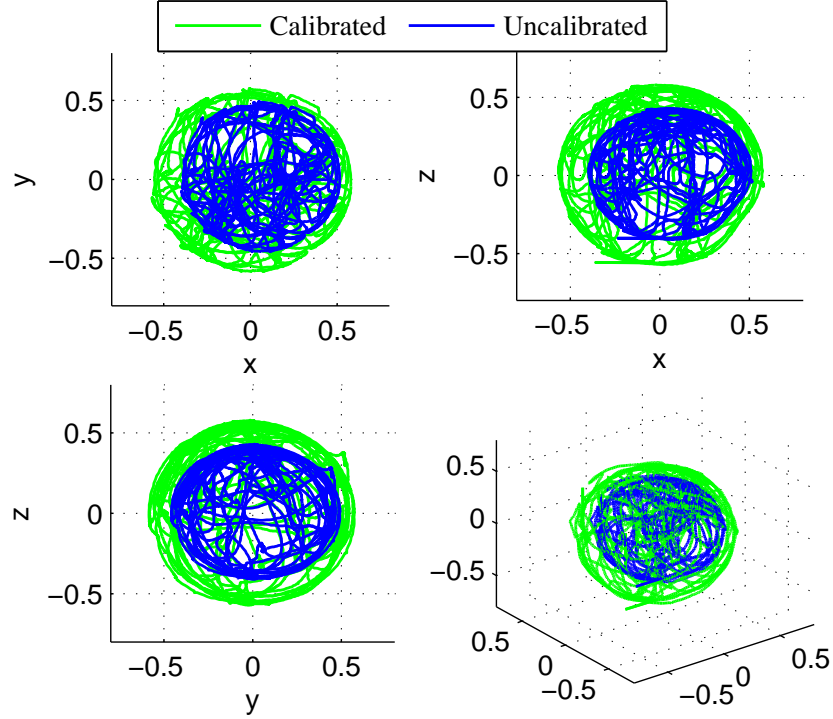
Figure 3.12: Magnetometer calibration results

3.3.2 Propeller Efficiency Calibration

As mentioned in (3.1), the thrust f of a single rotor can be modeled as

$$f = C_T \rho n^2 D^4 = b\varpi^2 \tag{3.24}$$

The rotor angular velocity ϖ is controlled by the ESC. However, the density of the air ρ is not constant as it depends on the air pressure and temperature. Additionally, wear and possible damages to the propellers and rotors might cause unexpected changes in C_T. These effects might change the equilibrium point of the quadrotor system and cause an observable translational motion during hover. Let us define the real propeller efficiency mapping coefficient c_i, $i \in \{1, 2, 3, 4\}$, then the actual thrust and drag moment generated by the propeller i are given by

$$\mathcal{T}_i^a = c_i b\varpi_i^2 \qquad Q_i^a = c_i \kappa \varpi_i^2$$

In the case of hovering, the angular velocity and the acceleration of the quadrotor should be equal to zero and the gravity, respectively. Thus, from (2.22) and (2.23), one obtains the following equation

$$\begin{bmatrix} 0 & db & 0 & -db \\ db & 0 & -db & 0 \\ -k & k & -k & k \\ b & b & b & b \end{bmatrix} \begin{bmatrix} c_1\varpi_1^2 \\ c_2\varpi_2^2 \\ c_3\varpi_3^2 \\ c_4\varpi_4^2 \end{bmatrix} = \begin{bmatrix} 0 \\ 0 \\ 0 \\ mg \end{bmatrix} \tag{3.25}$$

The equation (3.25) can be rearranged as

$$
\begin{bmatrix} c_1\varpi_1^2 \\ c_2\varpi_2^2 \\ c_3\varpi_3^2 \\ c_4\varpi_4^2 \end{bmatrix} = \begin{bmatrix} 0 & \frac{1}{2db} & -\frac{1}{4k} & \frac{1}{4b} \\ \frac{1}{2db} & 0 & \frac{1}{4k} & \frac{1}{4b} \\ 0 & -\frac{1}{2db} & -\frac{1}{4k} & \frac{1}{4b} \\ -\frac{1}{2db} & 0 & \frac{1}{4k} & \frac{1}{4b} \end{bmatrix} \begin{bmatrix} 0 \\ 0 \\ 0 \\ mg \end{bmatrix}
\tag{3.26}
$$

Then, we can solve for c_i as

$$
c_i = \frac{mg}{4b\varpi_i^2}, \quad i = 1,2,3,4
\tag{3.27}
$$

where, the motor speeds are obtained by averaging the applied motor speeds over N samples,

$$
\varpi_i = \frac{1}{N} \sum_{k=1}^{N} \varpi_{i,k}
$$

To perform the propeller efficiency calibration, we sample the applied motor speeds over a $5s$ period, which is sufficient to get a good motor speed estimation. Then, the actual torque and thrust applied to the quadrotor can be generated as

$$
\begin{bmatrix} \tau_\phi^a \\ \tau_\theta^a \\ \tau_\psi^a \\ \mathcal{T}^a \end{bmatrix} = \begin{bmatrix} 0 & db & 0 & -db \\ db & 0 & -db & 0 \\ -k & k & -k & k \\ b & b & b & b \end{bmatrix} \begin{bmatrix} c_1 & 0 & 0 & 0 \\ 0 & c_2 & 0 & 0 \\ 0 & 0 & c_3 & 0 \\ 0 & 0 & 0 & c_4 \end{bmatrix} \begin{bmatrix} \varpi_1^2 \\ \varpi_2^2 \\ \varpi_3^2 \\ \varpi_4^2 \end{bmatrix}
\tag{3.28}
$$

With the propeller efficiency coefficients, one can modify the desired motor speeds from the designed torque and thrust as

$$
\begin{bmatrix} \varpi_{1,d}^2 \\ \varpi_{2,d}^2 \\ \varpi_{3,d}^2 \\ \varpi_{4,d}^2 \end{bmatrix} = \begin{bmatrix} \frac{1}{c_1} & 0 & 0 & 0 \\ 0 & \frac{1}{c_2} & 0 & 0 \\ 0 & 0 & \frac{1}{c_3} & 0 \\ 0 & 0 & 0 & \frac{1}{c_4} \end{bmatrix} \begin{bmatrix} 0 & \frac{1}{2db} & -\frac{1}{4k} & \frac{1}{4b} \\ \frac{1}{2db} & 0 & \frac{1}{4k} & \frac{1}{4b} \\ 0 & -\frac{1}{2db} & -\frac{1}{4k} & \frac{1}{4b} \\ -\frac{1}{2db} & 0 & \frac{1}{4k} & \frac{1}{4b} \end{bmatrix} \begin{bmatrix} \tau_\phi \\ \tau_\theta \\ \tau_\psi \\ \mathcal{T} \end{bmatrix}
\tag{3.29}
$$

Assmue that $\varpi_i = \varpi_i^d$, $i = 1,2,3,4$, one can conclude that the actual torque and thrust are equal to the designed control torque and thrust. Note that the propeller efficiency coefficients may change after flying several times , the coefficients are given as follows during our test

$$
\frac{1}{c_1} = 1.10 \quad \frac{1}{c_2} = 1.02 \quad \frac{1}{c_3} = 1.00 \quad \frac{1}{c_4} = 1.13
\tag{3.30}
$$

3.3.3 RC Channels and ESCs Calibration

The RC transmitter/receiver, shown in Fig. 3.5, requires some simple calibration to ensure proper operation. The calibration of RC channels is a straightforward process simply move each of the enabled sticks through their full range and record the maximum, minimum and trim values for each RC channel. By moving the control sticks to their limits of travel, one has the channels parameters presented in Table 3.5. The desired thrust of quadrotor at the

Channel	Minimum	Trim	Maximum	Function
0	1074	1501	1926	Roll
1	1084	1503	1936	Pitch
2	992	992	1714	Throttle
3	1070	1504	1922	Yaw

Table 3.5: RC channels parameters

period k can be generated as

$$\mathcal{T}_d(k) \;=\; 4b\left(\frac{P_{\mathcal{T},r}(k) - P_{\mathcal{T},min}}{P_{\mathcal{T},max} - P_{\mathcal{T},min}}\varpi_{\max}\right)^2 \tag{3.31}$$

where, b is the thrust coefficient defined in Section 3.2.1, $P_{\mathcal{T},min}$ and $P_{\mathcal{T},max}$ are the minimum and maximum throttle values respectively, $P_{\mathcal{T},r}$ is the throttle PPM value received from the transmitter, and $\varpi_{\max}$ is the maximum angular velocity of the motor defined in Section 3.1.3.

The desired roll, pitch and yaw angles at the period k are given by

$$\phi_d(k) \;=\; \frac{P_{\phi,r}(k) - P_{\phi,trim}}{S_f} \tag{3.32}$$

$$\theta_d(k) \;=\; \frac{P_{\theta,r}(k) - P_{\theta,trim}}{S_f} \tag{3.33}$$

$$\psi_d(k) \;=\; \psi_d(k-1) + \frac{P_{\psi,r}(k) - P_{\psi,trim}}{S_y} \tag{3.34}$$

where, $P_{\phi,r}$, $P_{\theta,r}$ and $P_{\psi,r}$ denote the PPM values of the roll, pitch and yaw commands respectively, $P_{\phi,trim}$, $P_{\theta,trim}$ and $P_{\psi,trim}$ are the recorded trim PPM values of the roll, pitch and yaw respectively. The parameter S_f denotes the stick factor for the roll and pitch converting the PPM values to Euler angles. The choice of this stick factor is $1/20$ providing a maximum desired angle about 25 degree for the roll and pitch. The parameter S_y determines the sensitivity of the rotation rate of the yaw, which is set as 1000.

Electronic speed controllers are responsible for spinning the motors at the speed requested by the autopilot. ESCs calibration is also important, since the ESCs need to know the minimum and maximum PWM values that the flight controller will send. A complete process of ESC calibration using the ground station and APM can be found in [68]. After successfully calibrating, the mapping from the motor speed to the PWM value of motor i is given by

$$P_i = P_{\mathcal{T},min} + \frac{\varpi_i}{\varpi_{max}} * (P_{\mathcal{T},max} - P_{\mathcal{T},min}) \tag{3.35}$$

where, ϖ_i denotes the speed of motor i and ϖ_{max} denotes the maximum motor speed, and $P_{\mathcal{T},max}$ and $P_{\mathcal{T},min}$ are the maximum and minimum throttle PWM values.

3.4 Overview of the Quadrotor Implementation

An overview of the cascaded controllers used for our quadrotor system is shown in Fig. 3.13. The lower level, the higher bandwidth, is the control of the four rotor angular velocities. Another level is the on-board attitude control of the quadrotor at the frequency of 100Hz. The processes of the on-board controller can be separated into three steps (from left to right):
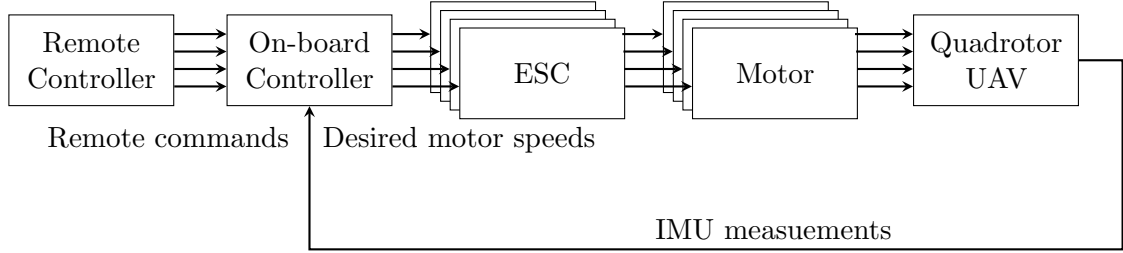
Figure 3.13: Overview of the quadrotor cascaded control loop

- Firstly, the on-board controller generates the desired attitude (ϕ_d, θ_d and ψ_d) and thrust ($\mathcal{T}_d$) from the PPM signals provided by the remote controller. The desired attitude and thrust are generated by (3.31) - (3.34) (see Section 3.3.3 for more details).

- The on-board controller reads the IMU measurements and calibrates the measurements (see Section 3.3.1). Then, the attitude control torque τ can be designed from the IMU measurements and/or the desired attitude generated in step 1. The details on attitude controller designing will be provided in Chapter 4 - 6.

- Finally, the desired motor speeds $\varpi_{i,d}$, $i = 1, 2, 3, 4$ can be generated by the control torque and thrust with the calibrated propeller efficiencies as shown in (3.29) (see Section 3.3.2 for more details). The PWM signals can be generated by (3.35) in Section 3.3.3 and sent to the actuators (ESCs and motors).

Chapter 4

Attitude Estimation and Control

In the absence of direct attitude measurement, the development of a robust and reliable attitude estimator is a key for a successful implementation of an efficient attitude control scheme. Theoretically, it is possible to estimate the attitude by integrating the rigid-body attitude kinematics using the angular velocity measurements, or reconstructing algebraically the orientation using the inertial measurements (at least two noncollinear inertial vectors measurements). However, in practice where the measurements are affected with noise, dynamic estimation algorithms relying on the angular velocity and inertial vector measurements are used. These estimation algorithms usually rely on the inertial measurement unit (IMU), typically including a gyroscope, an accelerometer and a magnetometer.

In this chapter, a nonlinear attitude estimator proposed in [23] will be implemented to estimate the attitude of the quadrotor. With the estimated attitude, the PD-like controller proposed in [39] has been fully tested in our quadrotor system. Both simulation results and experimental results are presented to show the effectiveness of our control scheme.

4.1   Attitude Estimation

4.1.1   Observer Design

Let us make the approximation that $a_\mathcal{B} \approx -gR^\top e_3$ for the case of hovering, and define the following vectors [23]:

$$
\begin{aligned}
u_\mathcal{I} &:= e_3, & v_\mathcal{I} &:= \frac{\pi_{u_\mathcal{I}} m_\mathcal{I}}{\|\pi_{u_\mathcal{I}} m_\mathcal{I}\|} \\
u_\mathcal{B} &:= -\frac{a_\mathcal{B}}{g}, & v_\mathcal{B} &:= \frac{\pi_{u_\mathcal{B}} m_\mathcal{B}}{\|\pi_{u_\mathcal{B}} m_\mathcal{B}\|}
\end{aligned}
\tag{4.1}
$$

where $\|x\|$ is the norm of vector x, and $\pi_x := \|x\|^2 I_3 - xx^\top, \forall x \in \mathbb{R}^3$ denotes the orthogonal projection on the plane orthogonal to x. It is obvious that $u_\mathcal{B} = R^\top u_\mathcal{I}$, and using the facts

$$
\begin{aligned}
R^\top \pi_{u_\mathcal{I}} m_\mathcal{I} &= R^\top (\|u_\mathcal{I}\|^2 I_3 - u_\mathcal{I} u_\mathcal{I}^\top) m_\mathcal{I} \\
&= (R^\top - R^\top u_\mathcal{I} u_\mathcal{I}^\top) RR^\top m_\mathcal{I} \\
&= (I_3 - u_\mathcal{B} u_\mathcal{B}^\top) m_\mathcal{B} \\
&= \pi_{u_\mathcal{B}} m_\mathcal{B}
\end{aligned}
$$

and

$$
\|\pi_{u_\mathcal{B}} m_\mathcal{B}\|^2 = (\pi_{u_\mathcal{B}} m_\mathcal{B})^\top (\pi_{u_\mathcal{B}} m_\mathcal{B}) = (\pi_{u_\mathcal{I}} m_\mathcal{I})^\top RR^\top (\pi_{u_\mathcal{I}} m_\mathcal{I}) = \|\pi_{u_\mathcal{I}} m_\mathcal{I}\|^2
$$

one has $v_\mathcal{B} = R^\top v_\mathcal{I}$. Define the estimates of the vectors $u_\mathcal{B}$ and $v_\mathcal{B}$ as

$$
\hat{u}_\mathcal{B} := \hat{R}^\top u_\mathcal{I}, \quad \hat{v}_\mathcal{B} := \hat{R}^\top v_\mathcal{I} \tag{4.2}
$$

where, $\hat{R}$ is the estimate of the actual attitude R, and the update law are given by [23]:

$$
\dot{\hat{R}} = \hat{R} S(\omega_\mathcal{B} - \hat{b} + \sigma_R) \tag{4.3}
$$

$$
\dot{\hat{b}} = -k_b \hat{b} + k_b \text{sat}_\Delta(\hat{b}) + \sigma_b \tag{4.4}
$$

$$
\sigma_R := k_1 u_\mathcal{B} \times \hat{u}_\mathcal{B} + k_2 \hat{u}_\mathcal{B} \hat{u}_\mathcal{B}^\top (v_\mathcal{B} \times \hat{v}_\mathcal{B}) \tag{4.5}
$$

$$
\sigma_b := -k_3 u_\mathcal{B} \times \hat{u}_\mathcal{B} - k_4 v_\mathcal{B} \times \hat{v}_\mathcal{B} \tag{4.6}
$$

where $\hat{b}$ is the estimate of the unknown bias b_g with $\|\hat{b}(0)\| < \Delta$ and Δ denoting positive constant, k_1, k_2, k_3, k_4 and k_b denote positive constants with $k_3 > k_4$, and the saturation function is defined by $\text{sat}_\Delta(x) := x \min(1, \Delta/\|x\|), \Delta > 0$. This estimator guarantees that, for almost all initial conditions, the trajectory of $(\hat{R}(t), \hat{b}(t))$ converges to the trajectory of $(R(t), b(t))$ asymptotically (see Theorem 1 in [23]).

4.1.2 Quaternion and Discrete Version

It is computationally expensive to compute the observer (4.3-4.6) mentioned above using rotation matrix representation, since the rotation matrix has nine variables. However, as discussed earlier, the unit-quaternion representation presents some advantages with respect to the rotation matrix representation in terms of computational efficiency. We can rewrite the observer given in (4.3 - 4.4) in terms of unit quaternion representation as follows:

$$
\dot{\hat{Q}} = \frac{1}{2} A(\hat{\omega}) \hat{Q} \tag{4.7}
$$

$$
\dot{\hat{b}} = -k_b \hat{b} + k_b \text{sat}_\Delta(\hat{b}) + \sigma_b \tag{4.8}
$$

where, $\hat{\omega} = [\hat{\omega}_1, \hat{\omega}_2, \hat{\omega}_3]^\top := \omega_\mathcal{B} - \hat{b} + \sigma_R$, $\hat{Q} = [\hat{\eta} \quad \hat{q}^\top]^\top$, and

$$
A(\hat{\omega}) := \begin{bmatrix} 0 & -\hat{\omega}^\top \\ \hat{\omega} & -\hat{\omega}_\times \end{bmatrix} = \begin{bmatrix} 0 & -\hat{\omega}_1 & -\hat{\omega}_2 & -\hat{\omega}_3 \\ \hat{\omega}_1 & 0 & \hat{\omega}_3 & -\hat{\omega}_2 \\ \hat{\omega}_2 & -\hat{\omega}_3 & 0 & \hat{\omega}_1 \\ \hat{\omega}_3 & \hat{\omega}_2 & -\hat{\omega}_1 & 0 \end{bmatrix}
$$

Assume that the sample time T is small enough, so that $\hat{\omega}(t)$ and $\sigma_b(t)$ remain constant over every period of time $(kT, (k+1)T], \forall k \in \mathbb{N}$. A discrete-time version of the observer (4.7) with a sampling period T is given by

$$\hat{Q}_{k+1} = \exp\left(\frac{T}{2}A(\hat{\omega}_k)\right)\hat{Q}_k \tag{4.9}$$

As shown in [23], the unit-quaternion based discrete-time attitude estimator using Taylor's expansions is given by (see Appendix A for more details)

$$\hat{Q}_{k+1} = \left(\cos\left(\frac{T\|\hat{\omega}_k\|}{2}\right)I_4 + \frac{T}{2}\mathrm{sinc}\left(\frac{T\|\hat{\omega}_k\|}{2}\right)A\left(\hat{\omega}_k\right)\right)\hat{Q}_k \tag{4.10}$$

$$\hat{b}_{k+1} = T\left(-k_b\hat{b}_k + k_b\mathrm{sat}_\Delta(\hat{b}_k) + \sigma_{b,k}\right) + \hat{b}_k \tag{4.11}$$

where $\mathrm{sinc}(x) = \sin(x)/x, \ \forall x \neq 0 \in \mathbb{R}$. For computational efficiency, the functions $\cos(x)$ and $\mathrm{sinc}(x)$ can be approximated by

$$\cos(x) = 1 - \frac{x^2}{2!} + \frac{x^4}{4!} + \cdots \qquad \mathrm{sinc}(x) = 1 - \frac{x^2}{3!} + \frac{x^4}{5!} \cdots \tag{4.12}$$

4.2 Control Design

Let Q_d be the desired attitude to be tracked, generated by

$$\dot{Q}_d = \begin{bmatrix} -q_d^\top \\ \eta I_3 + S(q_d) \end{bmatrix}\omega_d \tag{4.13}$$

where $Q_d := \begin{bmatrix} \eta_d, \ q_d^\top \end{bmatrix}^\top$. The attitude tracking error is represented by $R_e := R_d^\top R$, which corresponds to the unit quaternion $Q_e := Q_d^{-1} \odot Q$ and is defined as

$$Q_e = \begin{pmatrix} \eta_e \\ q_e \end{pmatrix} = \begin{pmatrix} \eta_d\eta + q^\top q_d \\ \eta_d q - \eta q_d - q_d \times q \end{pmatrix} \tag{4.14}$$

Differentiating both sides of equation $Q_d \odot Q_e = Q$ with respect to time, one has

$$\dot{Q}_d \odot Q_e + Q_d \odot \dot{Q}_e = \dot{Q} \tag{4.15}$$

Then the time derivative of Q_e can be derived as follows:

$$\begin{aligned}
\dot{Q}_e &= Q_d^{-1} \odot \dot{Q} - Q_d^{-1} \odot \dot{Q}_d \odot Q_e \\
&= \frac{1}{2}Q_d^{-1} \odot Q \odot Q_\omega - \frac{1}{2}Q_d^{-1} \odot Q_d \odot Q_{\omega_d} \odot Q_e \\
&= \frac{1}{2}Q_e \odot Q_\omega - \frac{1}{2}Q_{\omega_d} \odot Q_e \\
&= \frac{1}{2}Q_e \odot Q_\omega - \frac{1}{2}Q_e \odot Q_e^{-1} \odot Q_{\omega_d} \odot Q_e \\
&= \frac{1}{2}Q_e \odot Q_\omega - \frac{1}{2}Q_e \odot Q_{\tilde{\omega}_d} \\
&= \frac{1}{2}Q_e \odot Q_{\omega_e} \tag{4.16}
\end{aligned}$$

Using the fact that $Q_e^{-1} \odot Q_{\omega_d} \odot Q_e = Q_{\tilde{\omega}_d}$ where $\tilde{\omega}_d = R_e^\top \omega_d$ and $\omega_e = \omega - \tilde{\omega}_d$, and assuming that Q_d is constant (or slowly varying), *i.e.*, $\omega_d \approx 0$, the attitude error dynamics can be rewritten as

$$\dot{Q}_e = \begin{bmatrix} -\frac{1}{2} q_e^\top \omega \\ \frac{1}{2}(\eta_e I_3 + S(q_e))\omega \end{bmatrix} \quad (4.17)$$

using the fact $\omega_d = 0$ and $\omega_e = \omega$. Motivated by the well known PD-like attitude stabilization control law proposed in [39]

$$\tau = -\alpha q - \Gamma_1 \omega \quad (4.18)$$

where, α is a positive scalar and Γ_1 is a symmetric positive definite matrix. The following attitude control law is proposed:

$$\tau = -\alpha q_e - \Gamma_1 \omega \quad (4.19)$$

Under the proposed control law (4.19), the closed loop dynamics are given by

$$\dot{q}_e = \frac{1}{2}(\eta_e I_3 + S(q_e))\omega$$
$$I_f \dot{\omega} = -\omega \times I_f \omega - \alpha q_e - \Gamma_1 \omega \quad (4.20)$$

Theorem 4.1. [39] Consider (2.22) and (2.23) under the control law (4.19). Then, the equilibrium point $(\eta_e = 1, q_e = 0, \omega = 0)$ is almost globally asymptotically stable.

Proof. The time derivative of the following Lyapunov function candidate:

$$V = \alpha q_e^\top q_e + \alpha(1 - \eta_e)^2 + \frac{1}{2}\omega^\top I_f \omega \quad (4.21)$$

can be written as follows

$$\begin{aligned} \dot{V} &= 2\alpha q_e^\top \dot{q}_e + 2\alpha(\eta_e - 1)\dot{\eta}_e + \omega^\top I_f \dot{\omega} \\ &= \alpha q_e^\top \left((\eta_e I_3 + S(q_e))\omega \right) - \alpha(\eta_e - 1)\left(q_e^\top \omega \right) + \omega^\top (\tau - S(\omega)I_f \omega) \\ &= \alpha\eta_e q_e^\top \omega - \alpha\omega^\top S(q_e)q_e - \alpha\eta_e q_e^\top \omega + \alpha q_e^\top \omega - \alpha\omega^\top q_e - \omega^\top \Gamma_1 \omega - \omega^\top S(\omega)I_f \omega \\ &= -\omega^\top \Gamma_1 \omega \end{aligned} \quad (4.22)$$

which implies that $\omega(t), q_e(t)$ and η_e are bounded. Applying the LaSalle's invariance theorem, one can conclude that $\lim_{t\to\infty} \omega(t) = 0$, and consequently $\dot{\omega}$ tends to be zero. Therefore, in view of the second equation in (4.20), one has $\lim_{t\to\infty} q_e(t) = 0$. Using the fact that $\eta_e^2 + q_e^\top q_e = 1$, one can easily show that $\lim_{t\to\infty} \eta_e = \pm 1$. One can also show that the equilibrium point $(q_e = 0, \eta_e = 1, \omega = 0)$ is an attractor while the equilibrium point $(q_e = 0, \eta_e = -1, \omega = 0)$ is a repeller (*i.e.*, unstable).

$\square$

Remark 1. Since the attitude of the quadrotor can not be directly measured. The real attitude Q will be replaced by the estimated attitude $\hat{Q}$ as discussed in the previous section. On the other hand, the angular velocity measurements can be corrected using the estimated gyro bias $\hat{b}$. Therefore, the PD-like control law (4.19) can be modified using the estimated attitude and gyro bias as:

$$\tau = -\alpha \hat{q}_e - \Gamma_1(\omega_{\mathcal{B}} - \hat{b}) \tag{4.23}$$

where, $\hat{Q}_e := [\hat{\eta}_e \ \hat{q}_e^\top]^\top = Q_d^{-1} \odot \hat{Q}$. This modified controller will be implemented in our real-time experimental tests.

4.3 Simulation Results

In this section, we illustrate through simulation results the performance of the nonlinear observer (4.7) and the effectiveness of the PD-like controller (4.19) with unit quaternion representation. The simulations are carried out for the following scenario: an IMU is fixed to the center of a quadrotor UAV to measure the inertial vectors. The inertial vectors expressed in the inertial frame $\mathcal{I}$ are taken based on the local actual values as $a_{\mathcal{I}} = (0, 0, -9.81)^\top$ and $m_{\mathcal{I}} = (0.1550, -0.010, 0.5453)^\top$.

4.3.1 Simulation 1 - Attitude Estimation

The gains and parameters involved in the observer (4.3-4.6) are given by [23]

$$k_1 = 1, k_2 = 0.5, k_3 = k_1/32, k_4 = k_2/32, k_b = 25, \Delta = 0.03 \tag{4.24}$$

The P-gain k_1 is chosen larger than k_2 due to the fact that the measurements of the gravity direction are more reliable than the measurements of the geomagnetic field. Small values of k_3 and k_4 are chosen in order to reduce the integral wind-up effects. Large value of k_b is chosen to obtain a fast desaturation rate of the bias estimation.

In this simulation, we assume that there is no noise in the gyroscope and accelerometer measurements. However, an additive white Gaussian noise of variance 0.3 is considered in the magnetometer measurements. A constant gyro-bias vector $b_g = [0.01, -0.005, -0.01]^\top$ (deg /s) is introduced. The initial estimated Euler angles are chosen as $\hat{\phi}(0) = -45 \deg, \hat{\theta}(0) = 45 \deg$ and $\hat{\psi}(0) = 90 \deg$, and the actual angles are considered constants for all time, *i.e.,* $\phi(t) = 0 \deg, \theta(t) = 0 \deg, \psi(t) = 0 \deg$. The initial estimated gyro-bias is taken as $\hat{b}(0) = (0, 0, 0)^\top$.

The results presented in Fig. 4.1 and Fig. 4.2 show the effective performance of the nonlinear observer. One can see that a very fast convergence of the estimated variables to the actual values, and the quasi absence of overshoot of the estimated attitude despite the use of the integral correction term $\hat{b}$ and the large initial estimation errors. It can also be seen that the magnetic disturbance do not degrade the estimation performance of the roll and pitch estimates as well as the first and second components of the gyro-bias estimate $\hat{b}$.
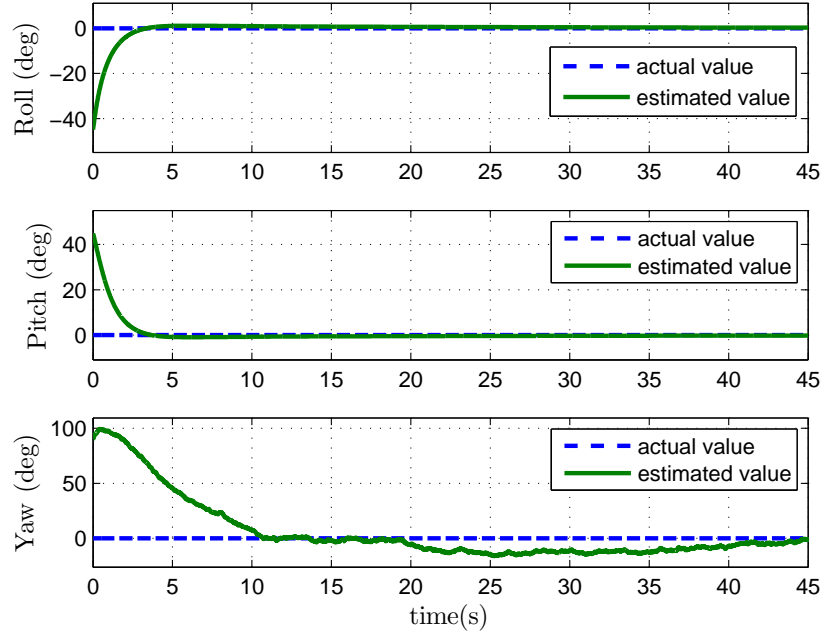
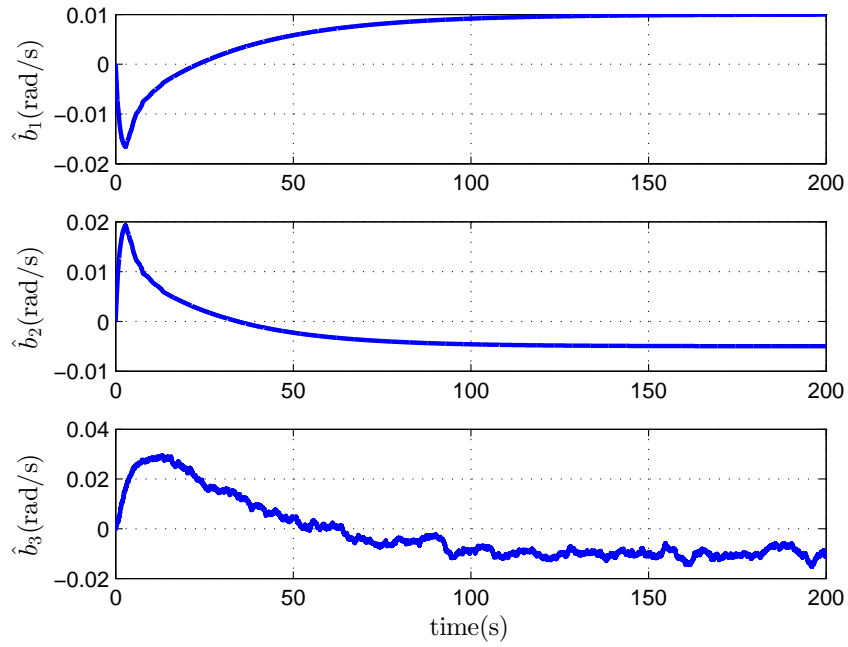Figure 4.1: Static attitude estimation with gyro-bias

Figure 4.2: Gyro-bias estimation

4.3.2 Simulation 2 - Attitude Control

To show the effectiveness of the PD-like controller (4.23), simulation for attitude control has been carried out. An overview of the control scheme I is presented in Fig. 4.3. As we can see, the control torque is designed with the desired attitude, the observed attitude and the corrected angular velocity given in (4.10)-(4.11).
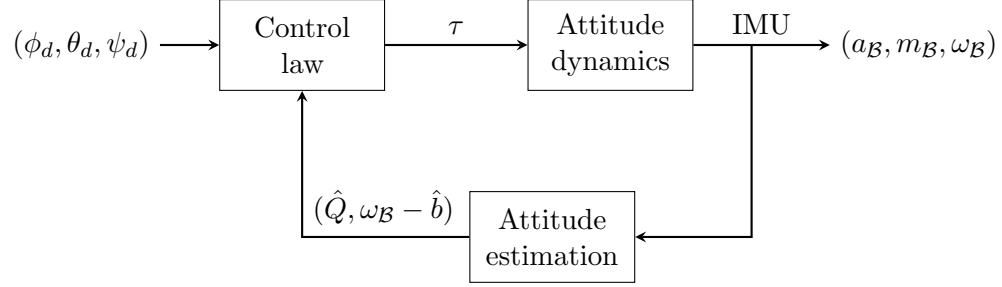

Figure 4.3: Control scheme I

The inertia matrix of the quadrotor has been taken as $I_f = \mathrm{diag}(0.0159, 0.0150, 0.0297)$ given in Section 3.2. The control gains involved in the PD-like controller (4.23) have been chosen as

$$\alpha = 6.0 \qquad \Gamma_1 = \mathrm{diag}([0.4368, \ 0.4243, \ 0.5970]) \tag{4.25}$$

where, Γ_1 is calculated from the linearized second-order dynamics of the roll, pitch and yaw by setting damping ratio to 1. The gains and parameters for the attitude estimator (4.10)-(4.11) are taken the same as (4.24) used in the simulation. The following initial conditions are considered as: $Q(0) = (0.9685, -0.1744, 0.1694, -0.0548)^\top$ (*i.e.*, $\phi(0) = -22 \deg, \theta(0) = 18 \deg$ and $\psi(0) = -10 \deg$), $\omega(0) = (0, 0, 0)^\top$, $\hat{Q}(0) = (0.9655, -0.1472, 0.1919, -0.0967)^\top$ (*i.e.*, $\hat{\phi}(0) = -20 \deg, \hat{\theta}(0) = 20 \deg$ and $\hat{\psi}(0) = -15 \deg$). The desired attitude is chosen as $\phi_d = 0 \deg, \theta_d = 0 \deg$ and $\psi_d = 0 \deg$, which has been simplified to the attitude stabilization problem.

Simulation results are shown in Fig. 4.4 and Fig. 4.5. Fig. 4.4 shows the evolution of the Euler angles and angular velocity with respect to time. We can clearly see fast convergence of the actual roll, pitch and yaw angles to the desired zero angles. Also Fig. 4.5 shows that the estimated attitude converges to the actual attitude fast enough. The slight overshoot of the yaw may be caused by the visible delay in the yaw estimation.

4.4 Experimental Results

In order to explore the real-time performance of the attitude estimator (4.10)-(4.11) and attitude controller (4.23), two experiments are performed on our 3DR quadrotor platform mentioned in Chapter 3.
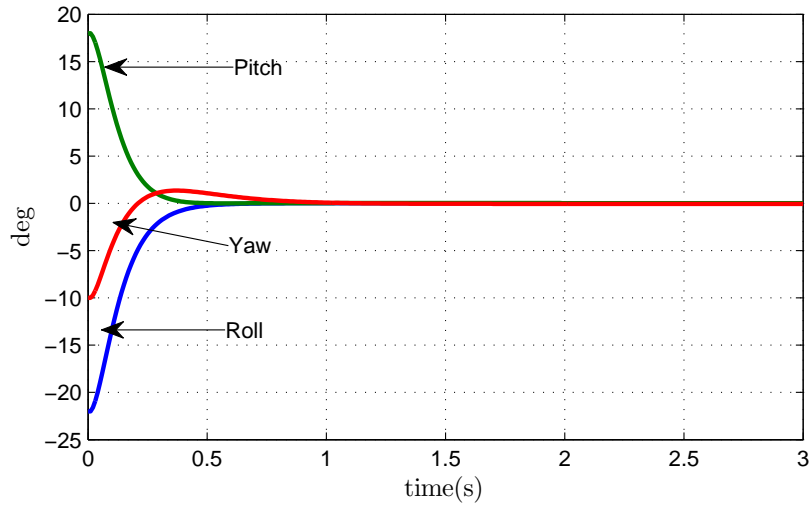
(a) Attitude in Euler angles
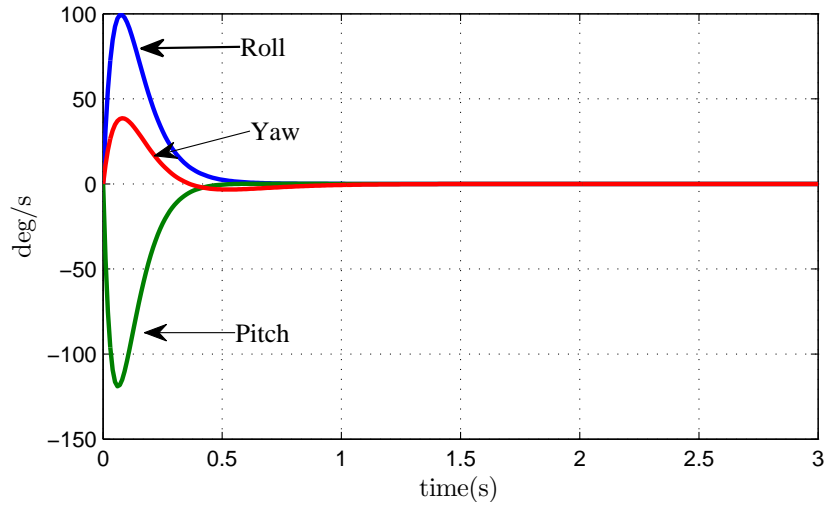
(b) Angular velocity

Figure 4.4: PD-like attitude control with attitude estimation

4.4.1 Experiment 1 - Attitude Estimation

The proposed discrete version of the attitude estimator (4.10)-(4.11), are implemented on our Autopilot system. The gains and parameters involved in the estimator are taken the same as (4.24). The experimental results are reported in Fig. 4.6 and Fig. 4.7. The estimated attitude is converted into the roll, pitch and yaw angles for visualization. Regarding the estimation of the yaw angles in Fig. 4.7, the presence of visible estimation errors may be explained by the fact that the inertial magnetic field vector might be slightly perturbed by the electrical equipment in the lab. However, the presence of magnetic disturbances does not prevent the estimates of the roll and pitch angles to converge to the actual values.
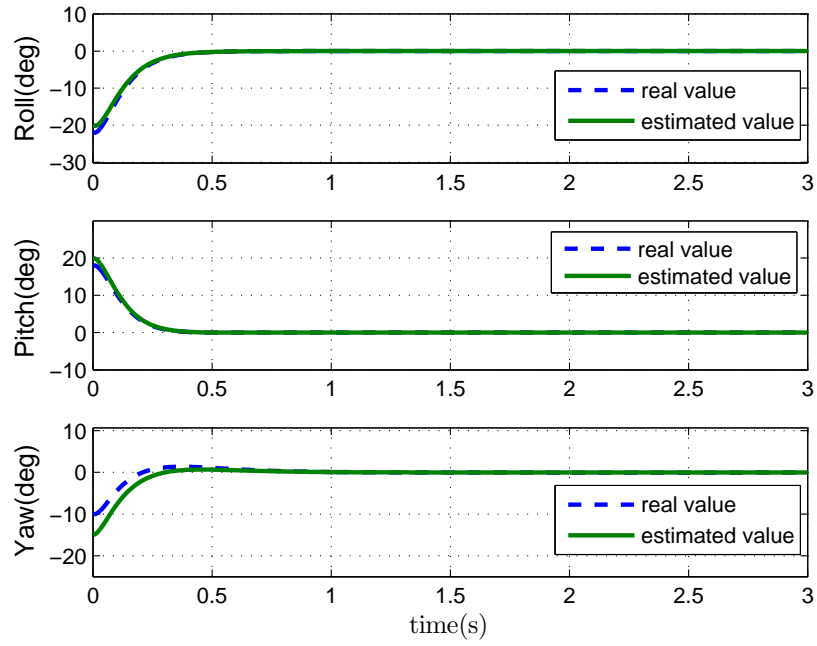
Figure 4.5: Comparison of the actual attitude and the estimated attitude
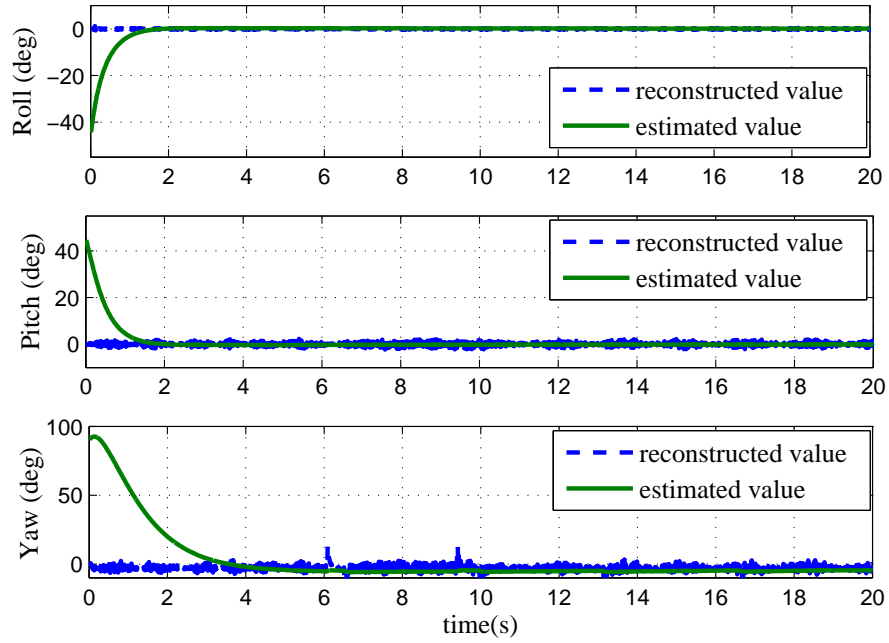
Figure 4.6: Real-time estimation for static attitude
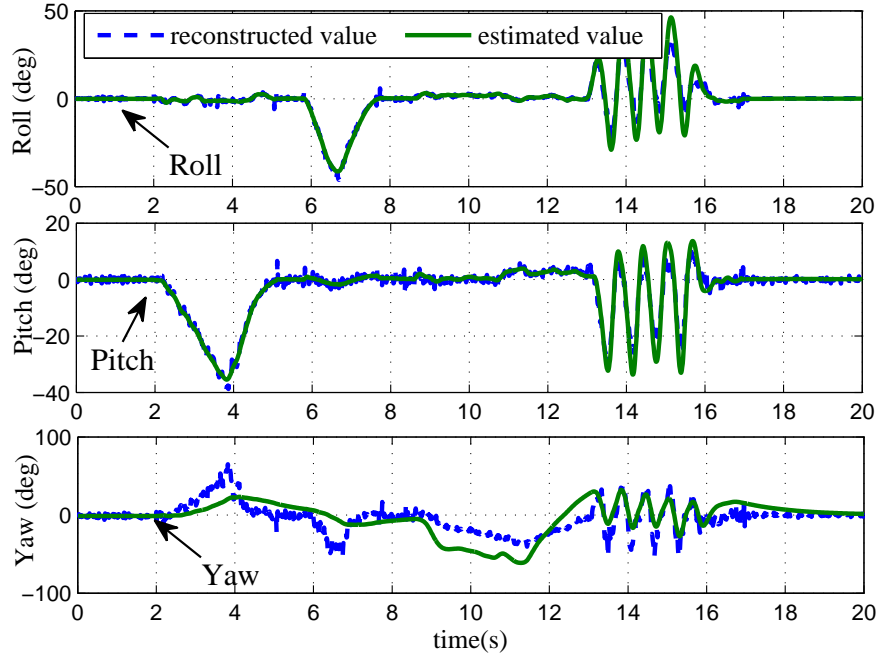
Figure 4.7: Real-time estimation for time-varying attitude

4.4.2   Experiment 2 - Attitude Control

In this experiment, the quadrotor is flown off the ground and its attitude is stabilized to $R = I_3$ (*i.e.,* $\phi = 0\,\mathrm{deg}$, $\theta = 0\,\mathrm{deg}$ and $\psi = 0\,\mathrm{deg}$) during the hover time. For the case of hovering, the total thrust of the motors should be equal to the gravity force. The experiment is performed with the attitude estimator (4.10) and (4.11), and the attitude control law (4.23). The gains involved in the controller are chosen as follows by trail-and-error:

$$\alpha = 5.0 \qquad \Gamma_1 = \mathrm{diag}([0.44,\ 0.42,\ 0.60]) \tag{4.26}$$

The performance of the real-time attitude stabilization is shown in Fig. 4.8. Fig. 4.8(a) shows Euler angles of the quadrotor. It can be seen that the control system ensures the Euler angles remain always between $(-5\,\mathrm{deg}, +5\,\mathrm{deg})$. Similarly, the angular velocity presented in Fig. 4.8(b) are relatively small.
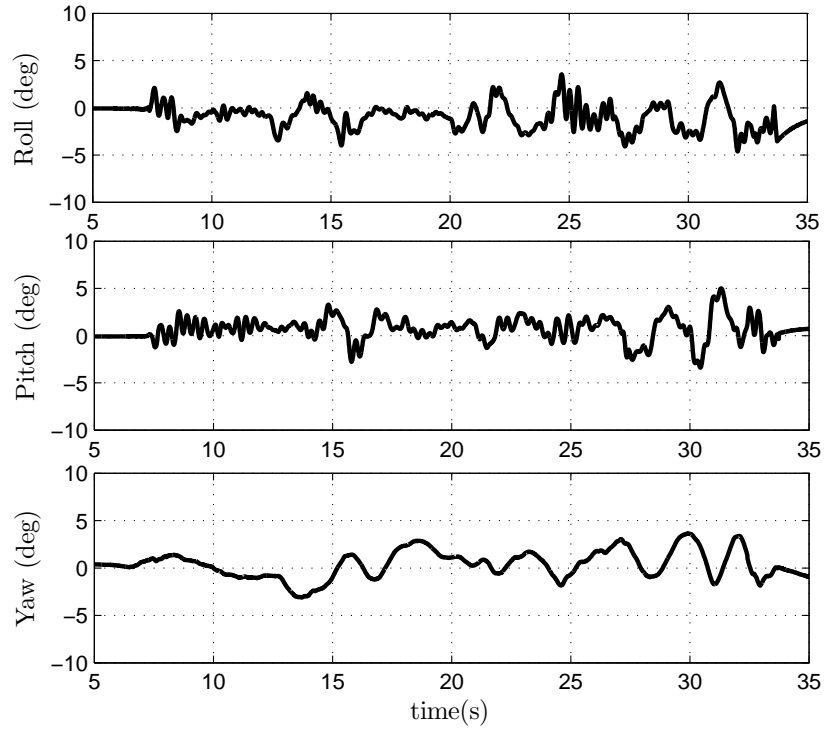
(a) Attitude in Euler angles
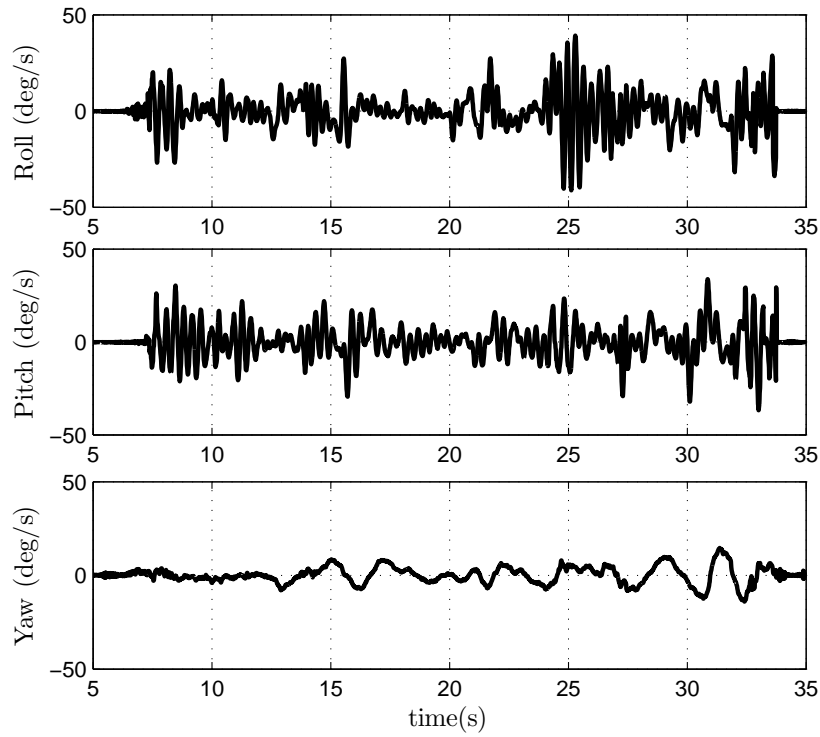
(b) Angular velocity

Figure 4.8: Experimental results for attitude stabilization

Chapter 5

Attitude Control Using Inertial Vector Measurements

Due to the unavailability of sensors that directly measure the attitude, suitable attitude observers are designed to reconstruct the attitude from the angular velocity and inertial vector measurements provided by an IMU. However, extra care has to be taken when the attitude estimation algorithm is combined with an attitude control scheme since the separation principle does not systematically hold for nonlinear systems. To overcome the above mentioned issue, a nonlinear controller relying on the inertial measurements without attitude reconstruction has been tested experimentally on our quadrotor system. The techniques of vectors decoupling and filtering are used to improve the performance. Both the simulation results and experimental resutls have been presented.

5.1 Control Design

Consider the dynamics of the desired attitude (4.13), let us define $R_{\bar{e}} := RR_d^\top$ as a new tracking error, which corresponds to the unit quaternion $Q_{\bar{e}} = (\eta_{\bar{e}}, q_{\bar{e}})$ and is given by

$$Q_{\bar{e}} \;=\; Q \odot Q_d^{-1} \tag{5.1}$$

$$=\; \begin{bmatrix} \eta_d \eta + q^\top q_d \\ \eta_d q - \eta q_d - q \times q_d \end{bmatrix} \tag{5.2}$$

Note that $Q_{\bar{e}}$ is different from Q_e defined in (4.14). However, $Q_{\bar{e}}$ and Q_e are related by $Q_{\bar{e}} = Q_d \odot Q_e \odot Q_d^{-1}$, and when $R_d = I_3$ one has

$$Q_e = Q_{\bar{e}} \tag{5.3}$$

Similarly, the time derivative of $Q_{\bar{e}}$ can be derived as follows:

$$
\begin{aligned}
\dot{Q}_{\bar{e}} &= \dot{Q} \odot Q_d^{-1} - Q_{\bar{e}} \odot \dot{Q}_d \odot Q_d^{-1} \\
&= \frac{1}{2} Q \odot Q_\omega \odot Q_d^{-1} - \frac{1}{2} Q_{\bar{e}} \odot Q_d \odot Q_{\omega_d} \odot Q_d^{-1} \\
&= \frac{1}{2} Q_{\bar{e}} \odot Q_d \odot Q_\omega \odot Q_d^{-1} - \frac{1}{2} Q_{\bar{e}} \odot Q_d \odot Q_{\omega_d} \odot Q_d^{-1} \\
&= \frac{1}{2} Q_{\bar{e}} \odot Q_{\omega_{\bar{e}}}
\end{aligned}
\tag{5.4}
$$

where $\omega_{\bar{e}} = R_d(\omega - \omega_d)$. In the case $\omega_d = 0$, we have $\omega_{\bar{e}} = R_d\omega$. Then, the tracking-error dynamics of $Q_{\bar{e}}$ are governed by

$$
\dot{Q}_{\bar{e}} = \begin{bmatrix} -\frac{1}{2} q_{\bar{e}}^\top R_d \omega \\ \frac{1}{2}(\eta_{\bar{e}} I_3 + S(q_{\bar{e}})) R_d \omega \end{bmatrix}
\tag{5.5}
$$

The explicit inertial measurements based controller can be easily generated from [44] and is given by

$$
\tau = z_\rho - \Gamma_2 \omega
\tag{5.6}
$$

$$
z_\rho := \sum_{i=1}^{n} \rho_i S(R_d^\top r_i) b_i
\tag{5.7}
$$

where $r_i \in \mathbb{R}^3, i = 1, \ldots, n \geq 2$ are known and constant inertial vectors expressed in the inertial frame $\mathcal{I}$, where at least two vectors are not collinear. $b_i \in \mathbb{R}^3, i = 1, \ldots, n \geq 2$ are the vector measurements of r_i expressed in the body-attached frame $\mathcal{B}$. Obviously, the vectors r_i and b_i are related by $b_i = R^\top r_i$. Parameters ρ_i for $i = 1, \ldots, n$ are positive constant gains, and Γ_2 is chosen as a positive definite matrix. Before stating the main results, a useful lemma is stated as follows:

Lemma 1. [44] Assume that at least two vectors, among the n inertial vectors, are collinear. Then the following statements hold:

1) The following matrix

$$
W_\rho = -\sum_{i=1}^{n} \rho_i S(r_i)^2
\tag{5.8}
$$

   is positive definite.

2) The following equality holds

$$
z_\rho = -2R_d^\top(\eta_{\bar{e}} I_3 - S(q_{\bar{e}})) W_\rho q_{\bar{e}}
\tag{5.9}
$$

3) Equation $z_\rho = 0$ is equivalent to

$$
(\eta_{\bar{e}} = 0, q_{\bar{e}} = v_\rho) \quad \text{or} \quad (\eta_{\bar{e}} = \pm 1, q_{\bar{e}} = 0)
$$

   where v_ρ are the unit eigenvectors of W_ρ.

Proof. The proof for Lemma 2 is straightforward (see Lemma 1 in [44], for more details) and omitted here. $\qquad\square$

Under the control law (5.6) and the attitude dynamics (2.22) and (2.23), the closed-loop error dynamics are given by

$$\begin{aligned}
\dot{q}_{\bar{e}} &= \frac{1}{2}(\eta_{\bar{e}}I_3 + S(q_{\bar{e}}))R_d\omega \\
I_f\dot{\omega} &= -S(\omega)I_f\omega - 2R_d^\top(\eta_{\bar{e}}I_3 - S(q_{\bar{e}}))W_\rho q_{\bar{e}} - \Gamma_2\omega
\end{aligned} \tag{5.10}$$

where, $z_\rho = -2R_d^\top(\eta_{\bar{e}}I_3 - S(q_{\bar{e}}))W_\rho q_{\bar{e}}$. Note that the desired attitude R_d is constant, and the closed-loop dynamics (5.10) are autonomous.

Let $\chi := (q_{\bar{e}}, \omega) \in D \times \mathbb{R}^3$ be the state vector, with $D := \{x \in \mathbb{R}^3 \mid \|x\| \leq 1\}$. Now, one can state the following theorem.

Theorem 5.1. Consider (2.22) and (2.23) under the control law 5.6. Assume that n vector measurements b_i, corresponding to the inertial vectors $r_i, i = 1, \cdots, n \geq 2$ are available, and at least two vectors, among the n inertial vectors, are non-collinear. Then the following statements hold:

1) The equilibria of the closed-loop dynamics (5.10) are given by $(q_{\bar{e}}, \omega) = (0,0) \cup (v_\rho, 0)$, where, v_ρ are the unit eigenvectors of W_ρ.

2) The equilibrium point $(0,0)$ is locally asymptotically stable with the domain of attraction containing the following domains:

$$\Phi_1 = \{\chi \in D \times \mathbb{R}^3 | \chi^\top P\chi \leq c\} \tag{5.11}$$

where, $\chi := (q_{\bar{e}}, \omega)$, $P = \mathrm{diag}(2W_\rho, \frac{1}{2}I_f)$, $c < 2\min\{\lambda(W_\rho)\}$ and $\lambda(x)$ is the eigenvalues of matrix (x).

3) The equilibria $(v_\rho, 0)$ are unstable and equilibrium point $(0,0)$ is almost globally asymptotically stable.

Proof. Consider the positive definite, radially unbounded, function $V : D \times \mathbb{R}^3 \to \mathbb{R}_{\geq 0}, D := \{x \in \mathbb{R}^3 | \|x\| \leq 1\}$, defined as

$$V = 2q_{\bar{e}}^\top W_\rho q_{\bar{e}} + \frac{1}{2}\omega^\top I_f\omega \tag{5.12}$$

Define $e_i := R_d^\top r_i - b_i$. Using the fact that, $r_i^\top S(q_{\bar{e}})r_i = 0$ and $R^\top R = RR^\top = I_3$, one can

show that

$$
\begin{aligned}
\frac{1}{2}\sum_{i=1}^{n}\rho_i e_i^\top e_i &= \frac{1}{2}\sum_{i=1}^{n}\rho_i(R_d^\top r_i - b_i)^\top(R_d^\top r_i - b_i) \\
&= \frac{1}{2}\sum_{i=1}^{n}\rho_i(R_d^\top r_i - R^\top r_i)^\top(R_d^\top r_i - R^\top r_i) \\
&= \frac{1}{2}\sum_{i=1}^{n}\rho_i(r_i^\top R_d R_d^\top r_i + r_i^\top R R^\top r_i - r_i^\top R R_d^\top r_i - r_i^\top R_d R^\top r_i) \\
&= \frac{1}{2}\sum_{i=1}^{n}\rho_i(2r_i^\top r_i - r_i^\top R R_d^\top r_i - r_i^\top R_d R^\top r_i) \\
&= \frac{1}{2}\sum_{i=1}^{n}\rho_i\left(2\|r_i\|^2 - r_i^\top(R_{\bar{e}} + R_{\bar{e}}^\top)r_i\right) \\
&= \sum_{i=1}^{n}\rho_i\left(\|r_i\|^2 - r_i^\top(I_3 + 2S(q_{\bar{e}})^2)r_i\right) \\
&= -2\sum_{i=1}^{n}\rho_i\left(r_i^\top S(q_{\bar{e}})^2 r_i\right) \\
&= q_{\bar{e}}^\top\left(-\sum_{i=1}^{n}\rho_i S(r_i)^2\right)q_{\bar{e}} \\
&= 2q_{\bar{e}}^\top W_\rho q_{\bar{e}} \tag{5.13}
\end{aligned}
$$

Using the fact $\dot{R} = RS(\omega)$, one can also show that the dynamics of e_i is governed by

$$
\dot{e}_i = -\dot{b}_i = -\dot{R}^\top r_i = S(\omega)R^\top r_i = -S(b_i)\omega \tag{5.14}
$$

Consequently, one can rewrite (5.12) as follows:

$$
V = \frac{1}{2}\sum_{i=1}^{n}\rho_i e_i^\top e_i + \frac{1}{2}\omega^\top I_f \omega \tag{5.15}
$$

whose time-derivative along the trajectories of (2.23) and (5.14), is given by

$$
\begin{aligned}
\dot{V} &= \sum_{i=1}^{n}\rho_i e_i^\top \dot{e}_i + \omega^\top I_f \dot{\omega} \\
&= \sum_{i=1}^{n}\rho_i e_i^\top(-S(b_i)\omega) + \omega^\top(-\omega \times I_f\omega + \tau + G_a) \\
&= -\sum_{i=1}^{n}\rho_i(R_d^\top r_i)^\top S(b_i)\omega + \omega^\top \tau \\
&= -\omega^\top\sum_{i=1}^{n}\rho_i S(R_d^\top r_i)b_i + \omega^\top(z_\rho - \Gamma_2\omega) \\
&= -\omega^\top\Gamma_2\omega \le 0 \tag{5.16}
\end{aligned}
$$

Since the closed-loop dynamics (5.10) are autonomous, one can use LaSalle's invariance theorem. Setting $\dot{V} \equiv 0$ leads to $\omega \equiv 0$ and then $\dot{\omega} \equiv 0$. From the second equation in (5.10), it follows that $\tau \equiv 0$. Then one can conclude from (5.6) that $z_\rho \equiv 0$, which, in view of Lemma 1, implies that $(Q_{\bar{e}} \equiv (\pm 1, 0^\top)^\top)$ or $(Q_{\bar{e}} \equiv (0, v_\rho^\top)^\top)$. It is clear that the largest invariant set for the closed-loop system, characterized by $\dot{V} = 0$ is given by $(0,0) \cup (v_\rho, 0)$

Since we showed that $\dot{V} \le 0$, one has $V(\chi(t)) \le V(\chi(0))$, for all $t \ge 0$, which shows that Φ_1 is a positively invariant set. Since $V(\chi) \ge 2\lambda_{min}(W_\rho)\|q_{\bar{e}}\|^2$, it is clear that $\min_{\|q_{\bar{e}}\|=1} V(\chi) = 2\min\{\lambda(W_\rho)\}$. It is clear that the equilibria $(v_\rho, 0)$ do not belong to Φ_1. Finally, since the largest invariant set in Φ_1, corresponding to $\dot{V} = 0$, is nothing else but $(0,0)$, the second claim of the theorem is proved.

Now we need to show that the equilibria $(v_\rho, 0)$ are unstable, using Chetaev arguments [69]. Introducing the change of variables $Q_x = (\eta_x, q_x) = (0, -v_\rho) \odot Q_{\bar{e}}$, then $Q_{\bar{e}}$ can be rewritten as

$$\begin{bmatrix} \eta_{\bar{e}} \\ q_{\bar{e}} \end{bmatrix} = \begin{bmatrix} 0 \\ v_\rho \end{bmatrix} \odot \begin{bmatrix} \eta_x \\ q_x \end{bmatrix} = \begin{bmatrix} -q_x^\top v_\rho \\ \eta_x v_\rho + S(v_\rho)q_x \end{bmatrix} \tag{5.17}$$

It is clear that the equilibrium $(q_{\bar{e}} = v_\rho, \omega = 0)$ is equivalent to $(q_x = 0, \omega = 0)$, where q_x is the vector part of the unit quaternion Q_x. The dynamics with new variables are given by

$$\begin{aligned} \dot{Q}_x &= \frac{1}{2}Q_x \odot Q_{\omega_{\bar{e}}} \\ I_f\dot{\omega} &= -\omega \times I_f\omega + z_\rho - \Gamma_2\omega \end{aligned} \tag{5.18}$$

where, z_ρ can be rewritten as

$$\begin{aligned} z_\rho &= -2R_d^\top(\eta_{\bar{e}}I_3 - S(q_{\bar{e}}))W_\rho q_{\bar{e}} \\ &= -2R_d^\top((-q_x^\top v_\rho)I_3 - S(\eta_x v_\rho + S(v_\rho)q_x))W_\rho(\eta_x v_\rho + S(v_\rho)q_x) \\ &= 2R_d^\top((q_x^\top v_\rho)I_3 + \eta_x S(v_\rho) + q_x v_\rho^\top - v_\rho q_x^\top)(\eta_x \lambda_\rho v_\rho + W_\rho S(v_\rho)q_x) \\ &= 2R_d^\top(q_x^\top v_\rho W_\rho S(v_\rho)q_x + \eta_x S(v_\rho)W_\rho S(v_\rho)q_x + \eta_x \lambda_\rho q_x + v_\rho q_x^\top W_\rho S(v_\rho)q_x) \end{aligned} \tag{5.19}$$

The linearized dynamics of (5.18) is given by

$$\begin{aligned} \dot{q}_x &= \frac{1}{2}\sigma R_d\omega \\ I_f\dot{\omega} &= 2\sigma R_d^\top M_\rho q_x - \Gamma_2\omega \end{aligned} \tag{5.20}$$

where, $\sigma = \pm 1$ and $M_\rho = \lambda_\rho I_3 + S(v_\rho)W_\rho S(v_\rho)$. It is easy to check that M_ρ is symmetric matrix with eigenvalues $\lambda_\rho, \bar{\lambda}_1 := \lambda_\rho - \lambda_1$ and $\bar{\lambda}_2 := \lambda_\rho - \lambda_2$. Let us consider the following Chetaev function:

$$\mathcal{V}(q_x, \omega) = 4q_x^\top M_\rho q_x - \omega^\top I_f\omega \tag{5.21}$$

where, $\mathcal{V}(0,0) = 0$. Define the set $B_r = \{x := (q_x, \omega)^\top \in D \times \mathbb{R}^3 \mid \|x(t)\| < r\}$, where $r > 0$ is arbitrarily close to zero. Let us define U_r a subset of B_r that is, $U_r = \{x \in B_r \mid \mathcal{V}(x) > 0\}$. Note that U_r is a non-empty set contained in B_r, since $\mathcal{V}(\epsilon v_\rho, 0) = \epsilon^2 \lambda_\rho > 0$ for all $\epsilon^2 < r$. The time derivative of $\mathcal{V}$, in view of (5.20), is given by

$$\begin{aligned} \dot{\mathcal{V}} &= 8q_x^\top M_\rho \dot{q}_x - 2\omega^\top I_f\dot{\omega} \\ &= 4\sigma q_x^\top M_\rho R_d\omega - 2\omega^\top(2\sigma R_d^\top M_\rho q_x - \Gamma_2\omega) \\ &= 2\omega^\top \Gamma_2\omega \end{aligned} \tag{5.22}$$

where, $\dot{\mathcal{V}}$ is positive semi-definite everywhere in U_r for all $r > 0$. Therefore, for any initial conditions $x(0) \in U_r$, $x(t)$ must leave U_r, since $\mathcal{V}(x)$ is bounded in U_r and $\dot{\mathcal{V}}$ is positive semi-definite everywhere in U_r. Since $\mathcal{V}(x) > \mathcal{V}(0)$, $x(t)$ must leave U_r through the circle $\|x\| = r$ and not through the edges $\mathcal{V}(x) = 0$. Hence the equilibrium points $(v_\rho, 0)$ are unstable.

To show that the stable manifolds associated to unstable equilibria have Lebesgue measure zero, we take a look at the Jacobian matrix of the closed-loop linearized dynamics (5.20)

$$A = \begin{bmatrix} 0 & \frac{1}{2}\sigma R_d \\ 2\sigma I_f^{-1} R_d^\top M_\rho & -I_f^{-1} \Gamma_2 \end{bmatrix} \tag{5.23}$$

Since $\mathrm{Tr}(A) = -\mathrm{Tr}(I_f^{-1}\Gamma_2) \neq 0$, it is clear that the eigenvalues of A are not all imaginary. This guarantees that stable manifolds associated to the unstable equilibria have zero Lebesgue measure. Finally, one concludes that the equilibrium point $(q_{\bar{e}} = 0, \omega = 0)$ is almost globally asymptotically stable. □

'

5.2 Implementation with IMUs

5.2.1 Standard Implementation with IMUs

As mentioned in Chapter 3, the IMU fixed to our quadrotor consists of a three-axis gyroscope, a three-axis accelerometer and a three-axis magnetometer. The standard implementation of the explicit controller (5.6) based on inertial measurements is given by

$$\tau = \rho_1 S(R_d^\top \bar{a}_\mathcal{I})\bar{a}_\mathcal{B} + \rho_2 S(R_d^\top \bar{m}_\mathcal{I})\bar{m}_\mathcal{B} - \Gamma_2 \omega \tag{5.24}$$

where ρ_1 and ρ_2 are positive gains and Γ_2 is a positive definite matrix, and the normalized vectors are given by

$$\bar{a}_\mathcal{I} := e_3 \qquad \bar{m}_\mathcal{I} := \frac{m_\mathcal{I}}{|m_\mathcal{I}|} \qquad \bar{a}_\mathcal{B} := \frac{-a_\mathcal{B}}{g} \quad \bar{m}_\mathcal{B} := \frac{m_\mathcal{B}}{|m_\mathcal{B}|}$$

Let us coin this control scheme as standard controller to distinguish it with the decoupled controller proposed in this section later.

Obviously, from Theorem 5.1, the actual attitude of the quadrotor will converge to the desired attitude asymptotically for almost all initial conditions with the standard controller (5.24). However, the standard implementation of the controller (5.24) encounters some issues since the two vectors e_3 and $\bar{m}_\mathcal{I}$ are close to each other. For discussion purposes and without loss of generality, let us take a look at the problem of the quadrotor stabilization (*i.e.,* $R_d = I_3$). Then

1) The closed-loop dynamics of the roll, pitch and yaw are highly coupled. This implies that the stabilization errors of yaw strongly affect the stabilization dynamics of the roll and pitch. This issue can be observed by taking a close look at the linearized closed-loop dynamics (5.10) around the equilibrium point $(q_{\bar{e}} = 0, \omega = 0)$, which is given by

$$
\begin{aligned}
\dot{q}_{\bar{e}} &= \frac{1}{2}\sigma\omega \\
I_f\dot{\omega} &= -2\sigma W_\rho q_{\bar{e}} - \Gamma_2\omega
\end{aligned}
\tag{5.25}
$$

where, using the fact that $z_\rho = -2R_d^\top(\eta_{\bar{e}}I_3 - S(q_{\bar{e}}))W_\rho q_{\bar{e}}$ from Lemma 1. and W_ρ can be specified as

$$
W_\rho = \begin{bmatrix} \rho_1 + \rho_2(1 - \bar{m}_1^2) & -\rho_2\bar{m}_1\bar{m}_2 & -\rho_2\bar{m}_1\bar{m}_3 \\ -\rho_2\bar{m}_2\bar{m}_1 & \rho_1 + \rho_2(1 - \bar{m}_2^2) & -\rho_2\bar{m}_2\bar{m}_3 \\ -\rho_2\bar{m}_3\bar{m}_1 & -\rho_2\bar{m}_3\bar{m}_2 & \rho_2(1 - \bar{m}_3^2) \end{bmatrix}
$$

The linearized system can be rewritten as the following second-order dynamics

$$
I_f\ddot{x} + \Gamma_2\dot{x} + W_\rho x = 0
\tag{5.26}
$$

where, $x := (\sigma\phi, \sigma\theta, \sigma\psi)^\top = 2\sigma q_{\bar{e}}$ for small ϕ, θ, ψ angles. In practice, the normalized gravity vector and geomagnetic field vector (*i.e.*, $\bar{a}_{\mathcal{I}}$ and $\bar{m}_{\mathcal{I}}$) can be "ill-conditioned" in the sense that they are very close to each other (for example, $\bar{a}_{\mathcal{I}} = (0, 0, 1)^\top$ and $\bar{m}_{\mathcal{I}} = (0.2734, -0.0178, 0.9617)^\top$ in Thunder Bay, ON., Canada). In such case, the third component of $\bar{m}_{\mathcal{I}}$ is dominant to its first and second ones. Let us assume that $\bar{m}_2^2 \approx 0$ and $\bar{m}_3^2 \gg \bar{m}_1^2$, then the dynamics of the roll, pitch and yaw can be simplified as

$$
I_\phi\ddot{\phi} + \Gamma_\phi\dot{\phi} + (\rho_1 + \rho_2(1 - \bar{m}_1^2))\phi - \rho_2\bar{m}_1\bar{m}_3\psi = 0
\tag{5.27}
$$

$$
I_\theta\ddot{\theta} + \Gamma_\theta\dot{\theta} + (\rho_1 + \rho_2)\theta = 0
\tag{5.28}
$$

$$
I_\psi\ddot{\psi} + \Gamma_\psi\dot{\psi} + \rho_2(1 - \bar{m}_3^2)\psi - \rho_2\bar{m}_1\bar{m}_3\phi = 0
\tag{5.29}
$$

where, Γ_2 has been chosen as $diag(\Gamma_\phi, \Gamma_\theta, \Gamma_\psi)$. In view of (5.27) and (5.29), the dynamics of the roll and pitch (*i.e.*, ϕ and ψ) are strongly coupled with each other.

2) Magnetic disturbance and bias influence the dynamics of the roll, pitch and yaw angles. In many applications, especially for the small-size electric motorized aerial robots, significant magnetic disturbances are almost unavoidable, leading significant time-varying deterministic errors between $m_\mathcal{B}$ and $R^\top m_\mathcal{I}$. This not only leads to large errors of the yaw angles but also nonnegligible errors in the roll and pitch stabilization.

3) The ill-conditioning of the two vectors $\bar{a}_{\mathcal{I}}$ and $\bar{m}_{\mathcal{I}}$ may also lead to the difficulty of finding "nonhigh" gains (ρ_1, ρ_2) leading to a fast time response. To show the slow response, let us neglect the coupling term in the dynamics (5.29) (*i.e.*, in the case $\phi = 0$) and rewrite it as

$$
I_\psi\ddot{\psi} + \Gamma_\psi\dot{\psi} + \rho_2(1 - \bar{m}_3^2)\psi = 0
\tag{5.30}
$$

where, the eigenvalues of the second-order dynamics (5.30) can be obtained as

$$\lambda_1 = -\frac{\Gamma_\psi}{2I_\psi}\left(1 - \sqrt{1 - \frac{4\rho_2(1 - \bar{m}_3^2)I_\psi}{\Gamma_\psi^2}}\right) \approx -\frac{\rho_2(1 - \bar{m}_3^2)}{\Gamma_\psi}$$

$$\lambda_2 = -\frac{\Gamma_\psi}{2I_\psi}\left(1 + \sqrt{1 - \frac{4\rho_2(1 - \bar{m}_3^2)I_\psi}{\Gamma_\psi^2}}\right)$$

Since $1 - \bar{m}_3^2 \approx 0.0751 \ll 1$, the less negative eigenvalue λ_1 will be very close to zero if ρ_2 is not chosen sufficiently high, which leads to a slow response for the dynamics of yaw. However, increasing the value of ρ_2 amplifies the noise and increases the coupling effect.

5.2.2 Implementation with Vector Decoupling

Considering the following vectors as (4.1)

$$u_\mathcal{I} := e_3, \qquad v_\mathcal{I} := \frac{\pi_{u_\mathcal{I}} m_\mathcal{I}}{\|\pi_{u_\mathcal{I}} m_\mathcal{I}\|} \qquad u_\mathcal{B} := -\frac{a_\mathcal{B}}{g}, \qquad v_\mathcal{B} := \frac{\pi_{u_\mathcal{B}} m_\mathcal{B}}{\|\pi_{u_\mathcal{B}} m_\mathcal{B}\|} \tag{5.31}$$

with $\pi_x = \|x\|^2 I_3 - xx^\top, \forall x \in \mathbb{R}^3$, denoting the orthogonal projection on the plane orthogonal to vector x. From the definitions of $v_\mathcal{I}$, one has $v_\mathcal{I} = [v_1, v_2, 0]^\top$, where $v_1^2 + v_2^2 = 1$.

Consider the following control law:

$$\begin{aligned} \tau &= z_\rho - \Gamma\omega \\ z_\rho &:= \rho_1 S(R_d^\top u_\mathcal{I})u_\mathcal{B} + \rho_2 S(R_d^\top v_\mathcal{I})v_\mathcal{B} \end{aligned} \tag{5.32}$$

Let us coin this control scheme a partially decoupled controller to distinguish it with the fully decoupled controller proposed in this section later. Obviously, from Theorem 5.1, the decoupled controller (5.32) guarantees almost-global convergence of the attitude of the quadrotor to the desired attitude. The following properties hold:

1) In the presence of a constant magnetic disturbance field or a magnetic bias, the dynamics of the roll and pitch still converge to the desired roll and pitch angles for almost all initial conditions.

2) For the attitude stabilization, the dynamics of the roll and pitch are locally decoupled from the dynamics of yaw.

Decoupling of Roll/Pitch Dynamics from Magnetic Bias

Let us assume that the magnetometer measurements are influenced by a constant(or slowly time varying) magnetic bias in the inertial frame. Define $m_\mathcal{I}^b$ as the biased magnetic field

expressed in inertial frame, which is different from the geomagnetic field $m_{\mathcal{I}}$. Therefore, magnetometer measurement $m_{\mathcal{B}} = R^\top m_{\mathcal{I}}^b \neq R^\top m_{\mathcal{I}}$ and consequently $v_{\mathcal{B}} \neq R^\top v_{\mathcal{I}}$. In this case, one has $v_{\mathcal{B}} = R^\top v_{\mathcal{I}}^b$, where $v_{\mathcal{I}}^b$ is also a unit constant vector orthogonal to $u_{\mathcal{I}}$ but different from $v_{\mathcal{I}}$. Assume that there exists a unique constant angle $\Theta \in [0; \pi)$ such that

$$v_{\mathcal{I}}^b = \cos \Theta v_{\mathcal{I}} + \sin \Theta (u_{\mathcal{I}} \times v_{\mathcal{I}})$$

Using the Rodrigues's rotation formula, a constant rotation matrix can be constructed as follow

$$R_b = I_3 + \sin \Theta u_{\mathcal{I}\times} + 2(\sin \frac{\Theta}{2})^2 (u_{\mathcal{I}\times})^2$$

One verifies that $R_b u_{\mathcal{I}} = u_{\mathcal{I}}$ and

$$
\begin{aligned}
R_b v_{\mathcal{I}} &= v_{\mathcal{I}} + \sin \Theta (u_{\mathcal{I}\times} v_{\mathcal{I}}) + 2(\sin \frac{\Theta}{2})^2 (u_{\mathcal{I}\times})^2 v_{\mathcal{I}} \\
&= v_{\mathcal{I}} + 2(\sin \frac{\Theta}{2})^2 (u_{\mathcal{I}} u_{\mathcal{I}}^\top - |u_{\mathcal{I}}| I_3) v_{\mathcal{I}} + \sin \Theta (u_{\mathcal{I}\times} v_{\mathcal{I}}) \\
&= v_{\mathcal{I}} - 2(\sin \frac{\Theta}{2})^2 v_{\mathcal{I}} + \sin \Theta (u_{\mathcal{I}\times} v_{\mathcal{I}}) \\
&= \cos \Theta v_{\mathcal{I}} + \sin \Theta (u_{\mathcal{I}\times} v_{\mathcal{I}}) = v_{\mathcal{I}}^b
\end{aligned}
$$

Define $\bar{R}_b = R_b^\top R$ and $\tilde{\bar{R}} = \bar{R} R_d^\top$, then the feedback term z_ρ can be modified as

$$
\begin{aligned}
z_\rho &= \rho_1 S(R_d^\top u_{\mathcal{I}}) u_{\mathcal{B}} + \rho_2 S(R_d^\top v_{\mathcal{I}}) v_{\mathcal{B}} \\
&= \rho_1 S(R_d^\top u_{\mathcal{I}}) R^\top u_{\mathcal{I}} + \rho_2 S(R_d^\top v_{\mathcal{I}}) R^\top v_{\mathcal{I}}^b \\
&= \rho_1 S(R_d^\top u_{\mathcal{I}}) R^\top R_b R_b^\top u_{\mathcal{I}} + \rho_2 S(R_d^\top v_{\mathcal{I}}) R^\top R_b v_{\mathcal{I}} \\
&= \rho_1 S(R_d^\top u_{\mathcal{I}}) \bar{R}_b^\top u_{\mathcal{I}} + \rho_2 S(R_d^\top v_{\mathcal{I}}) \bar{R}_b^\top v_{\mathcal{I}} \qquad (5.33)
\end{aligned}
$$

From Theorem 5.1, one verifies that $(\bar{R}_b(t), \omega(t)) \to (R_d, 0)$ as $t \to \infty$ for almost all initial conditions with decoupled control law (5.32) and magnetic biased inertial measurements feedback (5.33). Using the fact $\bar{R}_b^\top u_{\mathcal{I}} \to R_d^\top u_{\mathcal{I}}$ as $t \to \infty$, one deduces that

$$
\bar{R}_b^\top u_{\mathcal{I}} = R^\top \begin{bmatrix} 0 \\ 0 \\ 1 \end{bmatrix} = \begin{bmatrix} -S\theta \\ S\phi C\theta \\ C\phi C\theta \end{bmatrix} \to R_d^\top u_{\mathcal{I}} = \begin{bmatrix} -S\theta_d \\ S\phi_d C\theta_d \\ C\phi_d C\theta_d \end{bmatrix}
$$

which implies that the roll, pitch angles ϕ, θ converge to the desired angles ϕ_d and θ_d, respectively. It is worth noting that, the decoupled controller ensures an almost-global convergence for the roll and pitch in the presence of a constant bias on the magnetic field.

Local Decoupling of Roll/Pitch Dynamics from Yaw Dynamics

For the problem of attitude stabilization using the decoupled controller (5.32), one has the following linear dynamics

$$I_f \ddot{x} + \Gamma \dot{x} + W_\rho x = 0 \qquad (5.34)$$

where, $x := (\sigma\phi, \sigma\theta, \sigma\psi)^\top$, and the positive definite matrix W_ρ with decoupled vectors is given by

$$W_\rho = \begin{bmatrix} \rho_1 + \rho_2(1 - v_1^2) & -\rho_2 v_1 v_2 & 0 \\ -\rho_2 v_2 v_1 & \rho_1 + \rho_2(1 - v_2^2) & 0 \\ 0 & 0 & \rho_2 \end{bmatrix}$$

Then, the linearized closed-loop dynamics of the roll, pitch and yaw angles are given by

$$I_\phi \ddot\phi + \Gamma_\phi \dot\phi + (\rho_1 + \rho_2(1 - v_1^2))\phi - \rho_2 v_1 v_2 \theta = 0 \tag{5.35}$$
$$I_\theta \ddot\theta + \Gamma_\theta \dot\theta + (\rho_1 + \rho_2(1 - v_2^2))\theta - \rho_2 v_1 v_2 \phi = 0 \tag{5.36}$$
$$I_\psi \ddot\psi + \Gamma_\psi \dot\psi + \rho_2 \psi = 0 \tag{5.37}$$

Obviously, the dynamics of the roll and pitch (*i.e.*, ϕ and θ) are locally decoupled from the dynamics of the yaw (*i.e.*, ψ). The dynamics can be further simplified for the special case where $v_1^2 \gg v_2^2$ and $v_2^2 \approx 0$ (for example, in our case $v_\mathcal{I} = (0.9979, -0.0650, 0)^\top$).

$$I_\phi \ddot\phi + \Gamma_\phi \dot\phi + \rho_1 \phi = 0 \tag{5.38}$$
$$I_\theta \ddot\theta + \Gamma_\theta \dot\theta + (\rho_1 + \rho_2)\theta = 0 \tag{5.39}$$

The natural frequencies of the roll, pitch and yaw dynamics (5.37)-(5.39) depend only on two parameters ρ_1 and ρ_2. Practically, the value of ρ_2 is chosen much smaller than the value of ρ_1 to reduce the noise and the coupling effect.

In the general case, the problem of the coupling between the dynamics of the roll and pitch can be locally solved by introducing a third virtual inertial vector $\mu_\mathcal{I}$ and its measurement $\mu_\mathcal{B}$ given by

$$\mu_\mathcal{I} := u_\mathcal{I} \times v_\mathcal{I}, \qquad \mu_\mathcal{B} := u_\mathcal{B} \times v_\mathcal{B} \tag{5.40}$$

It is easy to check that $\mu_\mathcal{B} = R^\top \mu_\mathcal{I}$, since

$$u_\mathcal{B} \times v_\mathcal{B} = S(R^\top u_\mathcal{I})R^\top v_\mathcal{I} = R^\top(u_\mathcal{I} \times m_\mathcal{I})$$

Then, a modified fully decoupled controller is given by

$$\tau = \rho_1 S(R_d^\top u_\mathcal{I})u_\mathcal{B} + \rho_2 S(R_d^\top v_\mathcal{I})v_\mathcal{B} + \rho_3 S(R_d^\top \mu_\mathcal{I})\mu_\mathcal{B} - \Gamma\omega \tag{5.41}$$

Obviously, from Theorem 5.1, the fully decoupled controller (5.41) also guarantees the almost-global stability for the problem of attitude stabilization. From the controller (5.41), the matrix W_ρ can be rewritten as a diagonal matrix around the equilibrium point ($q_{\bar e} = 0, \omega = 0$):

$$W_\rho = \begin{bmatrix} \rho_1 + \rho_2(1 - v_1^2) + \rho_3(1 - v_2^2) & 0 & 0 \\ 0 & \rho_1 + \rho_2(1 - v_2^2) + \rho_3(1 - v_1^2) & 0 \\ 0 & 0 & \rho_2 + \rho_3 \end{bmatrix} \tag{5.42}$$

Then, one has the following linear dynamics

$$I_\phi \ddot\phi + \Gamma_\phi \dot\phi + (\rho_1 + \rho_2(1 - v_1^2) + \rho_3(1 - v_2^2))\phi = 0 \tag{5.43}$$
$$I_\theta \ddot\theta + \Gamma_\theta \dot\theta + (\rho_1 + \rho_2(1 - v_2^2) + \rho_3(1 - v_1^2))\theta = 0 \tag{5.44}$$
$$I_\psi \ddot\psi + \Gamma_\psi \dot\psi + (\rho_2 + \rho_3)\psi = 0 \tag{5.45}$$

The linear dynamics (5.43 - 5.45) guarantees local decoupling of the roll, pitch and yaw dynamics.

In particular, by choosing $\rho_1 = \rho_2 = \rho_3 = \rho$, the closed-loop dynamics (5.10) can be rewritten as

$$
\begin{aligned}
\dot{q}_e &= \frac{1}{2}(\eta_e I_3 + S(q_e))\omega \\
I_f \dot{\omega} &= -S(\omega)I_f\omega - 4\rho\eta_e q_e - \Gamma\omega
\end{aligned}
\tag{5.46}
$$

using the dynamics (4.17), and the fact that z_ρ can be rewritten as

$$
\begin{aligned}
z_\rho &= \sum_{i=1}^{n} \rho_i S(R_d^\top r_i) R_e^\top R_d^\top r_i \\
&= -2(\eta_e I_3 - S(q_e))R_d^\top W_\rho R_d q_e \\
&= -4\rho\eta_e q_e
\end{aligned}
\tag{5.47}
$$

The closed-loop dynamics (5.46) can be linearized around the equilibrium point Ω_1 as

$$
I_\phi \ddot{\phi}_e + \Gamma_\phi \dot{\phi}_e + 2\rho\phi_e = 0 \tag{5.48}
$$
$$
I_\theta \ddot{\theta}_e + \Gamma_\theta \dot{\theta}_e + 2\rho\theta_e = 0 \tag{5.49}
$$
$$
I_\psi \ddot{\psi}_e + \Gamma_\psi \dot{\psi}_e + 2\rho\psi_e = 0 \tag{5.50}
$$

where, $\phi_e = \phi - \phi_d$, $\theta_e = \theta - \theta_d$ and $\psi_e = \psi - \psi_d$, and Γ_2 has been chosen as $diag(\Gamma_\phi, \Gamma_\theta, \Gamma_\psi)$. From the dynamics (5.48)-(5.50), the error dynamics of the roll, pitch and yaw are locally decoupled. Moreover, by setting $\rho = \alpha/4$ *i.e.*, $W_\rho = (\alpha/2)I_3$, one can conclude that the closed-loop dynamics (4.20) and (5.46) have similar linearized second-order dynamics around the equilibrium point ($\eta_e = 1, q_e = 0, \omega = 0$). The second-order dynamics can be written as

$$
I_f \ddot{x} + \Gamma_2 \dot{x} + \alpha x = 0 \tag{5.51}
$$

where, $x = (\phi_e, \theta_e, \psi_e)^\top$.

5.3   Inertial Measurements Filtering

With the technique of vector decoupling, the actual attitude can converge to the desired attitude efficiently. However, another issue that may affect the performance of the quadrotor is the noise in the measurements provided by IMUs. Two popular methods of filtering: nonlinear complementary filter and Kalman-like filter, have been introduced in this section to clear the measurement noise and improve the real-time performance of the quadrotor.

5.3.1 Nonlinear Complementary Filtering

Motived by the nonlinear attitude estimation algorithm (4.3-4.6), one proposes the following nonlinear complementary filter for vector measurements

$$
\begin{aligned}
\dot{\hat{u}}_{\mathcal{B}} &= -S(\hat{\omega}_{\mathcal{B}})\hat{u}_{\mathcal{B}} \\
\dot{\hat{v}}_{\mathcal{B}} &= -S(\hat{\omega}_{\mathcal{B}})\hat{v}_{\mathcal{B}} \\
\hat{\omega}_{\mathcal{B}} &:= \omega_{\mathcal{B}} + k_1 u_{\mathcal{B}} \times \hat{u}_{\mathcal{B}} + k_2 \hat{u}_{\mathcal{B}} \hat{u}_{\mathcal{B}}^{\top}(v_{\mathcal{B}} \times \hat{v}_{\mathcal{B}})
\end{aligned}
\tag{5.52}
$$

where $\hat{u}_{\mathcal{B}}$ and $\hat{v}_{\mathcal{B}}$ are the estimates of $u_{\mathcal{B}}$ and $v_{\mathcal{B}}$, k_1 and k_2 are positive gains. The proof to show the convergence of the estimated vectors to the actual vectors is similar to the Theorem 1 in [23] and omitted here. The discrete version of the complementary filter over the period $(kT, (k+1)T]$ with small enough sampling time T, can be written as

$$
\begin{aligned}
\hat{u}_{\mathcal{B}_{k+1}} &= \exp\left(-TS(\hat{\omega}_{\mathcal{B}_k})\right)\hat{u}_{\mathcal{B}_k} \\
\hat{v}_{\mathcal{B}_{k+1}} &= \exp\left(-TS(\hat{\omega}_{\mathcal{B}_k})\right)\hat{v}_{\mathcal{B}_k}
\end{aligned}
\tag{5.53}
$$

The approximation of $\exp\left(-TS(\hat{\omega}_{\mathcal{B}_k})\right)$ is given by (see Appendix B for details):

$$
\exp\left(-TS(\hat{\omega}_{\mathcal{B}_k})\right) = \left(I_3 - T\text{sinc}(\Theta)S(\hat{\omega}_{\mathcal{B}_k}) + T^2\text{cosc}(\Theta)(S(\hat{\omega}_{\mathcal{B}_k}))^2\right)
\tag{5.54}
$$

where, $\Theta = T\|\hat{\omega}_{\mathcal{B}_k}\|$ and

$$
\begin{aligned}
\text{sinc}(x) &= \frac{\sin(x)}{x} = 1 - \frac{x^2}{3!} + \frac{x^4}{5!} - \frac{x^7}{7!} + \cdots \\
\text{cosc}(x) &= \frac{1 - \cos(x)}{x^2} = \frac{1}{2!} - \frac{x^2}{4!} + \frac{x^4}{6!} - \frac{x^6}{8!} + \cdots
\end{aligned}
$$

This approach guarantees that $\hat{u}_{\mathcal{B}_{k+1}}$ and $\hat{v}_{\mathcal{B}_{k+1}}$ remain within unit vectors (see details in [70]).

5.3.2 Kalman-Like Filtering

A predictor-corrector estimation introduced in [1] is applied using the dynamics of the vector measurements and angular velocity. Let $x[k]$ be the vector measurement at time t_k, and $u[k]$ be the input of the dynamics generating the vector measurement, such that

$$
x[k+1] = f(x[k], u[k])
\tag{5.55}
$$

We denote our estimate of the state at time step k, using measurements up to the time step j, by $\hat{x}[k|j]$ and the sensor measurements of the state at the time step $k+1$ by $\bar{x}[k+1]$. The update rule is then generated as follows:

$$
\begin{aligned}
\hat{x}[k+1|k] &= f(\hat{x}[k|k], u[k]) \\
\hat{x}[k+1|k+1] &= C\hat{x}[k+1|k] + (I - C)\bar{x}[k+1]
\end{aligned}
\tag{5.56}
$$

where, C is a diagonal tuning factor matrix. The elements $C_{ii} \in [0, 1]$ represent the relative weight of the prediction and measurements. Let $x[k]$ represent the inertial vector measurements ($u_{\mathcal{B}}[k]$ and $v_{\mathcal{B}}[k]$) expressed the rigid body frame at time t_k and $u[k]$ represent angular

velocity ($\omega_\mathcal{B}[k]$). The discrete-time version of the inertial vector measurements update law are given by

$$\hat{u}_\mathcal{B}[k+1|k+1] = Cu_\mathcal{B}[k+1] + (I_3 - C)\exp(-TS(\omega_\mathcal{B}[k]))\hat{u}_\mathcal{B}[k|k]$$
$$\hat{v}_\mathcal{B}[k+1|k+1] = Cv_\mathcal{B}[k+1] + (I_3 - C)\exp(-TS(\omega_\mathcal{B}[k]))\hat{v}_\mathcal{B}[k|k] \tag{5.57}$$

where, the diagonal matrix C is tuned by trial-and-error until acceptable performance is achieved.

5.4 Simulation Results

To explore the performance of each decoupled controller, a set of simulations have been performed. Fig. 5.1 is an overview of control scheme II
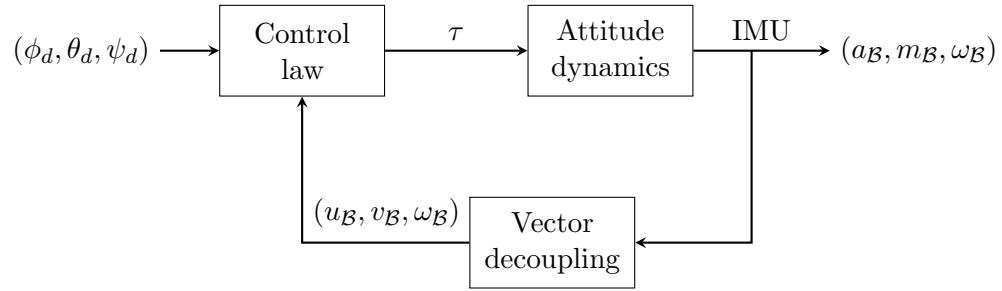

Figure 5.1: Control scheme II

5.4.1 Simulation 1 - Attitude Control

The moment of inertia and inertial vectors are chosen the same as those used in Chapter 4. Similarly, the initial conditions are taken as $\phi(0) = -22\deg$, $\theta(0) = 18\deg$, $\psi(0) = -10\deg$, $\omega = (0,0,0)^\top$, and the desired attitude is given by $\phi_d = 0\deg$, $\theta_d = 0\deg$, $\psi_d = 0\deg$. As discussed in Section 5.1, it is not easy to choose a set of gains for the standard inertial measurement based attitude controller. However, it is possible to choose these gains so as to obtain similar dynamics in the roll, pitch or yaw with those of the standard controller. The control parameters involved in the controllers (5.24), (5.32) and (5.41) are given in Table 5.1, allowing the linearized error system discussed in Section 5.1 to have similar dynamics in the pitch. Γ_2 is calculated from the linearized second-order dynamics of the roll, pitch and yaw by setting damping ratio to 1.

The results illustrated in Fig. 5.2 - 5.4 show important performance differences between the standard controller and the two decoupled controllers with the same control gains. As we can see, the roll and pitch converge to the desired roll and pitch angles with almost the same performance. However, significant differences in the performance of the yaw with standard controller have been shown in Fig. 5.3 and Fig. 5.4. One can observe, for the

Simulation 1	Simulation 2	Simulation 3
Controller (5.24)	Controller (5.32)	Controller (5.41)
$\rho_1 = 2.5 \quad \rho_2 = 0.5$		$\rho_1 = \rho_2 = \rho_3 = 1.5$
$\Gamma_2 = \text{diag}([0.4717, 0.4242, 0.2437])$		$\Gamma_2 = \text{diag}([0.4368, 0.4243, 0.5970])$

Table 5.1: Control gains for simulations

standard controller, a very slow convergence in the yaw angles, which is caused by the fact that the value of the third component of the magnetic field is close to 1. In contrast, a fast convergence of the yaw angles has been shown in Fig. 5.3 and an even faster convergence of the yaw is given in Fig. 5.4. The speed of the yaw dynamics in partially decoupled controller is limited by the choice of ρ_2. A higher value of ρ_2 can increase the speed of convergence, however, a higher noise will be introduced in the pitch dynamics.

5.4.2 Simulation 2 - Comparison with Magnetic Disturbance

The same gains involved in the controllers (5.32), (5.24) and (5.41) are used. In addition, each component of the measurements provided by the magnetometer is corrupted by an additive white Gaussian noise of variance 0.3. The initial conditions are taken as $\phi(0) = -45\,\text{deg}$, $\theta(0) = 45\,\text{deg}$, $\psi(0) = 90\,\text{deg}$, $\omega(0) = (0, 0, 0)^\top$, and the desired attitude is given by $\phi_d = 0\,\text{deg}$, $\theta_d = 0\,\text{deg}$, $\psi_d = 0\,\text{deg}$. The comparison results of the three controllers have been presented in Fig. 5.5. As we can see, the simulation results again show the different speeds of the convergence in the yaw dynamics. It also can been seen that, in the presence of the magnetic field disturbance, the magnetic disturbances do not degrade the performance of the error dynamics of the roll and pitch. On the other hand, a slightly higher noise on the yaw dynamics is a price to pay for a faster response.
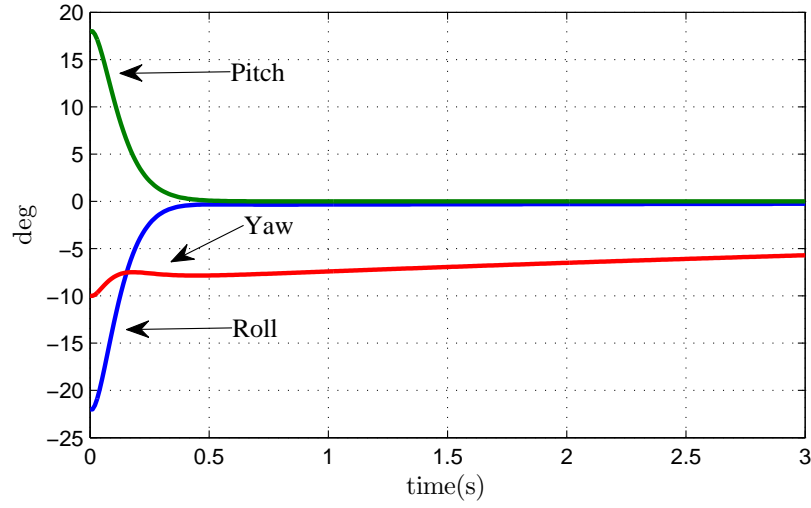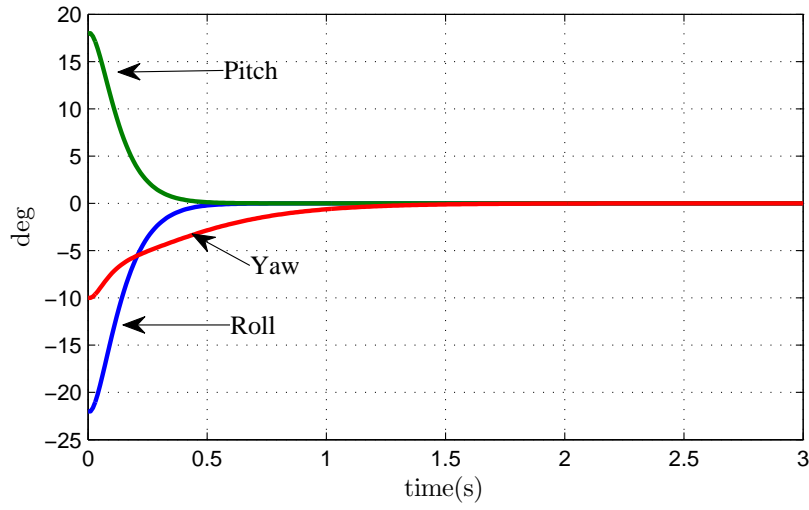
(a) Attitude in Euler angles
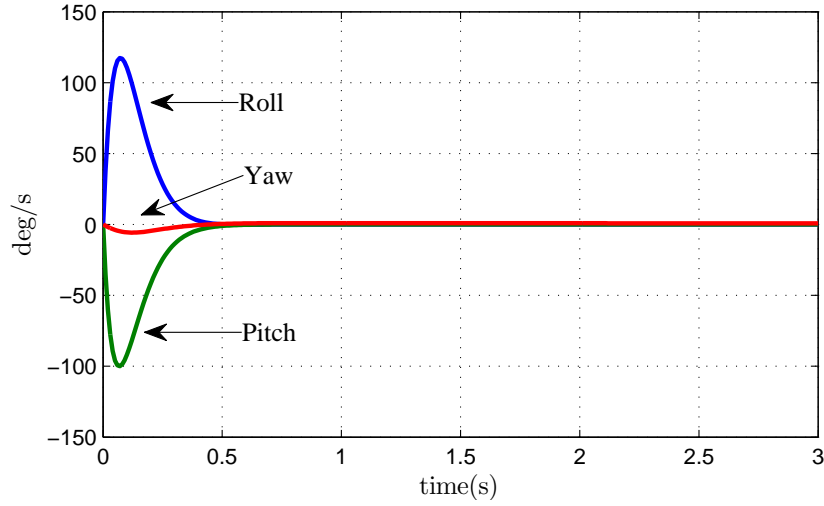
(b) Angular velocity

Figure 5.2: Attitude control without vector decoupling

5.5 Experimental Results

The experiment involves flying the quadrotor off the ground and stabilizing the attitude (Euler angles representation) of the quadrotor to zero (*i.e.,* $\phi_d = 0\,\mathrm{deg}, \theta_d = 0\,\mathrm{deg}, \psi_d = 0\,\mathrm{deg}$). Three experiments are performed with the gains shown in Table 5.2

Other settings are the same as those used in Chapter 4 and Chapter 5. Experimental results have been presented in Fig. 5.6 - 5.8. As shown in Fig. 5.6, Fig. 5.7 and Fig. 5.8, the proposed controllers perform well after taking off from the ground. The Euler angles in all the experiments remain aways between $(-5\,\mathrm{deg}, +5\,\mathrm{deg})$ and the angular velocity are

(a) Attitude in Euler angles
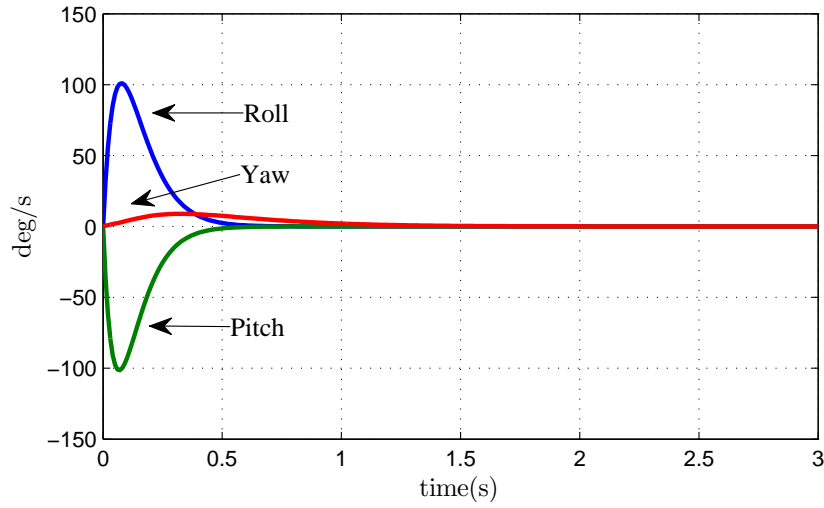
(b) Angular velocity

Figure 5.3: Attitude control with partially vector decoupling

Experiment 1	Experiment 2	Experiment 3
Controller (5.32)		Controller (5.41)
Complementary filter (5.53)	Kalman-like filter (5.56)	Complementary filter (5.53)
$\rho_1 = 2.6 \quad \rho_2 = 0.6$		$\rho_1 = \rho_2 = \rho_3 = 1.5$
$\Gamma_2 = \mathrm{diag}([0.44, 0.45, 0.29])$		$\Gamma_2 = \mathrm{diag}([0.44, 0.42, 0.60])$

Table 5.2: Control gains for experiments

relatively small.
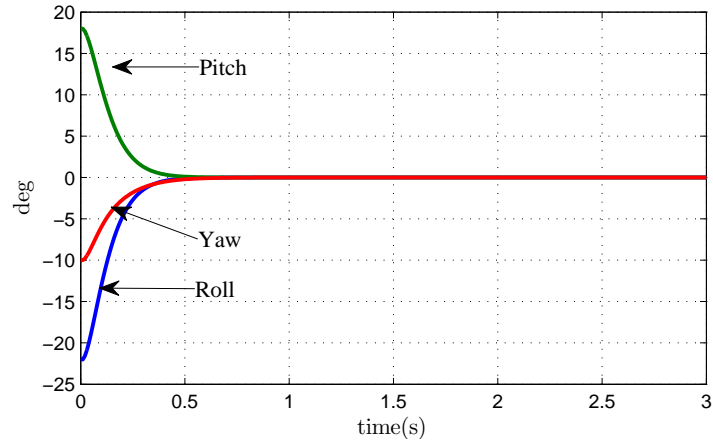
(a) Attitude in Euler angles
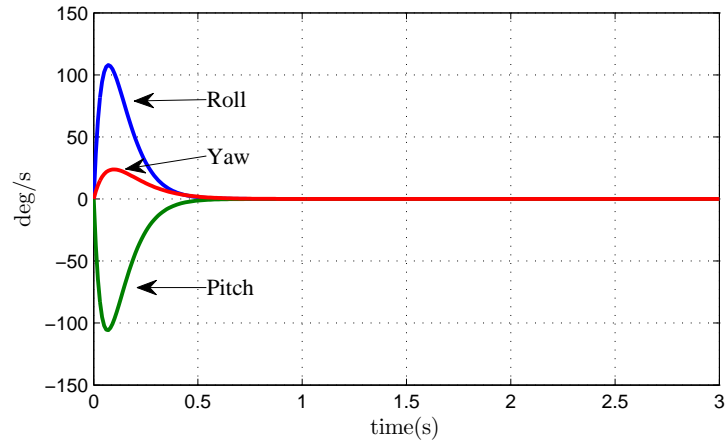
(b) Angular velocity

Figure 5.4: Attitude control with fully vector decoupling
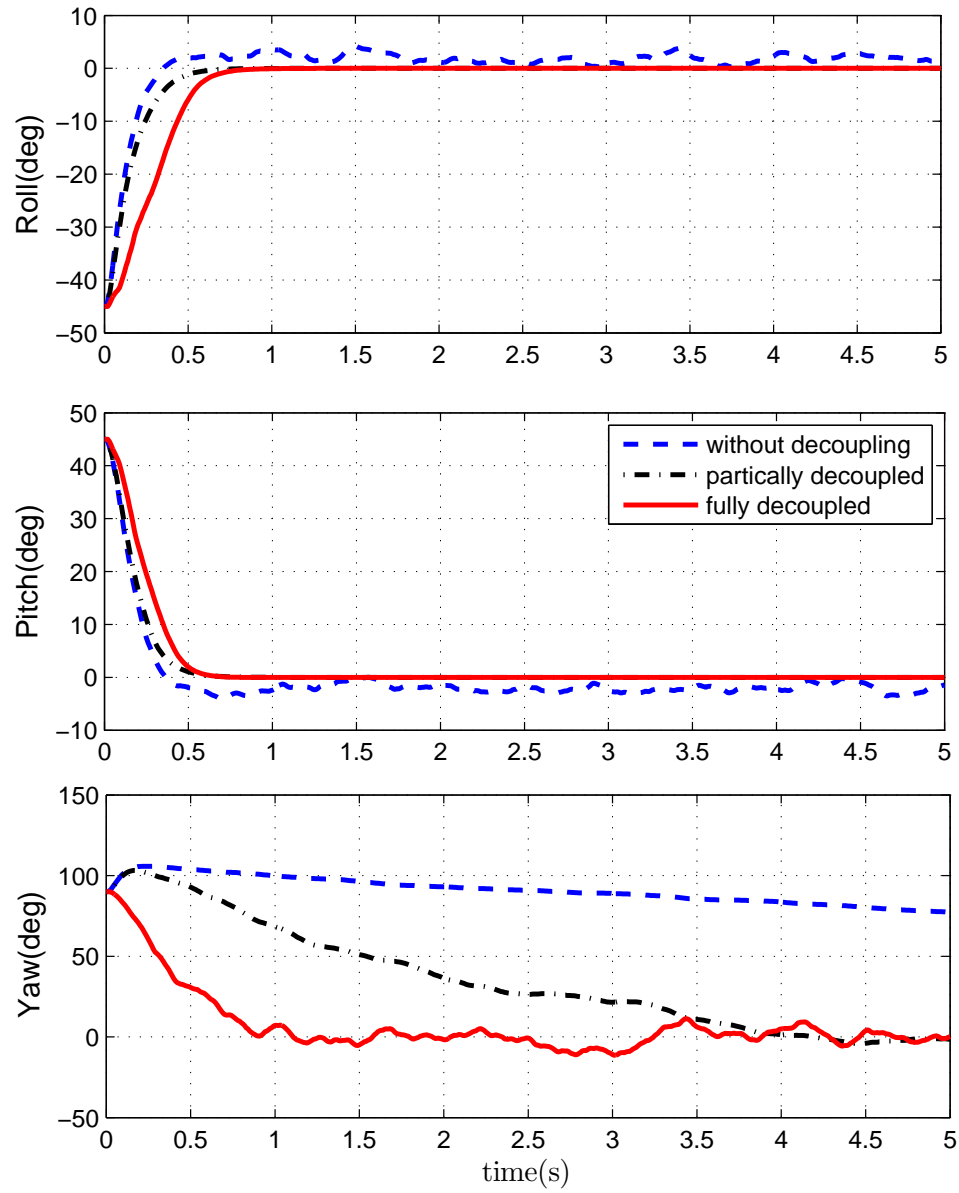
Figure 5.5: Attitude control comparison with magnetic disturbances
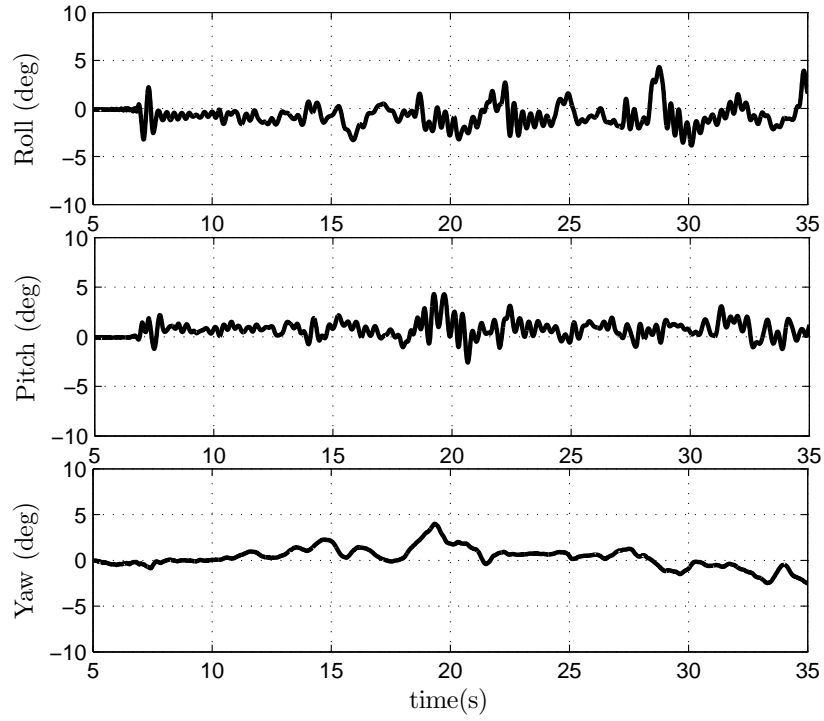
(a) Attitude in Euler angles
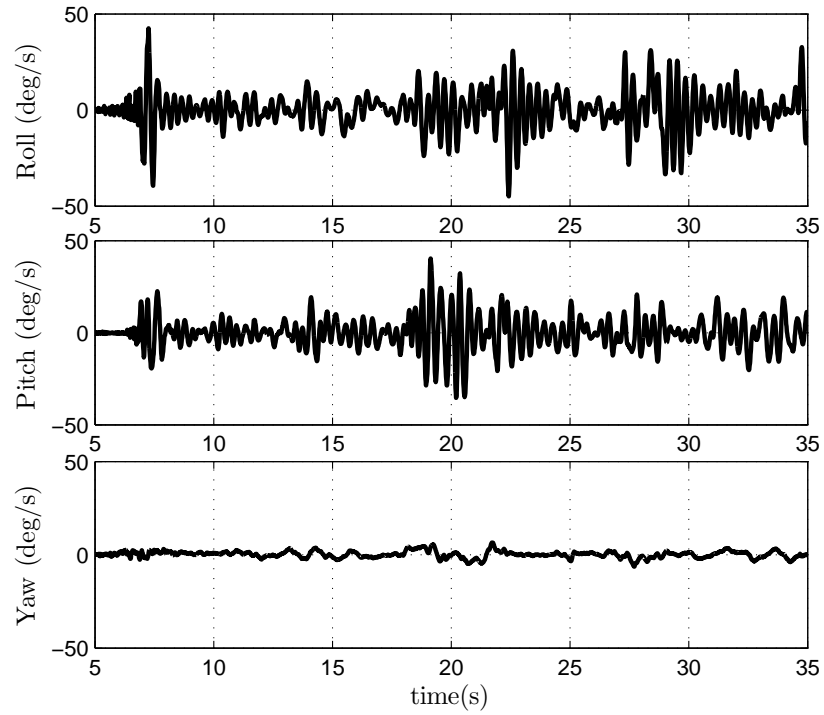
(b) Angular velocity

Figure 5.6: Attitude stabilization controller (5.24) and filter (5.53)

(a) Attitude in Euler angles

(b) Angular velocity

Figure 5.7: Attitude stabilization with controller (5.32) and filter (5.56)

(a) Attitude in Euler angles

(b) Angular velocity

Figure 5.8: Attitude stabilization with controller (5.41) and filter (5.53)
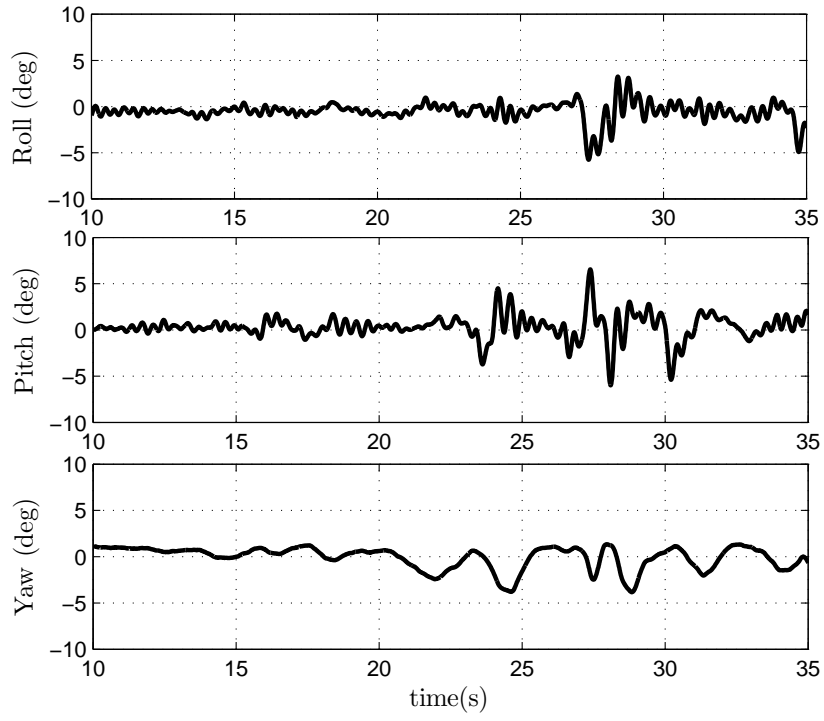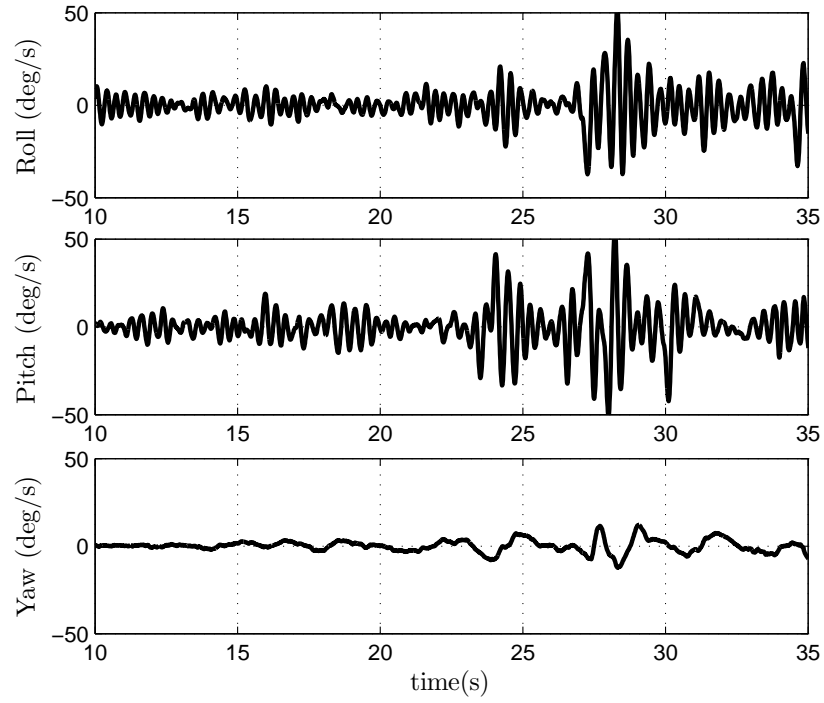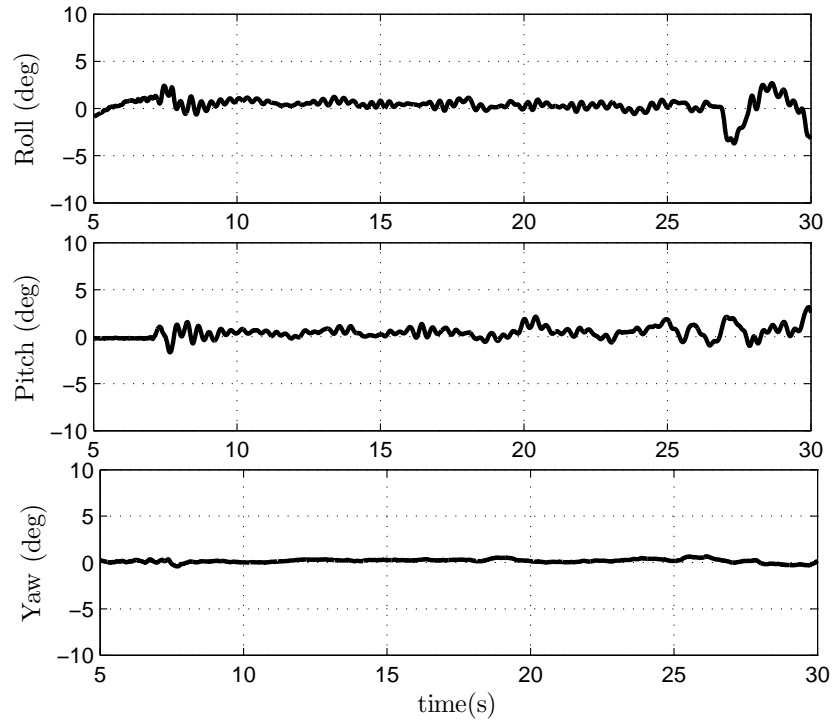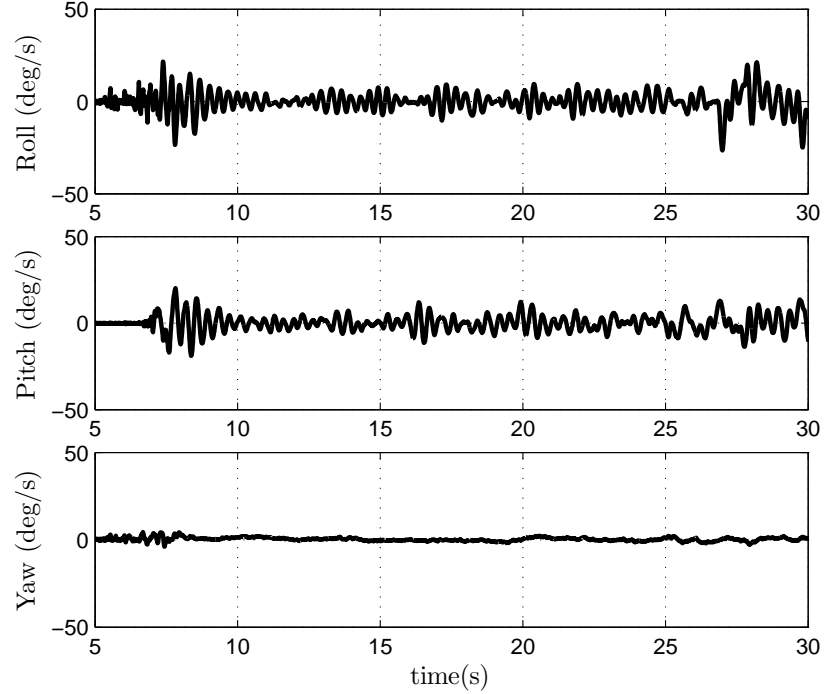
Chapter 6

Velocity-free Attitude Control with Inertial Measurements

The majority of the control schemes (for example, control scheme I and control scheme II) developed for the quadrotor are (roughly speaking) Proportional-Derivative (PD) type, where the proportional action is produced in terms of the attitude and the derivative action (generating the necessary damping) is produced in terms of the angular velocity. In practice, the orientation can be constructed or estimated using the inertial vector measurements and the angular velocity. However, gyroscopes are expensive and prone to failure especially in sophisticated aerospace applications (*e.g.,* satellites, spacecraft).

In this chapter, an inertial measurement based controller without angular velocity is implemented. Instead of using the angular velocity (either directly or indirectly), as proposed in [44], a passive auxiliary system is designed to approach the actual angular velocity. As it will be shown later, some practical issues in our implementation are discussed. Finally, a set of simulation results are presented.

6.1 Control Design

Let us define the following dynamic of auxiliary system:

$$\dot{\bar{Q}} = \frac{1}{2}\bar{Q} \odot \begin{bmatrix} 0 \\ \beta \end{bmatrix} \tag{6.1}$$

where, $\bar{Q}$ is the auxiliary attitude with $\bar{Q}(0) \in \mathbb{Q}$, and the input of the auxiliary system $\beta \in \mathbb{R}^3$ will be defined later.

Let us define the vector $\bar{b}_i, i = 1, 2, \ldots, n$, as $\bar{b}_i = R(\bar{Q})^\top r_i$, corresponding to the vector r_i in the frame attached to the auxiliary system (6.1). Let $\tilde{R} = R\bar{R}^\top$ be the discrepancy between the orientation of the rigid body and the orientation of the auxiliary system (6.1), which corresponds to the unit quaternion as $\tilde{Q} = Q \odot \bar{Q}^{-1}$. Using the fact $Q = \tilde{Q} \odot \bar{Q}$, the

dynamics of $\tilde{Q}$ are governed by

$$\dot{\tilde{Q}} = \frac{1}{2}\tilde{Q} \odot Q_{\tilde{\omega}} = \begin{bmatrix} -\frac{1}{2}\tilde{q}^\top\tilde{\omega} \\ \frac{1}{2}(\tilde{\eta}I_3 + S(\tilde{q}))\tilde{\omega} \end{bmatrix} \tag{6.2}$$

where, $\bar{Q} \odot Q_\omega \odot \bar{Q}^{-1} = Q_{\bar{\omega}}$ and $\bar{Q} \odot Q_\beta \odot \bar{Q}^{-1} = Q_{\bar{\beta}}$, where $\bar{\beta} = \bar{R}\beta$, $\bar{\omega} = \bar{R}\omega$ and $\tilde{\omega} = \bar{R}\omega - \bar{R}\beta$.

Before stating our main results, let us define the following variables:

$$z_\rho := \sum_{i=1}^n \rho_i(R_d^\top r_i) \times b_i \qquad z_\gamma := \sum_{i=1}^n \gamma_i \bar{b}_i \times b_i \tag{6.3}$$

where ρ_i and γ_i for $i = 1, 2, \cdots, n$ are positive gain parameters. Let us state the following Lemma:

Lemma 2. [44] Assume that at least two vectors, among the n inertial vectors, are not collinear. Then the following statements hold:

1) The matrix

$$W_\gamma = -\sum_{i=1}^n \gamma_i S(r_i)^2 \tag{6.4}$$

   is positive definite.

2) The following equality holds:

$$z_\gamma = -2\bar{R}^\top(\tilde{\eta}I_3 - S(\tilde{q}))W_\gamma\tilde{q} \tag{6.5}$$

3) Equation $z_\gamma = 0$ is equivalent to

$$(\tilde{\eta} = 0, \tilde{q} = v_\gamma) \quad \text{or} \quad (\tilde{\eta} = \pm 1, \tilde{q} = 0)$$

   where, v_γ are the unit eigenvectors of matrix W_γ.

Proof. The proof of Lemma 2 is similar to the proof of Lemma 2 and omitted here. $\qquad \square$

The inertial vector measurements based velocity-free controller can be generated straight-forwardly from [44] as

$$\tau = z_\rho + z_\gamma \tag{6.6}$$

where, z_ρ, and z_γ are defined in (6.3). The input of the auxiliary system (6.1) is given by

$$\beta = -z_\gamma \tag{6.7}$$

Under the proposed control law (6.6), the closed-loop dynamics of the system (2.22) and (2.23) are given by

$$\begin{aligned} \dot{q}_{\bar{e}} &= \frac{1}{2}(\eta_{\bar{e}}I_3 + S(q_{\bar{e}}))R_d\omega \\ \dot{\tilde{q}} &= \frac{1}{2}(\tilde{\eta}I_3 + S(\tilde{q}))\left(R^\top\tilde{R}\omega - 2(\tilde{\eta}I_3 - S(\tilde{q}))W_\gamma\tilde{q}\right) \\ I_f\dot{\omega} &= -S(\omega)I_f\omega - 2R_d^\top(\eta_{\bar{e}}I_3 - S(q_{\bar{e}}))W_\rho q_{\bar{e}} - 2R^\top\tilde{R}(\tilde{\eta}I_3 - S(\tilde{q}))W_\gamma\tilde{q} \end{aligned} \tag{6.8}$$

where, using the facts $z_\rho = -2R_d^\top(\eta_{\bar{e}}I_3 - S(q_{\bar{e}}))W_\rho q_{\bar{e}}$ and $z_\gamma = R^\top\tilde{R}(\tilde{\eta}I_3 - S\tilde{q})W_\gamma\tilde{q}$. Note that the desired attitude R_d is constant, and the closed-loop dynamics (6.8) are autonomous.

Let $\chi := (q_{\bar{e}}, \tilde{q}, \omega) \in D \times D \times \mathbb{R}^3$ be the state vector, with $D := \{x \in \mathbb{R}^3 \mid \|x\| \leq 1\}$. Now, one can state the following theorem.

Theorem 6.1. [44] Consider system (2.22) and (2.23) under the control law (6.6). Let (6.7) be the input of the auxiliary sytem (6.1). Assume that n vector measurements b_i, corresponding to the inertial vectors r_i, $i = 1, 2, \ldots, n \geq 2$ are available, and at least two vectors, among the n inertial vectors are not collinear. Then

1) The equilibria of the closed-loop error dynamics (6.8) are given by $\Omega_1 = (0, 0, 0)$, $\Omega_2 = (v_\rho, 0, 0)$, $\Omega_3 = (0, v_\gamma, 0)$ and $\Omega_4 = (v_\rho, v_\gamma, 0)$, where, v_ρ and v_γ, respectively, are the unit eigenvectors of W_ρ and W_γ.

2) The equilibrium point Ω_1 is locally asymptotically stable with the domain of attraction containing the following domains:

$$\Phi_1 = \{\chi \in D \times D \times \mathbb{R}^3 | \chi^\top P\chi \leq c\} \tag{6.9}$$

   where, $P = \text{diag}(2W_\rho, 2W_\gamma, \frac{1}{2}I_f)$, $c < 2\min\{\lambda(W_\rho), \lambda(W_\gamma)\}$ and $\lambda(x)$ is the eigenvalues of matrix (x).

3) The equilibria Ω_2, Ω_3 and Ω_4 are unstable and equilibrium point Ω_1 is almost globally asymptotically stable.

Proof. Consider the following Lyapunov function candidate

$$V = 2q_{\bar{e}}W_\rho q_{\bar{e}} + 2\tilde{q}W_\gamma\tilde{q} + \frac{1}{2}\omega^\top I_f\omega \tag{6.10}$$

Define $e_i = R_d^\top r_i - b_i$ and $\tilde{b}_i = \bar{b}_i - b_i$. Similarly, one shows that

$$\sum_{i=1}^n \rho_i e_i^\top e_i = 4q_{\bar{e}}W_\rho q_{\bar{e}}, \quad \sum_{i=1}^n \gamma_i \tilde{b}_i^\top \tilde{b}_i = 4\tilde{q}W_\gamma\tilde{q}$$

One can also show that the dynamics of $\tilde{b}_i$ and e_i as

$$\begin{aligned}
\dot{\tilde{b}}_i &= S(\bar{b}_i)(\beta - \omega) + S(\tilde{b}_i)\omega \\
\dot{e}_i &= -S(b_i)\omega
\end{aligned} \tag{6.11}$$

Consequently, the Lyapunov function candidate (6.10) can be rewritten as

$$V = \frac{1}{2}\sum_{i=1}^n \rho_i e_i^\top e_i + \frac{1}{2}\sum_{i=1}^n \gamma_i \tilde{b}_i^\top \tilde{b}_i + \frac{1}{2}\omega^\top I_f\omega \tag{6.12}$$

Then, the time derivative of V, along the trajectory of (2.23) and (6.11), is given by

$$
\begin{aligned}
\dot{V} &= \sum_{i=1}^{n} \rho_i e_i^\top \dot{e}_i + \sum_{i=1}^{n} \gamma_i \tilde{b}_i^\top \dot{\tilde{b}}_i + \omega^\top I_f \dot{\omega} \\
&= -\sum_{i=1}^{n} \rho_i e_i^\top S(b_i)\omega + \sum_{i=1}^{n} \gamma_i \tilde{b}_i^\top \left(S(\bar{b}_i)\beta - S(b_i)\omega \right) + \omega^\top I_f \dot{\omega} \\
&= -\sum_{i=1}^{n} \rho_i e_i^\top S(b_i)\omega + \sum_{i=1}^{n} \gamma_i \tilde{b}_i^\top \left(S(\bar{b}_i)(\beta - \omega) + S(\tilde{b}_i)\omega \right) + \omega^\top I_f \dot{\omega} \\
&= -\sum_{i=1}^{n} \rho_i e_i^\top S(b_i)\omega - \sum_{i=1}^{n} \gamma_i b_i^\top S(\bar{b}_i)(\beta - \omega) + \omega^\top I_f \dot{\omega} \\
&= -\omega^\top \sum_{i=1}^{n} \rho_i S(R_d^\top r_i)b_i - (\omega - \beta)^\top \sum_{i=1}^{n} \gamma_i S(\bar{b}_i)b_i + \omega^\top \left(\tau - S(\omega)I_f\omega \right) \\
&= -\omega^\top z_\rho - (\omega - \beta)^\top z_\gamma + \omega^\top (z_\rho + z_\gamma) \\
&= -z_\gamma^\top z_\gamma
\end{aligned}
\tag{6.13}
$$

Since the closed-loop system (6.8) is autonomous, the LaSalle's invariance theorem is applied in the following statements. From (6.13), setting $\dot{V} \equiv 0$, one obtains $z_\gamma \equiv 0$, which implies that $\tilde{Q} \equiv (\pm 1, 0)$ or $\tilde{Q} \equiv (0, v_\gamma)$ from Lemma 2. Consequently, one can show that $\omega \equiv \beta$ in view of the first equation of (6.8). On the other hand, since $z_\gamma \equiv 0$, it follows from the definition of β that $\beta \equiv 0$, and consequently $\omega \equiv 0$ from the second equation of (6.8). Then, one concludes that $\tau \equiv 0$. Using the fact that $z_\gamma \equiv 0$, from (6.6), one obtains that $z_\rho \equiv 0$. Invoking Lemma 1, one has $Q_{\bar{e}} \equiv (\pm 1, 0)$ or $Q_{\bar{e}} \equiv (0, v_\rho)$. It is clear that the largest invariant for the closed-loop system (6.8), characterized by $\dot{V} = 0$ is given by $\Omega = \bigcup_{i=1}^{4} \Omega_i$.

Since V is non-increasing, one has $V(\chi(t)) \leq V(\chi(0))$, for all $t \geq 0$, which implies that Φ_1 is a positively invariant sublevel set. From (6.10), it follows that $V(\chi) \geq 2\lambda_{min}(W_\gamma)\|\tilde{q}\|^2$ and $V(\chi) \geq 2\lambda_{min}(W_\rho)\|q_{\bar{e}}\|^2$. It is clear that Ω_2, Ω_3 and Ω_4 do not belong to Φ_1, since $c < \min_{\|\tilde{q}\|=1, \|q_{\bar{e}}\|=1} V(\chi) = 2\min\{\lambda_{min}(W_\rho), \lambda_{min}(W_\gamma)\}$. Consequently, Ω_1 is the only largest invariant set in Φ_1. This ends the second claim of the theorem.

Now, we need to show that the equilibria Ω_2, Ω_3 and Ω_4 are unstable using Chetaev arguments [69]. Introducing the changes of variables $Q_x = (\eta_x, q_x) = (0, -v_\rho) \odot Q_{\bar{e}}$ and $Q_y(\eta_y, q_y) = (0, -v_\gamma) \odot \tilde{Q}$, one can rewritten the $Q_{\bar{e}}$ and $\tilde{Q}$ as

$$
\begin{bmatrix} \eta_{\bar{e}} \\ q_{\bar{e}} \end{bmatrix} = \begin{bmatrix} 0 \\ v_\rho \end{bmatrix} \odot \begin{bmatrix} \eta_x \\ q_x \end{bmatrix} = \begin{bmatrix} -q_x^\top v_\rho \\ \eta_x v_\rho + S(v_\rho)q_x \end{bmatrix}
\tag{6.14}
$$

$$
\begin{bmatrix} \tilde{\eta} \\ \tilde{q} \end{bmatrix} = \begin{bmatrix} 0 \\ v_\gamma \end{bmatrix} \odot \begin{bmatrix} \eta_y \\ q_y \end{bmatrix} = \begin{bmatrix} -q_y^\top v_\gamma \\ \eta_y v_\gamma + S(v_\gamma)q_y \end{bmatrix}
\tag{6.15}
$$

It is clear that the equilibria Ω_2, Ω_3 and Ω_4 are, respectively, equivalent to $\Lambda_2 = (q_x = 0, \tilde{q} = 0, \omega = 0)$, $\Lambda_3 = (q_{\bar{e}} = 0, q_y = 0, \omega = 0)$ and $\Lambda_4 = (q_x = 0, q_y = 0, \omega = 0)$. The linearization of the closed-loop system (6.8) about the equilibria Λ_2, Λ_3 and Λ_4, respectively, leads to

the state matrices A_2, A_3 and A_4

$$A_2 = \begin{bmatrix} N_2 & 0 & \frac{1}{2}N_1 \\ 0 & 0 & \frac{1}{2}\sigma I_3 \\ 2I_f^{-1}N_1N_2 & -2\sigma I_f^{-1}W_\rho & 0 \end{bmatrix} \tag{6.16}$$

$$A_3 = \begin{bmatrix} -W_\gamma & 0 & -\frac{1}{2}\sigma M_1 \\ 0 & 0 & \frac{1}{2}I_3 \\ -2\sigma I_f^{-1}M_1W_\gamma & 2I_f^{-1}M_2 & 0 \end{bmatrix} \tag{6.17}$$

$$A_4 = \begin{bmatrix} N_2 & 0 & \frac{1}{2}N_1M_1 \\ 0 & 0 & \frac{1}{2}I_3 \\ 2I_f^{-1}M_1N_1N_2 & 2I_f^{-1}M_2 & 0 \end{bmatrix} \tag{6.18}$$

where, $N_1 = 2v_\gamma v_\gamma^\top - I_3$, $M_1 = 2v_\rho v_\rho^\top - I_3$, $N_2 = \lambda_\gamma I_3 + S(v_\gamma)W_\gamma S(v_\gamma)$, $M_2 = \lambda_\rho I_3 + S(v_\rho)W_\rho S(v_\rho)$ and $\sigma = \pm 1$. Note that N_2 is a symmetric matrix with eigenvalues λ_γ, $\bar{\lambda}_1 := \lambda_\gamma - \lambda_1$ and $\bar{\lambda}_2 = \lambda_\gamma - \lambda_2$, where $\lambda_\gamma, \lambda_1$ and λ_2 are the eigenvalues of W_γ. The matrix N_1 is clearly nonsingular and satisfies $N_1^2 = I_3$.

To show that equilibria Λ_2 is unstable, we consider the following Chetaev function

$$V_2(q_x, \tilde{q}, \omega) = 4q_x^\top N_2 q_x + 4\tilde{q}^\top W_\rho \tilde{q} - \omega^\top I_f \omega \tag{6.19}$$

where, $V_2(0,0,0) = 0$. Define the set $B_r = \{x := (q_x, \tilde{q}, \omega^\top)^\top \in D \times D \times \mathbb{R}^3 | \, \|x(t)\| < r\}$, where $r > 0$. Let us define U_r a subset of B_r that is, $U_r = \{x \in B_r | V_2(x) > 0\}$. Note that U_r is a non-empty set contained in B_r, since $V_2(\epsilon v_\gamma, 0, 0) = \epsilon^2 \lambda_\gamma > 0$ for all $\epsilon^2 < r$. The time derivative of V_2, is given by

$$\begin{aligned} \dot{V}_2 &= 8q_x^\top N_2 \dot{q}_x + 8\tilde{q}^\top W_\rho \dot{\tilde{q}} - 2\omega^\top I_f \dot{\omega} \\ &= 8q_x^\top N_2(N_2 q_x + \frac{1}{2}N_1\omega) + 4\sigma\tilde{q}^\top W_\rho\omega - 2\omega^\top(2N_1N_2q_x - 2\sigma W_\rho) \\ &= 8q_x^\top N_2 N_2 q_x \end{aligned}$$

where, $\dot{V}_2$ is positive semi-definite everywhere in U_r for all $r > 0$. Therefore, for any initial conditions $x(0) \in U_r$, the state $x(t)$ must leave U_r since $V_2(x)$ is bounded on U_r and V_2 is non-decreasing in U_r. Since $V_2(x) > V_2(0)$, $x(t)$ must leave U_r through the circle $\|x\| = r$ and not through the edges $V_2(x) = 0$. Hence the equilibrium point Ω_2 is unstable. Similarly, one can choose the following Chetave functions for Λ_3 and Λ_4, respectively, as

$$V_3(x, q_e, \omega) = 4q_e^\top N_2 q_e + 4x^\top N_2 x - \omega^\top I_f \omega \tag{6.20}$$

$$V_4(x, y, \omega) = 4y^\top N_2 y + 4x^\top N_2 x - \omega^\top I_f \omega \tag{6.21}$$

The same arguments can be used to show that Ω_3 and Ω_4 are also unstable, and omitted here.

To show the equilibrium point Ω_1 is almost globally asymptotically stable, we need to show that the stable manifolds associated to the unstable equilibria have Lebesgue measure zero.

We need to show that the eigenvalues of A_2, A_3 and A_4 are not all with zero real-part [71]. In practice, it is easy to choose the control gains γ_i such that the eigenvalues of W_γ are all equal (see Section 6.2). The trace of A_2 is given by $\mathrm{Tr}(A_2) = \mathrm{Tr}(N_2) = 4\lambda_\gamma - \mathrm{Tr}(W_\gamma) = \lambda_\gamma > 0$. Hence, A_2 can not have all its eigenvalues with zero real-part. Similar arguments can be used to show that A_4 does not have all its eigenvalues with zero real-parts, and hence omitted. For A_3, it is clear that the eigenvalues of A_3 are not all on the imaginary axis, since $\mathrm{Tr}(A_3) = -\mathrm{Tr}(W_\gamma) \neq 0$ as W_γ is symmetric positive definite. Finally, one concludes that the equilibrium Ω_1 of the closed-loop system (6.8) is almost globally asymptotically stable. This completes the proof. $\qquad\square$

6.2 Implementation using Inertial Vector Measurements

6.2.1 Standard Implementation

Considering the same decoupled inertial vectors $u_\mathcal{I}$, $v_\mathcal{I}$ and $\mu_\mathcal{I}$ and their measurements $u_\mathcal{B}$, $v_\mathcal{B}$ and $\mu_\mathcal{B}$ defined in Chapter 5, one has the following standard velocity-free controller and auxiliary system input as:

$$
\begin{aligned}
\tau &= z_\rho + z_\gamma \\
\beta &= -z_\gamma \\
z_\rho &:= \rho_1(R_d^\top u_\mathcal{I}) \times u_\mathcal{B} + \rho_2(R_d^\top v_\mathcal{I}) \times v_\mathcal{B} + \rho_3(R_d^\top \mu_\mathcal{I}) \times \mu_\mathcal{B} \\
z_\gamma &:= \gamma_1(\bar{R}^\top u_\mathcal{I}) \times u_\mathcal{B} + \gamma_2(\bar{R}^\top v_\mathcal{I}) \times v_\mathcal{B} + \gamma_3(\bar{R}^\top \mu_\mathcal{I}) \times \mu_\mathcal{B}
\end{aligned}
$$

The control torque and the auxiliary system input can be simplified by choosing $\rho_1 = \rho_2 = \rho_3 = \rho$, $\gamma_1 = \gamma_2 = \gamma_3 = \gamma$ as:

$$
\begin{aligned}
\tau &= -4\rho\eta_{\bar{e}}q_{\bar{e}} - 4\gamma\tilde{\eta}\tilde{q} \\
\beta &= 4\gamma\tilde{\eta}\tilde{q}
\end{aligned}
\tag{6.22}
$$

Note that almost-global stability for the equilibrium point Ω_1 is still guaranteed with the control (6.22). However, some issues in the implementation can be pointed by observing the performance of the linearized closed-loop dynamics. Let us consider the first-order approximation of the closed-loop system (6.8) with the control torque and auxiliary system input given by (6.22) around the equilibrium point Ω_1,

$$
\begin{aligned}
\dot{q}_{\bar{e}} &= \frac{1}{2}\omega \\
\dot{\omega} &= -4I_f^{-1}\rho q_{\bar{e}} - 4\gamma I_f^{-1}\tilde{q} \\
\dot{\tilde{q}} &= \frac{1}{2}\omega - 2\gamma\tilde{q}
\end{aligned}
\tag{6.23}
$$

where, we use the facts $\tilde{R} \approx I_3 + 2S(\tilde{q})$ and $R_{\bar{e}} \approx I_3 + 2S(q_{\bar{e}})$. Next we will show the slow response by checking the eigenvalues of the state matrix of the linearized system. From the linear dynamics (6.23), it is easy to check that the linear dynamics of the roll, pitch and yaw are locally decoupled. Define a new state $\xi = (\xi_\phi, \xi_\theta, \xi_\psi)$, where $\xi_\phi = (q_{\bar{e},1}, \omega_1, \tilde{q}_1)$,

$\xi_\theta = (q_{\bar{e},2}, \omega_3, \tilde{q}_2)$ and $\xi_\psi = (q_{\bar{e},3}, \omega_3, \tilde{q}_3)$, then the state matrix of the dynamics (6.23) is given by

$$A_s = \begin{bmatrix} A_\phi & 0_3 & 0_3 \\ 0_3 & A_\theta & 0_3 \\ 0_3 & 0_3 & A_\psi \end{bmatrix} \tag{6.24}$$

with

$$A_\phi = \begin{bmatrix} 0 & \frac{1}{2} & 0 \\ -4\rho I_\phi^{-1} & 0 & -4\gamma I_\phi^{-1} \\ 0 & \frac{1}{2} & -2\gamma \end{bmatrix} A_\theta = \begin{bmatrix} 0 & \frac{1}{2} & 0 \\ -4\rho I_\theta^{-1} & 0 & -4\gamma I_\theta^{-1} \\ 0 & \frac{1}{2} & -2\gamma \end{bmatrix} A_\psi = \begin{bmatrix} 0 & \frac{1}{2} & 0 \\ -4\rho I_\psi^{-1} & 0 & -4\gamma I_\psi^{-1} \\ 0 & \frac{1}{2} & -2\gamma \end{bmatrix}$$

The eigenvalues of matrix A_s can be obtained by solving the following polynomial equation for λ:

$$\det(\lambda I_9 - A_s) = \det(\lambda I_3 - A_\phi)\det(\lambda I_3 - A_\theta)\det(\lambda I_3 - A_\psi) = 0 \tag{6.25}$$

There are only two parameters ρ and γ that may affect the eigenvalues of the state matrix A_s. Let us firstly check the eigenvalues of matrix A_ϕ

$$\begin{aligned} \det(\lambda I_3 - A_\phi) &= \det\left(\begin{bmatrix} \lambda & -\frac{1}{2} & 0 \\ 4\rho I_\phi^{-1} & \lambda & 4\gamma I_\phi^{-1} \\ 0 & -\frac{1}{2} & \lambda + 2\gamma \end{bmatrix}\right) \\ &= \lambda^3 + 2\rho I_\phi^{-1}\lambda + 2\gamma(\lambda^2 + \lambda I_\phi^{-1} + 2\rho I_\phi^{-1}) \\ &= 0 \end{aligned} \tag{6.26}$$

It is not easy to get the exact symbolic eigenvalues. However, one can get the numerical solutions using MATLAB. For a fixed positive value of ρ, for example $\rho = 1.5$ given in Chapter 5, the eigenvalues of the state matrix A_ϕ are plotted in Fig. 6.1 for all values of γ (where, $I_\phi = 0.0159$ given in Section 3.2). As it shown, all the eigenvalues have the negative real part for $\gamma > 0$. The eigenvalues of the state matrix A_ϕ will be very close to zero if the value of γ is not taken sufficiently large, since $\text{Tr}(A_\phi) = \lambda_1 + \lambda_2 + \lambda_3 = -2\gamma$. For discussion purposes, let us assume that $2\gamma \approx \infty$. Then, it is straightforward to verify that the three eigenvalues are given by

$$\begin{cases} \lambda_1 = -\frac{1}{2}I_\phi^{-1}\left(1 - \sqrt{1 - 8\rho I_\phi}\right) \\ \lambda_2 = -\frac{1}{2}I_\phi^{-1}\left(1 + \sqrt{1 - 8\rho I_\phi}\right) \\ \lambda_3 = -2\gamma + I_\phi^{-1} \end{cases} \tag{6.27}$$

It is known that the largest eigenvalue (*i.e.,* the smallest in absolute value) of the state matrix is important for the convergence rate. Then, one has the limit of the maximum eigenvalues of the state matrix A_ϕ with respect to γ as

$$\lim_{\gamma \to \infty} \lambda_{\max}(A_\phi) = -\frac{1}{2}I_\phi^{-1}\left(1 - \sqrt{1 - 8\rho I_\phi}\right) \tag{6.28}$$

It is clear that $\lim_{\gamma \to \infty} \lambda_{\max}(A_\phi)$ will be small if ρ is not large enough, since $I_\phi \ll 1$. The eigenvalues of A_θ and A_ψ are plotted, respectively, in Fig. 6.2 and Fig. 6.3 for all values of γ. The same arguments can be used for the eigenvalues of the state matrices A_θ and A_ψ. Finally, one can conclude that the maximum eigenvalues of the state matrix A_s will be very close to imaginary axis if ρ and γ are not chosen sufficiently large. This leads to slow time response of the closed-loop dynamics (6.23).
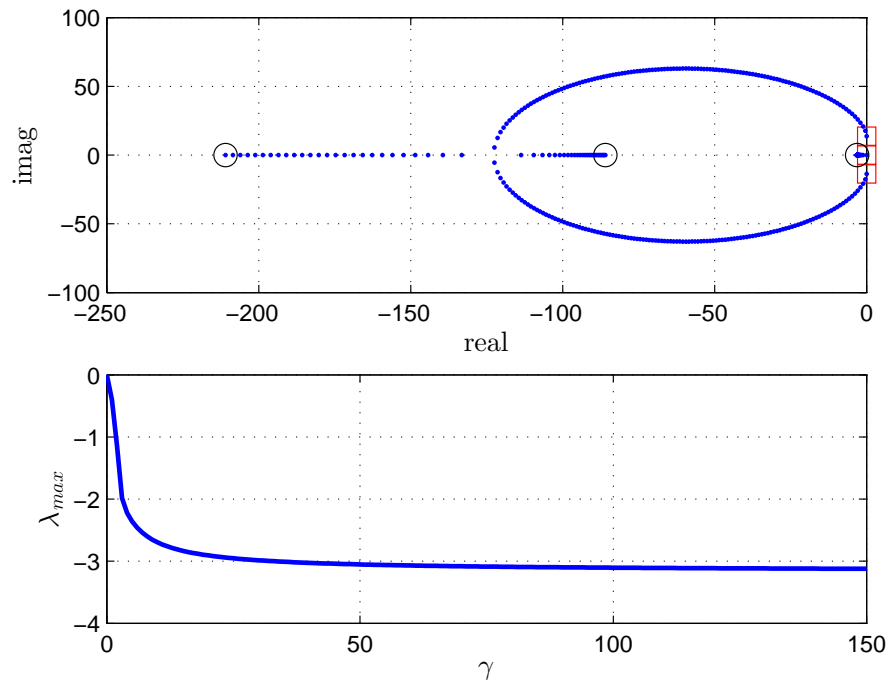
Figure 6.1: Eigenvalues of the roll dynamics varying with γ
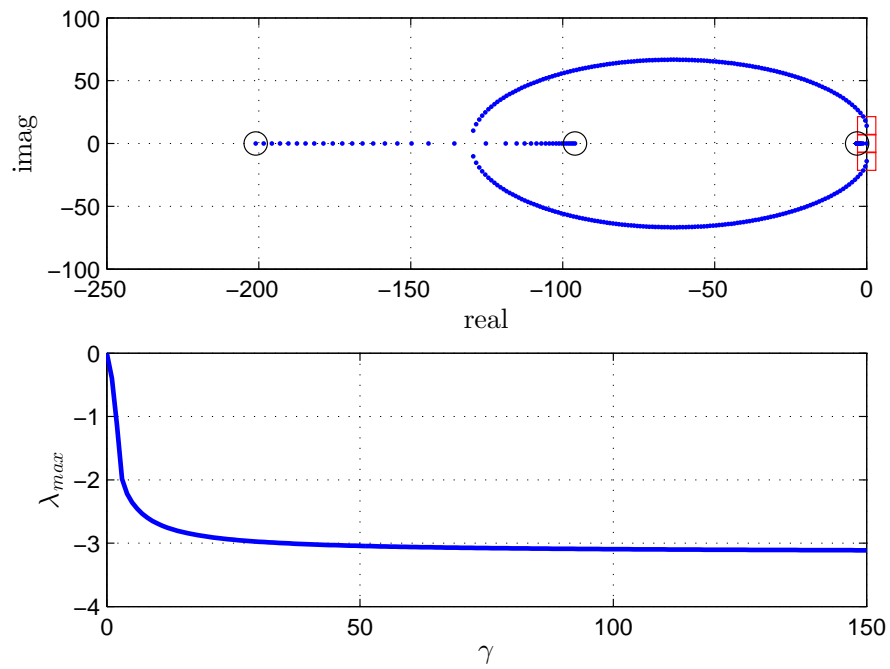
Figure 6.2: Eigenvalues of the pitch dynamics varying with γ
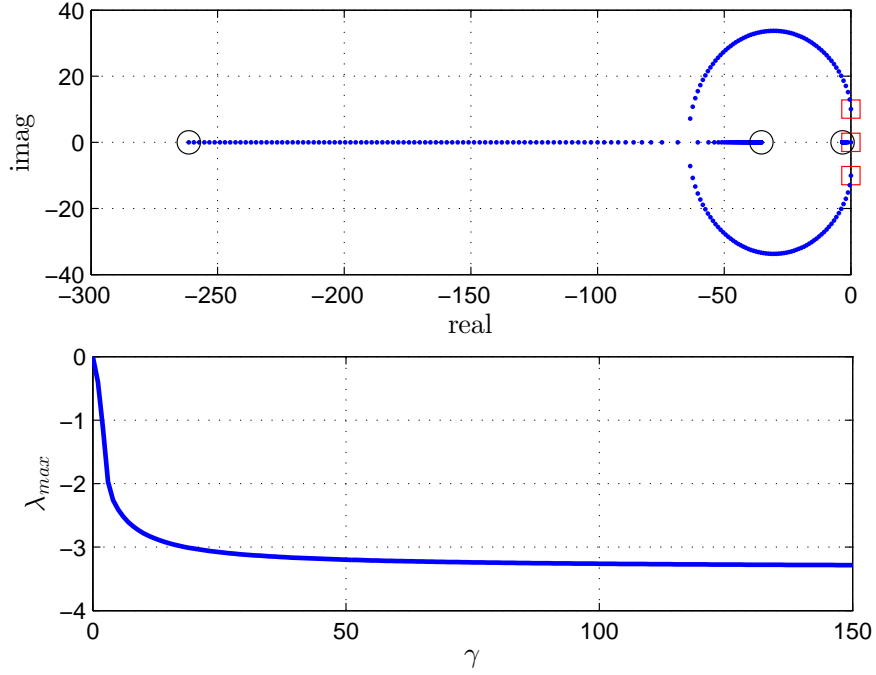
Figure 6.3: Eigenvalues of the yaw dynamics varying with γ

6.2.2 Improved Implementation

An improved approach has been proposed as follows

$$
\begin{aligned}
\tau &= -4\rho\eta_{\bar{e}}q_{\bar{e}} - 4\gamma\tilde{\eta}\tilde{q} \\
\beta &= 4\gamma K_\beta\tilde{\eta}\tilde{q}
\end{aligned}
\tag{6.29}
$$

where, K_β is a diagonal positive definite matrix. Note that it is easy to check that the proposed approach leads to the same results as in Theorem 6.1. Again, let us consider the first-order approximation of the closed-loop dynamics around the equilibrium point Ω_1 as

$$
\begin{aligned}
\dot{q}_{\bar{e}} &= \frac{1}{2}\omega \\
\dot{\omega} &= -4\rho I_f^{-1}q_{\bar{e}} - 4\gamma I_f^{-1}\tilde{q} \\
\dot{\tilde{q}} &= \frac{1}{2}\omega - 2\gamma K\tilde{q}
\end{aligned}
\tag{6.30}
$$

The state matrix of the dynamics (6.30) is given by

$$
\bar{A}_s = \begin{bmatrix} \bar{A}_\phi & 0_3 & 0_3 \\ 0_3 & \bar{A}_\theta & 0_3 \\ 0_3 & 0_3 & \bar{A}_\psi \end{bmatrix}
\tag{6.31}
$$

with

$$
\bar{A}_\phi = \begin{bmatrix} 0 & \frac{1}{2} & 0 \\ -4\rho I_\phi^{-1} & 0 & -4\gamma I_\phi^{-1} \\ 0 & \frac{1}{2} & -2\gamma K_\phi \end{bmatrix} \quad
\bar{A}_\theta = \begin{bmatrix} 0 & \frac{1}{2} & 0 \\ -4\rho I_\theta^{-1} & 0 & -4\gamma I_\theta^{-1} \\ 0 & \frac{1}{2} & -2\gamma K_\theta \end{bmatrix} \quad
\bar{A}_\psi = \begin{bmatrix} 0 & \frac{1}{2} & 0 \\ -4\rho I_\psi^{-1} & 0 & -4\gamma I_\psi^{-1} \\ 0 & \frac{1}{2} & -2\gamma K_\psi \end{bmatrix}
$$

where, $K = diag(K_\phi, K_\theta, K_\psi)$. The eigenvalues of state matrix $\bar{A}_s$ are given by the roots of the following polynomial equation:

$$\det(\lambda I_3 - \bar{A}_\phi) \det(\lambda I_3 - \bar{A}_\theta) \det(\lambda I_3 - \bar{A}_\psi) = 0 \qquad (6.32)$$

One has that the eigenvalues of state matrix $\bar{A}_s$ are the eigenvalues of the matrices $\bar{A}_\phi$, $\bar{A}_\theta$ and $\bar{A}_\psi$. The eigenvalues of $\bar{A}_\phi$ are the roots of the following polynomial equation:

$$\lambda^3 + 2\rho I_\phi^{-1}\lambda + 2\gamma(K_\phi\lambda^2 + \lambda I_\phi^{-1} + 2\rho K_\phi I_\phi^{-1}) = 0 \qquad (6.33)$$

Again, let us assume that $2\gamma \approx \infty$ for discussion purposes. Then the three eigenvalues are given by

$$\begin{cases} \lambda_1 = -\frac{1}{2}(I_\phi K_\phi)^{-1}\left(1 - \sqrt{1 - 8\rho K_\phi^2 I_\phi}\right) \\ \lambda_2 = -\frac{1}{2}(I_\phi K_\phi)^{-1}\left(1 + \sqrt{1 - 8\rho K_\phi^2 I_\phi}\right) \\ \lambda_3 = -2\gamma + (I_\phi K_\phi)^{-1} \end{cases} \qquad (6.34)$$

One can verify that $\text{Real}(\lambda_1) \geq -\sqrt{2\rho I_\phi^{-1}}$, and $\text{Real}(\lambda_1) = -\sqrt{2\rho I_\phi^{-1}}$ if and only if $K_\phi = \frac{1}{2\sqrt{2\rho I_\phi}}$. Then one has the limit of the maximum eigenvalues of the state matrix $\bar{A}_\phi$ with respect to γ as

$$\lim_{\gamma\to\infty} \lambda_{\max}(\bar{A}_\phi) = -\sqrt{2\rho I_\phi^{-1}} \qquad (6.35)$$

It is easy to check that $\lim_{\gamma\to\infty} \lambda_{\max}(\bar{A}_\phi) \leq \lim_{\gamma\to\infty} \lambda_{\max}(A_\phi)$ when ρ is chosen sufficient small (*i.e.*, $\rho < 1/(8I_\phi)$). Choosing $\rho = 1.5$ and $K_\phi = 1/(2\sqrt{2\rho I_\phi}) = 2.2893$, the eigenvalues of the state matrix $\bar{A}_\phi$ are plotted in Fig. 6.4 with respect to γ. As we can see, $\lambda_{\max}(\bar{A}_\phi) < \lambda_{\max}(A_\phi)$ for all values of γ. The same arguments can be used for the eigenvalues of $\bar{A}_\theta$ and $\bar{A}_\psi$. The eigenvalues of the matrices $\bar{A}_\phi$, $\bar{A}_\theta$ and $\bar{A}_\psi$ are presented, respectively, in Fig. 6.5 and Fig. 6.6 for all values of γ. An advantage of the improved approach with respect to the standard approach, is that there exists a set of "nonhigh" gains ρ leading to a fast time response.

On the other hand, the slow time response of the closed-loop system is not the sole issue. The auxiliary system leads to the difficulty of finding nonhigh gain γ leading to small noise in the feedback. The closed-loop dynamics can be rewritten as a second-order dynamics and a passive dynamics

$$I_f\ddot{q}_{\bar{e}} + 2\gamma\tilde{q} + 2\rho q_{\bar{e}} = 0 \qquad (6.36)$$
$$\dot{\tilde{q}} = -2\gamma K\tilde{q} + \dot{q}_{\bar{e}} \qquad (6.37)$$

From the dynamics (6.37), one can verify that the rate of convergence of $2\gamma\tilde{q} \to K^{-1}\dot{q}_e$ can be guaranteed when γ is chosen sufficiently large. Moreover, choosing $K = \Gamma_2^{-1}$ defined in Chapter 5, the dynamics (6.36) can be approximated by

$$I_f\ddot{q}_{\bar{e}} + \Gamma_2\dot{q}_{\bar{e}} + 2\rho q_{\bar{e}} = 0 \qquad (6.38)$$

which is similar to the dynamics (5.51). However, the large gain γ may excessively amplify the measurement noise in the feedback (6.29). This leads to the difficulty of finding a "nonhigh" gain γ providing the system with an acceptable acceptably fast time response.
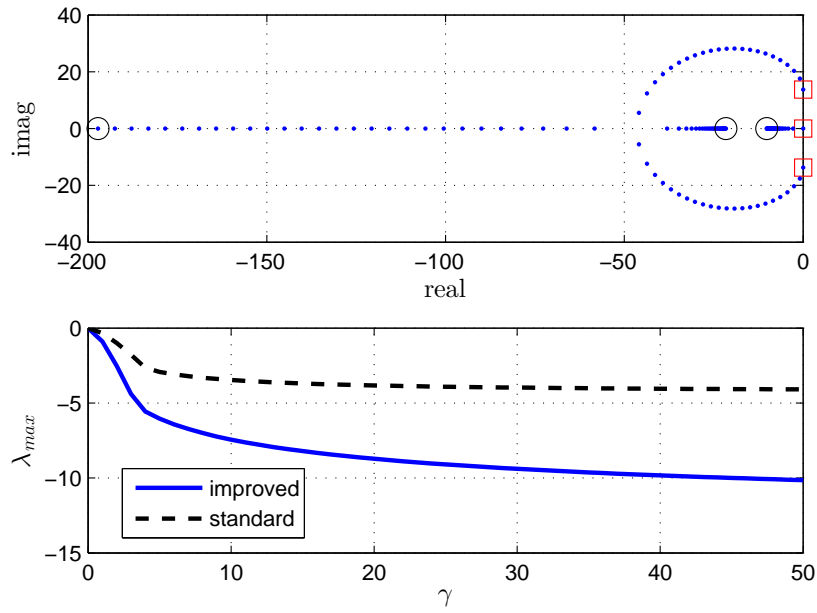
Figure 6.4: Eigenvalues of the roll dynamics varying with gamma
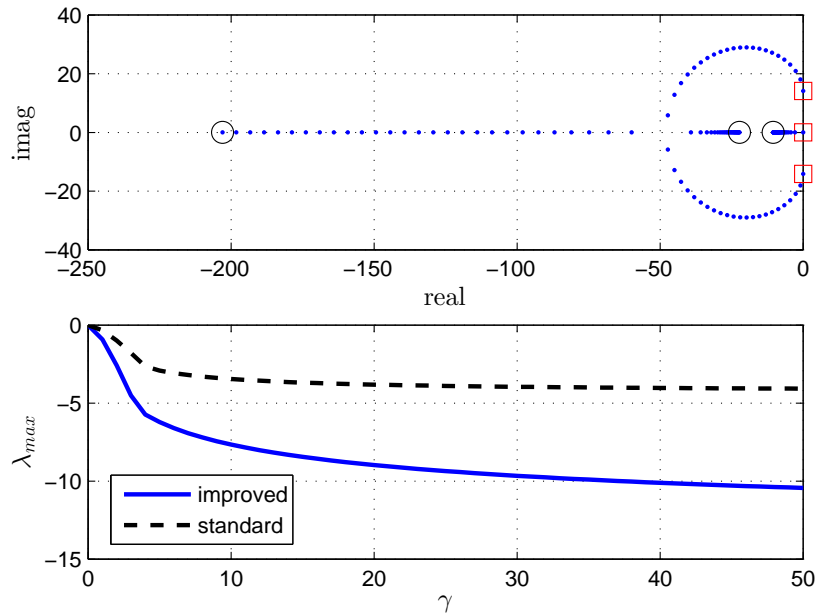

Figure 6.5: Eigenvalues of the pitch dynamics varying with gamma

6.3   Simulation Results

As proposed in reference [44], an overview of the inertial measurements based velocity-free control scheme is shown in Fig. 6.7. As we can see, the outputs of the dynamics model are
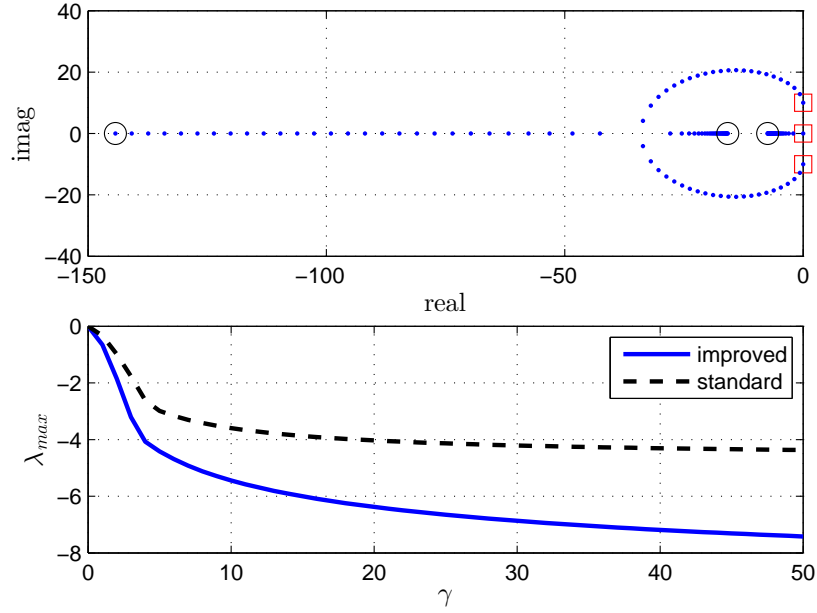
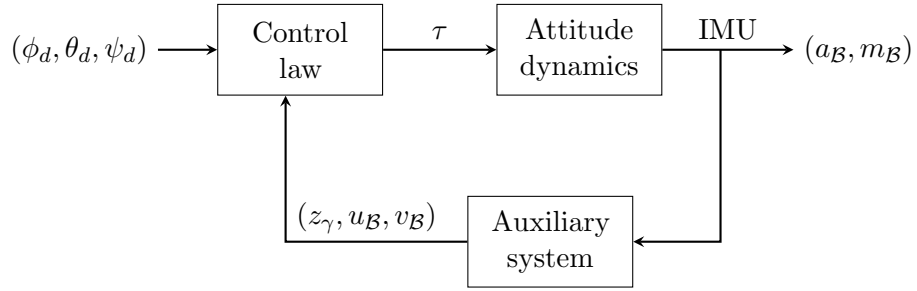Figure 6.6: Eigenvalues of the yaw dynamics varying with gamma

Figure 6.7: Control scheme III

only accelerometer and magnetometer measurements. However, with the help of auxiliary system, the vector z_γ is designed to approach the angular velocity.

Simulation 1	Simulation 2
Standard controller (6.22)	Improved controller (6.29)
$\rho_1 = \rho_2 = \rho_3 = \rho = 1.5$	
$\gamma_1 = \gamma_2 = \gamma_3 = \gamma = 132$	$\gamma_1 = \gamma_2 = \gamma_3 = \gamma = 25$
	$K^{-1} = \mathrm{diag}([0.44, 0.42, 0.60])$

Table 6.1: Control gains for simulation

Two sets of simulations have been presented in this section showing the performance of quadrotor system with the velocity-free controllers (6.22) and (6.29). The inertia matrix has been taken the same as in Chapter 4, and the initial conditions are taken as $\phi(0) = -22\,\mathrm{deg}$, $\theta(0) = 18\,\mathrm{deg}$, $\psi(0) = -10\,\mathrm{deg}$ and $\omega = (0, 0, 0)^\top$. For the attitude stabilization, the desired

attitude is given by $\phi_d = 0 \deg$, $\theta_d = 0 \deg$ and $\psi_d = 0 \deg$. The control parameters involved in the controllers (6.22) and (6.29) are chosen as shown in Table 6.1

The simulation results presented in Fig. 6.8-6.11 show important performance differences between the standard approach and the improved approach. In particular, the standard approach shows a slow convergence in the roll, pitch and yaw dynamics with large value of γ. In contrast, one can see, for the improved approach, a very fast convergence of the Euler angles despite the use of relative small value of γ. This can be explained by the fact that, for the improved approach, the auxiliary velocity is much closer to the actual angular velocity compared to the standard approach (see Fig. 6.9 and 6.11).
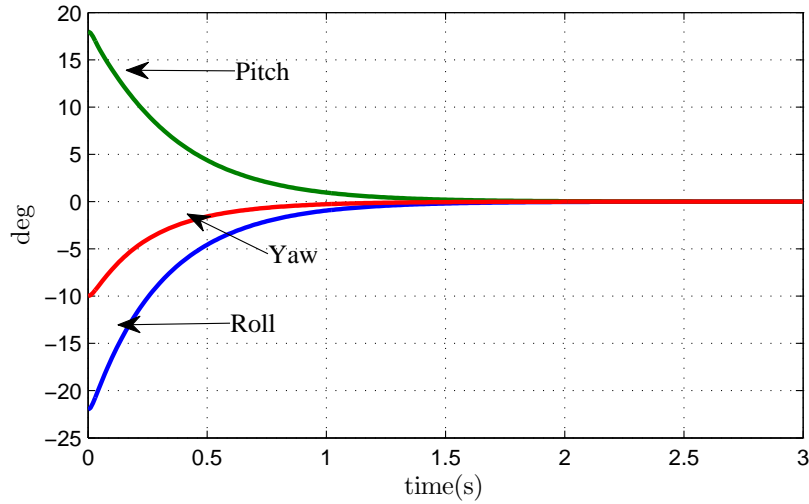
(a) Attitude in Euler angles
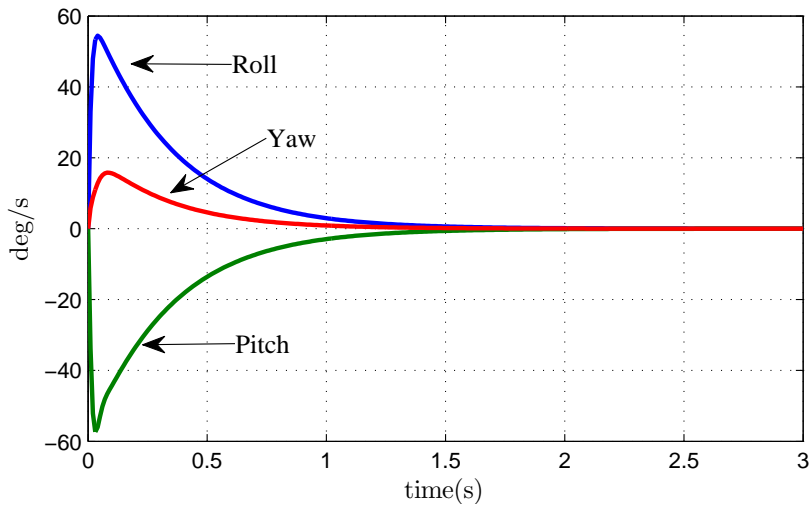
(b) Angular velocity

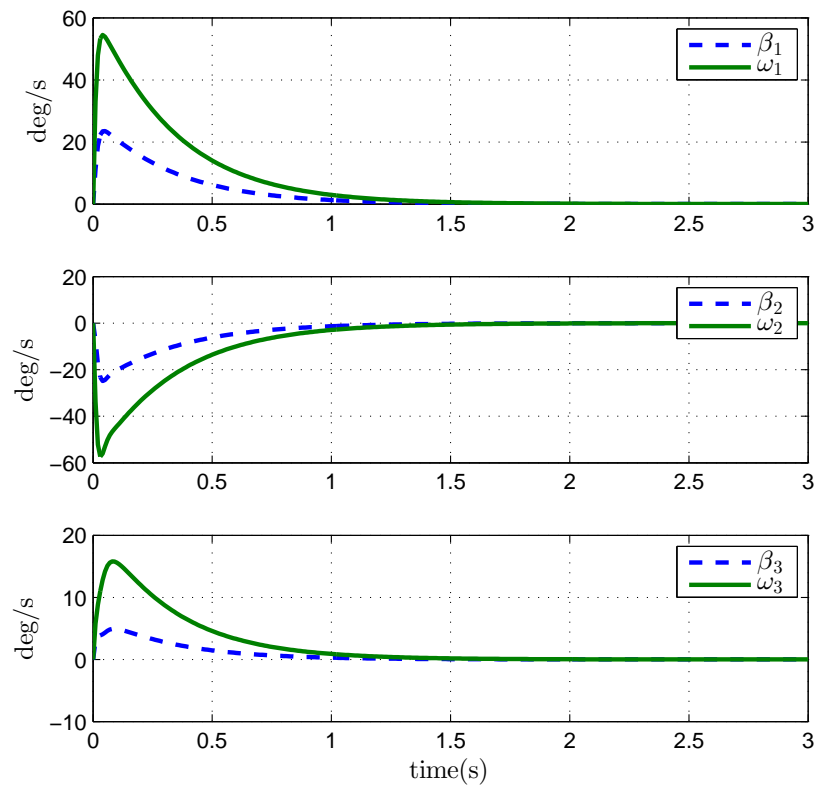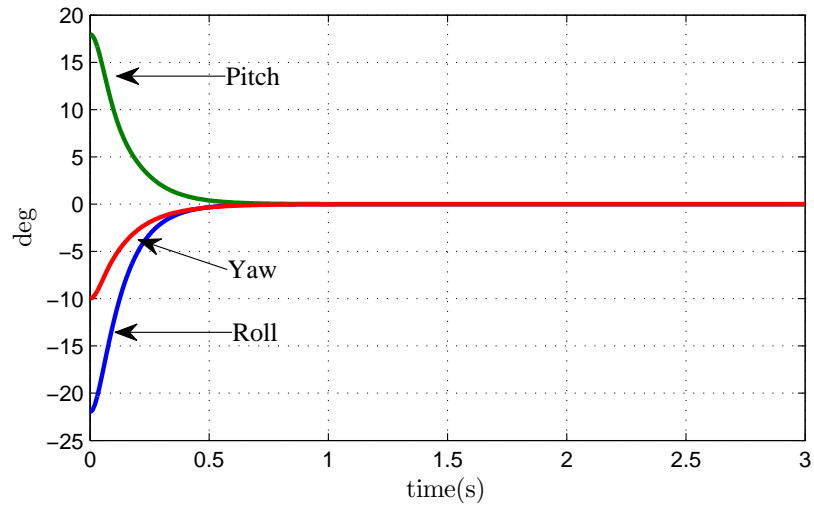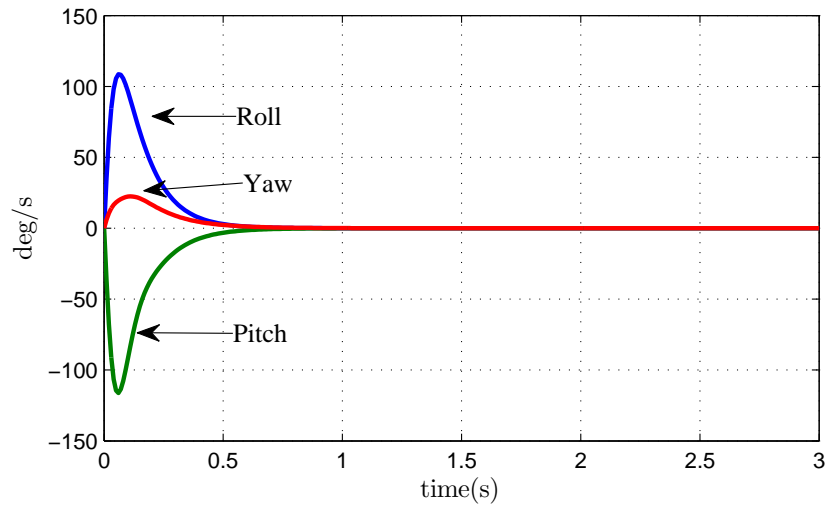Figure 6.8: Attitude control with standard velocity-free approach

Figure 6.9: Comparison of auxiliary velocity and angular velocity with standard velocity-free approach

(a) Attitude in Euler angles

(b) Angular velocity

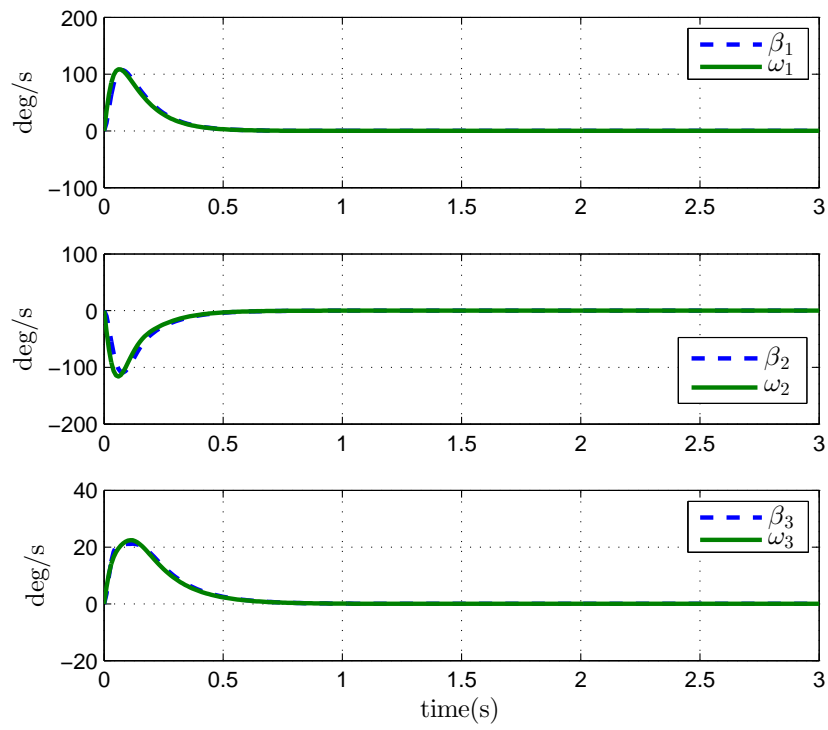Figure 6.10: Attitude control with improved velocity-free approach

Figure 6.11: Comparison of auxiliary velocity and angular velocity with improved velocity-free approach

Chapter 7

Conclusion

In this thesis, a quadrotor control system based on low-cost microprocessor and sensors, has been developed. A method for determining the moment of inertia of the quadrotor platform was proposed by applying the attitude estimation algorithm for data collecting and the fast Fourier transform for data analyzing. A method for the calibration of the propeller efficiency was introduced to reduce the horizontal translation while hovering.

A nonlinear attitude estimator known as the conditioned complementary filter was tested in our real-time embedded system. In the presence of measurement noise from the IMUs and the magnetic field distortion, the nonlinear estimator still works well in our quadrotor platform. A PD-like unit quaternion based attitude controller was implemented and found to perform well in our indoor environment.

The technique of vector decoupling was introduced to improve the performances of inertial measurements based attitude controller. This controller guarantees almost-global asymptotic stability without the attitude estimation algorithm. The obtained experimental results show acceptable performance with careful vector measurement filtering.

Finally, we applied some linear system analysis methods to discuss the implementation issues of the inertial measurement based velocity-free controller. An improvement has been proposed to increase the response speed of the quadrotor system.

Development of a reliable and robust quadrotor platform is the main purpose of this project. We list below some specific research work based on the work presented in this thesis below.

- *Global asymptotic stability*
  Due to the topological obstruction in attitude control, there does not exist any smooth controller that guarantees global asymptotic stability. Some new approaches using hybrid control have been developed recently, which achieve global asymptotic stability. However, these results have been tested only in simulations and robustness with respect to uncertainties and disturbances has not been considered. We would like to improve our inertial measurements based controller such that global asymptotic sta-

bility is guaranteed.

- *Position control and Trajectory tracking*
  We would like to develop and implement some trajectory tracking control schemes, with the help of GPS and/or vision system. With the trajectory tracking schemes, the quadrotor can navigate autonomously, without any user intervention, or execute high-level commands.

- *Multiple UAVs formation*
  Multiple autonomous quadrotor UAVs are more suitable for the execution of challenging missions. Formation control is one of the most important research topics in this area. Obviously, the multi-UAVs formation relies on efficient individual quadrotor control methods and specific techniques for multi-agent motion coordination.

Appendix A

Discrete Version of Attitude Estimation

The exponential of a matrix A is defined as follows

$$\exp(A) = \sum_{k=0}^{\infty} \frac{A^k}{k!} = I + A + \frac{A^2}{2!} + \frac{A^3}{3!} + \frac{A^4}{4!} + \frac{A^5}{5!} + \cdots$$

Using the fact that $A(\hat{\omega}_k)^2 = -\|\hat{\omega}_k\|^2 I_4$, one obtains that

$$
\begin{aligned}
\exp\left(\frac{T}{2}A(\hat{\omega}_k)\right) &= I_4 + \left(\frac{T}{2}A(\hat{\omega}_k)\right) + \frac{\left(\frac{T}{2}A(\hat{\omega}_k)\right)^2}{2!} + \frac{\left(\frac{T}{2}A(\hat{\omega}_k)\right)^3}{3!} + \frac{\left(\frac{T}{2}A(\hat{\omega}_k)\right)^4}{4!} + \\
&\quad \frac{\left(\frac{T}{2}A(\hat{\omega}_k)\right)^5}{5!} + \frac{\left(\frac{T}{2}A(\hat{\omega}_k)\right)^6}{6!} + \frac{\left(\frac{T}{2}A(\hat{\omega}_k)\right)^7}{7!} + \cdots \\
&= \left(I_4 + \frac{\left(\frac{T}{2}A(\hat{\omega}_k)\right)^2}{2!} + \frac{\left(\frac{T}{2}A(\hat{\omega}_k)\right)^4}{4!} + \frac{\left(\frac{T}{2}A(\hat{\omega}_k)\right)^6}{6!} + \cdots\right) + \\
&\quad \left(\left(\frac{T}{2}A(\hat{\omega}_k)\right) + \frac{\left(\frac{T}{2}A(\hat{\omega}_k)\right)^3}{3!} + \frac{\left(\frac{T}{2}A(\hat{\omega}_k)\right)^5}{5!} + \frac{\left(\frac{T}{2}A(\hat{\omega}_k)\right)^7}{7!} + \cdots\right) \\
&= \left(I_4 + \frac{\left(\frac{T}{2}A(\hat{\omega}_k)\right)^2}{2!} + \frac{\left(\frac{T}{2}A(\hat{\omega}_k)\right)^4}{4!} + \frac{\left(\frac{T}{2}A(\hat{\omega}_k)\right)^6}{6!} + \cdots\right) + \\
&\quad \left(I_4 + \frac{\left(\frac{T}{2}A(\hat{\omega}_k)\right)^2}{3!} + \frac{\left(\frac{T}{2}A(\hat{\omega}_k)\right)^4}{5!} + \frac{\left(\frac{T}{2}A(\hat{\omega}_k)\right)^6}{7!} + \cdots\right)\left(\frac{T}{2}A(\hat{\omega}_k)\right) \\
&= \left(I_4 - \frac{\left(\frac{T}{2}\|\hat{\omega}_k\|\right)^2}{2!}I_4 + \frac{\left(\frac{T}{2}\|\hat{\omega}_k\|\right)^4}{4!}I_4 - \frac{\left(\frac{T}{2}\|\hat{\omega}_k\|\right)^6}{6!}I_4 + \cdots\right) + \\
&\quad \left(I_4 - \frac{\left(\frac{T}{2}\|\hat{\omega}_k\|\right)^2}{3!}I_4 + \frac{\left(\frac{T}{2}\|\hat{\omega}_k\|\right)^4}{5!}I_4 - \frac{\left(\frac{T}{2}\|\hat{\omega}_k\|\right)^6}{7!}I_4 + \cdots\right)\left(\frac{T}{2}A(\hat{\omega}_k)\right)
\end{aligned}
$$

Using the facts that

$$\sin x = \sum_{n=0}^{\infty} \frac{(-1)^n}{(2n+1)!} x^{2n+1} = x - \frac{x^3}{3!} + \frac{x^5}{5!} - \frac{x^7}{7!} + \cdots$$

and

$$\cos x = \sum_{n=0}^{\infty} \frac{(-1)^n}{(2n)!} x^{2n} = 1 - \frac{x^2}{2!} + \frac{x^4}{4!} - \frac{x^6}{6!} + \cdots$$

one has

$$\exp\left(\frac{T}{2} A(\hat{\omega}_k)\right) = \cos\left(\frac{T}{2}\|\hat{\omega}_k\|\right) I_4 + \frac{T}{2}\operatorname{sinc}\left(\frac{T}{2}\|\hat{\omega}_k\|\right) A(\hat{\omega}_k) \tag{A.1}$$

where

$$\operatorname{sinc}(x) = \sum_{n=0}^{\infty} \frac{(-1)^n}{(2n+1)!} x^{2n} = 1 - \frac{x^2}{3!} + \frac{x^4}{5!} - \frac{x^6}{7!} + \cdots$$

Consequently, the following discrete version of observer (4.7) is proposed:

$$\hat{Q}_{k+1} = \left(\cos\left(\frac{T}{2}\|\hat{\omega}_k\|\right) I_4 + \frac{T}{2}\operatorname{sinc}\left(\frac{T}{2}\|\hat{\omega}_k\|\right) A(\hat{\omega}_k)\right) \hat{Q}_k \tag{A.2}$$

Specially, if $\|\hat{\omega}_k\| \neq 0$, one has

$$\hat{Q}_{k+1} = \left(\cos\left(\frac{T}{2}\|\hat{\omega}_k\|\right) I_4 + \sin\left(\frac{T}{2}\|\hat{\omega}_k\|\right) A(\bar{\omega}_k)\right) \hat{Q}_k \tag{A.3}$$

where, $\hat{\omega}_k = \bar{\omega}_k\|\hat{\omega}_k\|$, then matrix $\exp\left(\frac{T}{2}A(\hat{\omega}_k)\right)$ can be also represented by an unit Quaternion

$$Q_{\bar{\omega}_k} = \left[\cos\left(\frac{T\|\hat{\omega}_k\|}{2}\right) \quad \sin\left(\frac{T\|\hat{\omega}_k\|}{2}\right) \bar{\omega}_k^\top\right]^\top \tag{A.4}$$

Finally, the quaternion at time $(k+1)T$ can be expressed as

$$\hat{Q}_{k+1} = \begin{cases} Q_{\bar{\omega}_k} \otimes \hat{Q}_k, & \text{if } \|\hat{\omega}_k\| \neq 0 \\ \hat{Q}_k, & \text{if } \|\hat{\omega}_k\| = 0 \end{cases} \tag{A.5}$$

which theoretically guarantees $\hat{Q}_{k+1}$ unit Quaternion (see details in [72]).

Appendix B

Discrete Version of Inertial Vector Integration

Using the fact

$$(-TS(\hat{\omega}_{\mathcal{B}_k}))^2 = T^2 \hat{w}_{\mathcal{B}_k} \hat{w}_{\mathcal{B}_k}^\top - \|T\hat{w}_{\mathcal{B}_k}\|^2 I_3$$

and

$$(-TS(\hat{\omega}_{\mathcal{B}_k}))^3 = -\|T\hat{w}_{\mathcal{B}_k}\|^2 (-TS(\hat{\omega}_{\mathcal{B}_k}))$$

the exponential of $-TS(\hat{\omega}_{\mathcal{B}_k})$ is given by

$$
\begin{aligned}
\exp\left(-TS(\hat{\omega}_{\mathcal{B}_k})\right) &= I_3 + (-TS(\hat{\omega}_{\mathcal{B}_k})) + \frac{(-TS(\hat{\omega}_{\mathcal{B}_k}))^2}{2!} + \frac{(-TS(\hat{\omega}_{\mathcal{B}_k}))^3}{3!} + \frac{(-TS(\hat{\omega}_{\mathcal{B}_k}))^4}{4!} + \\
&\quad \frac{(-TS(\hat{\omega}_{\mathcal{B}_k}))^5}{5!} + \frac{(-TS(\hat{\omega}_{\mathcal{B}_k}))^6}{6!} + \frac{(-TS(\hat{\omega}_{\mathcal{B}_k}))^7}{7!} + \frac{(-TS(\hat{\omega}_{\mathcal{B}_k}))^8}{8!} + \cdots \\
&= I_3 - TS(\hat{\omega}_{\mathcal{B}_k}) + \frac{(TS(\hat{\omega}_{\mathcal{B}_k}))^2}{2!} + \|T\hat{\omega}_{\mathcal{B}_k}\|^2 \frac{TS(\hat{\omega}_{\mathcal{B}_k})}{3!} - \|T\hat{\omega}_{\mathcal{B}_k}\|^2 \frac{(TS(\hat{\omega}_{\mathcal{B}_k}))^2}{4!} \\
&\quad -\|T\hat{\omega}_{\mathcal{B}_k}\|^4 \frac{TS(\hat{\omega}_{\mathcal{B}_k})}{5!} + \|T\hat{\omega}_{\mathcal{B}_k}\|^4 \frac{(TS(\hat{\omega}_{\mathcal{B}_k}))^2}{6!} + \|T\hat{\omega}_{\mathcal{B}_k}\|^6 \frac{TS(\hat{\omega}_{\mathcal{B}_k})}{7!} \\
&\quad -\|T\hat{\omega}_{\mathcal{B}_k}\|^6 \frac{(TS(\hat{\omega}_{\mathcal{B}_k}))^2}{8!} + \cdots \\
&= I_3 + \left(1 - \frac{\|T\hat{\omega}_{\mathcal{B}_k}\|^2}{3!} + \frac{T\|\hat{\omega}_{\mathcal{B}_k}\|^4}{5!} - \frac{T\|\hat{\omega}_{\mathcal{B}_k}\|^6}{7!} + \cdots \right)(-TS(\hat{\omega}_{\mathcal{B}_k})) + \\
&\quad \left(\frac{1}{2!} - \frac{\|T\hat{\omega}_{\mathcal{B}_k}\|^2}{4!} + \frac{\|T\hat{\omega}_{\mathcal{B}_k}\|^4}{6!} - \frac{\|T\hat{\omega}_{\mathcal{B}_k}\|^6}{8!} + \cdots \right)(-TS(\hat{\omega}_{\mathcal{B}_k}))^2 \\
&= I_3 + \text{sinc}(\|T\hat{\omega}_{\mathcal{B}_k}\|)(-TS(\hat{\omega}_{\mathcal{B}_k})) + \text{cosc}(T\|\hat{\omega}_{\mathcal{B}_k}\|)(-TS(\hat{\omega}_{\mathcal{B}_k}))^2 \\
&= I_3 - T\text{sinc}(\Theta)S(\hat{\omega}_{\mathcal{B}_k}) + T^2 \text{cosc}(\Theta)(S(\hat{\omega}_{\mathcal{B}_k}))^2 \quad\quad\quad\text{(B.1)}
\end{aligned}
$$

where, $\Theta = T\|\hat{\omega}_{\mathcal{B}_k}\|$ and

$$
\begin{aligned}
\text{sinc}(x) &= \frac{\sin(x)}{x} = 1 - \frac{x^2}{3!} + \frac{x^4}{5!} - \frac{x^7}{7!} + \cdots \\
\text{cosc}(x) &= \frac{1 - \cos(x)}{x^2} = \frac{1}{2!} - \frac{x^2}{4!} + \frac{x^4}{6!} - \frac{x^6}{8!} + \cdots
\end{aligned}
$$

The expansion of the exponential matrix $\exp(-TS(\hat{\omega}_{\mathcal{B}_k}))$ is given by

$$\exp(-TS(\hat{\omega}_{\mathcal{B}_k})) = \begin{bmatrix} 1 - \Theta^2 c\Theta + \hat{\omega}_{k_x}^2 c\Theta & \hat{\omega}_{k_x}\hat{\omega}_{k_y}c\Theta + \hat{\omega}_{k_z}s\Theta & -\hat{\omega}_{k_y}s\Theta + \hat{\omega}_{k_x}\hat{\omega}_{k_z}c\Theta \\ -\hat{\omega}_{k_z}s\Theta + \hat{\omega}_{k_x}\hat{\omega}_{k_y}c\Theta & 1 - \Theta^2 c\Theta + \hat{\omega}_{k_y}^2 c\Theta & \hat{\omega}_{k_y}\hat{\omega}_{k_z}c\Theta + \hat{\omega}_{k_x}s\Theta \\ \hat{\omega}_{k_x}\hat{\omega}_{k_z}c\Theta + \hat{\omega}_{k_y}s\Theta & -\hat{\omega}_{k_x}s\Theta + \hat{\omega}_{k_y}\hat{\omega}_{k_z}c\Theta & 1 - \Theta^2 c\Theta + \hat{\omega}_{k_z}^2 c\Theta \end{bmatrix} \tag{B.2}$$

where, $\hat{\omega}_{\mathcal{B}_k} = [\hat{\omega}_{k_x}, \hat{\omega}_{k_y}, \hat{\omega}_{k_z}]^\top$, and c and s denoting the cosine and sine operators.

Appendix C

Magnetometer Calibration

A novel compensation approach proposed in [66] and [67] has been implemented in our thesis. Without the effect of white noise, the magnetic measurement can be simplified as

$$m_{\mathcal{B}} = DR^\top m_{\mathcal{I}} + b_m \tag{C.1}$$

where, R is the notation matrix, D is the distortion, $m_{\mathcal{I}}$ denotes the Earth's magnetic field vector (expressed in the inertial frame), b_m is a body-fixed frame expression for the local magnetic disturbance, and n_m denotes the measurement noise. The D and b_m are given by

$$D = \begin{bmatrix} \epsilon_x & 0 & 0 \\ \epsilon_y \sin \delta_x & \epsilon_y \cos \delta_x & 0 \\ \epsilon_z \sin \delta_y \cos \delta_z & \epsilon_z \sin \delta_z & \epsilon_z \cos \delta_y \cos \delta_z \end{bmatrix} \qquad b_m = \begin{bmatrix} \varrho_x \\ \varrho_y \\ \varrho_z \end{bmatrix}$$

where, $(\epsilon_x, \epsilon_y, \epsilon_z)$ are the total scale errors on the x, y, and z axes respectively, $(\delta_x, \delta_y, \delta_z)$ are the sensor misalignment angles between the sensor measurements and body axes, and $(\varrho_x, \varrho_y, \varrho_z)$ are the sensor offsets between the sensor measurements and body axes. One can solve the equation (C.1) for $R^\top m_{\mathcal{I}}$ as

$$R^\top m_{\mathcal{I}} = D^{-1}(m_{\mathcal{B}} - b_m) \tag{C.2}$$

It is easy to calculate the inverse of matrix D, which is given by

$$D^{-1} = \begin{bmatrix} D_1 & 0 & 0 \\ D_2 & D_3 & 0 \\ D_4 & D_5 & D_6 \end{bmatrix}$$

and the coefficients $D_1 - D_5$ denote

$$D_1 = \frac{1}{\epsilon_x}$$

$$D_2 = -\frac{\tan \delta_x}{\epsilon_x}$$

$$D_3 = \frac{1}{\epsilon_y \cos \delta_x}$$

$$D_4 = \frac{\tan \delta_x \tan \delta_z}{\epsilon_x \cos \delta_y} - \frac{\tan \delta_y}{\epsilon_x}$$

$$D_5 = -\frac{\tan \delta_z}{\epsilon_y \cos \delta_x \cos \delta_y}$$

$$D_6 = \frac{1}{\epsilon_z \cos \delta_y \cos \delta_z}$$

Using the fact $m_{\mathcal{B}} = [m_{\mathcal{B}_x}, m_{\mathcal{B}_y}, m_{\mathcal{B}_z}]^{\top}$, one can further rewrite (C.2) as

$$R^{\top} m_{\mathcal{I}} = \begin{bmatrix} D_1(m_{\mathcal{B}_x} - \varrho_x) \\ D_2(m_{\mathcal{B}_x} - \varrho_x) + D_3(m_{\mathcal{B}_y} - \varrho_y) \\ D_4(m_{\mathcal{B}_x} - \varrho_x) + D_5(m_{\mathcal{B}_y} - \varrho_y) + D_6(m_{\mathcal{B}_z} - \varrho_z) \end{bmatrix} \tag{C.3}$$

Since $\|R^{\top} m_{\mathcal{I}}\|^2 = \|m_{\mathcal{I}}\|^2$, one can rearrange (C.3) as follows

$$C_1 m_{\mathcal{B}_x}^2 + C_2 m_{\mathcal{B}_x} m_{\mathcal{B}_y} + C_3 m_{\mathcal{B}_x} m_{\mathcal{B}_z} + C_4 m_{\mathcal{B}_y}^2 + C_5 m_{\mathcal{B}_y} m_{\mathcal{B}_z}$$
$$+ C_6 m_{\mathcal{B}_z}^2 + C_7 m_{\mathcal{B}_x} + C_8 m_{\mathcal{B}_y} + C_9 m_{\mathcal{B}_z} = C_{10} \tag{C.4}$$

with

$$C_1 = D_1^2 + D_2^2 + D_4^2$$
$$C_2 = 2D_2 D_3 + 2D_4 D_5$$
$$C_3 = 2D_4 D_6$$
$$C_4 = D_3^2 + D_5^2$$
$$C_5 = 2D_5 D_6$$
$$C_6 = D_6^2$$
$$C_7 = -2\varrho_x(D_1^2 + D_2^2 + D_4^2) - 2(D_2 D_3 + D_4 D_5)\varrho_y - 2D_4 D_6 \varrho_z$$
$$C_8 = -2\varrho_y(D_3^2 + D_5^2) - 2(D_2 D_3 + D_4 D_5)\varrho_x - 2D_5 D_6 \varrho_z$$
$$C_9 = -2\varrho_z D_6^2 - 2D_4 D_6 \varrho_x - 2D_5 D_6 \varrho_y$$
$$C_{10} = \|m_{\mathcal{I}}\|^2 - (D_1^2 + D_2^2 + D_4^2)\varrho_x^2 - (D_3^2 + D_5^2)\varrho_y^2 - D_6^2 \varrho_z^2 + 2(D_1 + D_2 + D_3)\varrho_x$$
$$+ 2(D_3 + D_5)\varrho_y + 2D_6 \varrho_z - 2(D_2 D_3 + D_4 D_5)\varrho_x \varrho_y - 2D_4 D_6 \varrho_x \varrho_z - 2D_5 D_6 \varrho_y \varrho_z$$

where, the coefficients C_k, $1 \leq k \leq 10$ are the functions of the 10 parameters $\epsilon_i, \delta_i, \varrho_i, i \in \{x, y, z\}$ and $\|m_{\mathcal{I}}\|$. One can further rewrite (C.4) as

$$\frac{C_1}{C_{10}} m_{\mathcal{B}_x}^2 + \frac{C_2}{C_{10}} m_{\mathcal{B}_x} m_{\mathcal{B}_y} + \frac{C_3}{C_{10}} m_{\mathcal{B}_x} m_{\mathcal{B}_z} + \frac{C_4}{C_{10}} m_{\mathcal{B}_y}^2 + \frac{C_5}{C_{10}} m_{\mathcal{B}_y} m_{\mathcal{B}_z} + \frac{C_6}{C_{10}} m_{\mathcal{B}_z}^2$$
$$+ \frac{C_7}{C_{10}} m_{\mathcal{B}_x} + \frac{C_8}{C_{10}} m_{\mathcal{B}_y} + \frac{C_9}{C_{10}} m_{\mathcal{B}_z} = 1 \tag{C.5}$$

The magnetometer data set $\{m_{\mathcal{B}}\}$ consisting of N data points (at least 1000 samples) can be collected by rotating the quadrotor along all the axes, and recorded them using the serial communication. Then (C.5) with N samples can be rewritten into a large matrix as

$$\mathbb{X}\mathbb{C} = \mathbb{W} \tag{C.6}$$

where

$$\mathbb{X} = \underbrace{\begin{bmatrix} m_{\mathcal{B}_{x1}}^2 & m_{\mathcal{B}_{x1}}m_{\mathcal{B}_{y1}} & \cdots & m_{\mathcal{B}_{z1}} \\ m_{\mathcal{B}_{x2}}^2 & m_{\mathcal{B}_{x2}}m_{\mathcal{B}_{y2}} & \cdots & m_{\mathcal{B}_{z2}} \\ \vdots & \vdots & \ddots & \vdots \\ m_{\mathcal{B}_{xN}}^2 & m_{\mathcal{B}_{xN}}m_{\mathcal{B}_{yN}} & \cdots & m_{\mathcal{B}_{zN}} \end{bmatrix}}_{N \times 9} \quad \mathbb{C} = \underbrace{\begin{bmatrix} C_1/C_{10} \\ C_2/C_{10} \\ \vdots \\ C_9/C_{10} \end{bmatrix}}_{9 \times 1} \quad \mathbb{W} = \underbrace{\begin{bmatrix} 1 \\ 1 \\ \vdots \\ 1 \end{bmatrix}}_{N \times 1}$$

Finally, $\mathbb{C}_{est}$, a least-squares best fit estimate for $\mathbb{C}$, can be generated as

$$\mathbb{C}_{est} = (\mathbb{X}^\top \mathbb{X})^{-1} \mathbb{X}^\top \mathbb{W} \tag{C.7}$$

Now that the estimates for $\mathbb{C}$ have been found. The earth magnetic field $m_{\mathcal{I}}$ at the current location can be obtained from the Inertial Geomagnetic Reference Field (IGRF) [73] or World Magnetic Model (WMM) [74]. For example, the earth magnetic field in Thunder Bay, Ontario, Canada is given by $(0.1550, -0.0101, 0.5453)^\top$ gauss. It is easy to have that $\|m_{\mathcal{I}}\| = 0.5670$. Using the local value of $\|m_{\mathcal{I}}\|$, solutions for nine parameters $\epsilon_i, \delta_i, \varrho_i, i \in \{x, y, z\}$ can be solved from nine nonlinear equations (C.7) algebraically. The gradient descent method with MATLAB can be used to solve the nine nonlinear equations.

Bibliography

[1] S. Lupashin, M. Hehn, M. W. Mueller, A. P. Schoellig, M. Sherback, and R. DAndrea, "A platform for aerial robotics research and demonstration: The flying machine arena," *Mechatronics*, vol. 24, no. 1, pp. 41–54, 2014.

[2] G. Mohanarajah, D. Hunziker, R. D'Andrea, and M. Waibel, "Rapyuta: A cloud robotics platform," *Automation Science and Engineering, IEEE Transactions on*, vol. 12, no. 2, pp. 481–493, 2015.

[3] J. L. Crassidis, F. L. Markley, and Y. Cheng, "Survey of nonlinear attitude estimation methods," *Journal of Guidance, Control, and Dynamics*, vol. 30, no. 1, pp. 12–28, 2007.

[4] M. Zamani, J. Trumpf, and R. Mahony, "Nonlinear attitude filtering: A comparison study," *arXiv preprint* arXiv:1502.03990, 2015.

[5] G. Wahba, "A least squares estimate of satellite attitude," *SIAM review*, vol. 7, no. 3, pp. 409–409, 1965.

[6] M. D. Shuster and S. Oh, "Three-axis attitude determination from vector observations," *Journal of Guidance, Control, and Dynamics*, vol. 4, no. 1, pp. 70–77, 1981.

[7] F. L. Markley, "Attitude determination using vector observations and the singular value decomposition," *The Journal of the Astronautical Sciences*, vol. 36, no. 3, pp. 245–258, 1988.

[8] S. F. Schmidt, "The Kalman filter - Its recognition and development for aerospace applications," *Journal of Guidance, Control, and Dynamics*, vol. 4, no. 1, pp. 4–7, 1981.

[9] J. L. Farrell, "Attitude determination by Kalman filtering," *Automatica*, vol. 6, no. 3, pp. 419–430, 1970.

[10] E. J. Lefferts, F. L. Markley, and M. D. Shuster, "Kalman filtering for spacecraft attitude estimation," *Journal of Guidance, Control, and Dynamics*, vol. 5, no. 5, pp. 417–429, 1982.

[11] F. L. Markley, "Attitude error representations for kalman filtering," *Journal of guidance, control, and dynamics*, vol. 26, no. 2, pp. 311–317, 2003.

[12] I. Bar-Itzhack and Y. Oshman, "Attitude determination from vector observations: quaternion estimation," *Aerospace and Electronic Systems, IEEE Transactions on*, vol. 321, no. 1, pp. 128–136, 1985.

[13] S. Salcudean, "A globally convergent angular velocity observer for rigid body motion," *Automatic Control, IEEE Transactions on*, vol. 36, no. 12, pp. 1493–1497, 1991.

[14] N. Metni, J.-M. Pflimlin, T. Hamel, and P. Souères, "Attitude and gyro bias estimation for a flying uav," in *Intelligent Robots and Systems, 2005.(IROS 2005). 2005 IEEE/RSJ International Conference on*, pp. 1114–1120, IEEE, 2005.

[15] T. Hamel and R. Mahony, "Attitude estimation on SO(3) based on direct inertial measurements," in *Robotics and Automation, 2006. ICRA 2006. Proceedings 2006 IEEE International Conference on*, pp. 2170–2175, IEEE, 2006.

[16] N. Metni, J.-M. Pflimlin, T. Hamel, and P. Souères, "Attitude and gyro bias estimation for a VTOL UAV," *Control Engineering Practice*, vol. 14, no. 12, pp. 1511–1520, 2006.

[17] A. Tayebi, S. McGilvray, A. Roberts, and M. Moallem, "Attitude estimation and stabilization of a rigid body using low-cost sensors," in *Decision and Control, 2007 46th IEEE Conference on*, pp. 6424–6429, IEEE, 2007.

[18] R. Mahony, T. Hamel, and J.-M. Pflimlin, "Nonlinear complementary filters on the special orthogonal group," *Automatic Control, IEEE Transactions on*, vol. 53, no. 5, pp. 1203–1218, 2008.

[19] R. Mahony, T. Hamel, J. Trumpf, and C. Lageman, "Nonlinear attitude observers on SO(3) for complementary and compatible measurements: A theoretical study," in *Decision and Control, 2009 held jointly with the 2009 28th Chinese Control Conference. CDC/CCC 2009. Proceedings of the 48th IEEE Conference on*, pp. 6407–6412, IEEE, 2009.

[20] P. Martin and E. Salaün, "Design and implementation of a low-cost observer-based attitude and heading reference system," *Control Engineering Practice*, vol. 18, no. 7, pp. 712–722, 2010.

[21] A. Tayebi, A. Roberts, and A. Benallegue, "Inertial measurements based dynamic attitude estimation and velocity-free attitude stabilization," in *American Control Conference (ACC), 2011*, pp. 1027–1032, IEEE, 2011.

[22] A. Roberts and A. Tayebi, "On the attitude estimation of accelerating rigid-bodies using GPS and IMU measurements," in *Decision and Control and European Control Conference (CDC-ECC), 2011 50th IEEE Conference on*, pp. 8088–8093, IEEE, 2011.

[23] M.-D. Hua, G. Ducard, T. Hamel, R. Mahony, and K. Rudin, "Implementation of a nonlinear attitude estimator for aerial robotic vehicles," *Control Systems Technology, IEEE Transactions on*, vol. 22, no. 1, pp. 201–213, 2014.

[24] M.-D. Hua, K. Rudin, G. Ducard, T. Hamel, and R. Mahony, "Nonlinear attitude estimation with measurement decoupling and anti-windup gyro-bias compensation," in *IFAC World Congress*, pp. 2972–2978, 2011.

[25] J.-Y. Wen and K. Kreutz-Delgado, "The attitude control problem," *Automatic Control, IEEE Transactions on*, vol. 36, no. 10, pp. 1148–1162, 1991.

[26] N. Chaturvedi, A. K. Sanyal, and N. H. McClamroch, "Rigid-body attitude control," *Control Systems Magazine, IEEE*, vol. 31, no. 3, pp. 30–51, 2011.

[27] R. Mahony, V. Kumar, and P. Corke, "Multirotor aerial vehicles: Modeling, estimation, and control of quadrotor," *IEEE Robotics and Automation Magazine*, no. 19, pp. 20–32, 2012.

[28] S. Bouabdallah, A. Noth, and R. Siegwart, "PID vs LQ control techniques applied to an indoor micro quadrotor," in *Intelligent Robots and Systems, 2004.(IROS 2004). Proceedings. 2004 IEEE/RSJ International Conference on*, vol. 3, pp. 2451–2456, IEEE, 2004.

[29] J. Li and Y. Li, "Dynamic analysis and PID control for a quadrotor," in *Mechatronics and Automation (ICMA), 2011 International Conference on*, pp. 573–578, IEEE, 2011.

[30] E. Reyes-Valeria, R. Enriquez-Caldera, S. Camacho-Lara, and J. Guichard, "LQR control for a quadrotor using unit quaternions: Modeling and simulation," in *Electronics, Communications and Computing (CONIELECOMP), 2013 International Conference on*, pp. 172–178, IEEE, 2013.

[31] M. Faessler, F. Fontana, C. Forster, E. Mueggler, M. Pizzoli, and D. Scaramuzza, "Autonomous, vision-based flight and live dense 3d mapping with a quadrotor micro aerial vehicle," *Journal of Field Robotics*, 2015.

[32] A. Benallegue, A. Mokhtari, and L. Fridman, "Feedback linearization and high order sliding mode observer for a quadrotor UAV," in *Variable Structure Systems, 2006. VSS'06. International Workshop on*, pp. 365–372, IEEE, 2006.

[33] I. Voos, "Nonlinear control of a quadrotor micro-UAV using feedback-linearization," in *Mechatronics, 2009. ICM 2009. IEEE International Conference on*, pp. 1–6, IEEE, 2009.

[34] D. Lee, H. J. Kim, and S. Sastry, "Feedback linearization vs. adaptive sliding mode control for a quadrotor helicopter," *International Journal of control, Automation and systems*, vol. 7, no. 3, pp. 419–428, 2009.

[35] S. Bouabdallah and R. Siegwart, "Backstepping and sliding-mode techniques applied to an indoor micro quadrotor," in *Robotics and Automation, 2005. ICRA 2005. Proceedings of the 2005 IEEE International Conference on*, pp. 2247–2252, IEEE, 2005.

[36] T. Madani and A. Benallegue, "Backstepping control for a quadrotor helicopter," in *Intelligent Robots and Systems, 2006 IEEE/RSJ International Conference on*, pp. 3255–3260, IEEE, 2006.

[37] Y.-C. Choi and H.-S. Ahn, "Nonlinear control of quadrotor for point tracking: Actual implementation and experimental tests," *Mechatronics, IEEE/ASME Transactions on*, vol. 20, no. 3, pp. 1179–1192, 2015.

[38] F. Goodarzi, D. Lee, and T. Lee, "Geometric nonlinear PID control of a quadrotor UAV on SE(3)," in *Control Conference (ECC), 2013 European*, pp. 3845–3850, IEEE, 2013.

[39] A. Tayebi and S. McGilvray, "Attitude stabilization of a VTOL quadrotor aircraft," *Control Systems Technology, IEEE Transactions on*, vol. 14, no. 3, pp. 562–571, 2006.

[40] F. Lizarralde and J. T. Wen, "Attitude control without angular velocity measurement: A passivity approach," *Automatic Control, IEEE Transactions on*, vol. 41, no. 3, pp. 468–472, 1996.

[41] P. Tsiotras, "Further passivity results for the attitude control problem," *IEEE Transactions on Automatic Control*, vol. 43, no. 11, pp. 1597–1600, 1998.

[42] M. R. Akella, "Rigid body attitude tracking without angular velocity feedback," *Systems & Control Letters*, vol. 42, no. 4, pp. 321–326, 2001.

[43] A. Tayebi, "Unit quaternion-based output feedback for the attitude tracking problem," *Automatic Control, IEEE Transactions on*, vol. 53, no. 6, pp. 1516–1520, 2008.

[44] A. Tayebi, A. Roberts, and A. Benallegue, "Inertial vector measurements based velocity-free attitude stabilization," *Automatic Control, IEEE Transactions on*, vol. 58, no. 11, pp. 2893–2898, 2013.

[45] D. Thakur and M. R. Akella, "Gyro-free rigid-body attitude stabilization using only vector measurements," *Journal of Guidance, Control, and Dynamics*, vol. 38, no. 4, pp. 811–818, 2014.

[46] L. Benziane, A. Benallegue, and A. Tayebi, "Attitude stabilization without angular velocity measurements," in *Robotics and Automation (ICRA), 2014 IEEE International Conference on*, pp. 3116–3121, IEEE, 2014.

[47] L. Benziane, A. Benallegue, Y. Chitour, and A. Tayebi, "Velocity-free attitude stabilization with inertial vector measurements," *International Journal of Robust and Nonlinear Control*, in press, 2015.

[48] M. D. Shuster, "A survey of attitude representations," *Navigation*, vol. 8, no. 9, pp. 439–517, 1993.

[49] P. Singla, D. Mortari, and J. L. Junkins, "How to avoid singularity for Euler angle set?," in *Proceedings of the AAS Space Flight Mechanics Conference, Hawaii*, 2004.

[50] J. Diebel, "Representing attitude: Euler angles, unit quaternions, and rotation vectors," *Matrix*, vol. 58, pp. 15–16, 2006.

[51] S. P. Bhat and D. S. Bernstein, "A topological obstruction to continuous global stabilization of rotational motion and the unwinding phenomenon," *Systems & Control Letters*, vol. 39, no. 1, pp. 63–70, 2000.

[52] T. Hamel, R. Mahony, R. Lozano, and J. Ostrowski, "Dynamic modeling and configuration stabilization for an X4-flyer," *Proceedings of the 15th IFAC World Congress*, vol. 15, no. 1, pp. 846–846, 2002.

[53] R. Mahony and T. Hamel, "Adaptive compensation of aerodynamic effects during takeoff and landing manoeuvres for a scale model autonomous helicopter," *European Journal of Control*, vol. 7, no. 1, pp. 43–57, 2001.

[54] P. E. Crouch, "Spacecraft attitude control and stabilization: Applications of geometric control theory to rigid body models," *Automatic Control, IEEE Transactions on*, vol. 29, no. 4, pp. 321–331, 1984.

[55] H. Lim, J. Park, D. Lee, and H. J. Kim, "Build your own quadrotor: Open-source projects on unmanned aerial vehicles," *Robotics and Automation Magazine, IEEE*, vol. 19, no. 3, pp. 33–45, 2012.

[56] [Online]. http://copter.ardupilot.com/.

[57] [Online]. http://3drobotics.com/.

[58] Datasheet: Atmel ATmega2560. http://www.atmel.com/.

[59] Datasheet: Atmel ATmega32U2. http://www.atmel.com/.

[60] Datasheet: Invensense MPU-6000.

[61] Datasheet: Honeywell HMC5883l.

[62] B. Mccormick, *Aerodynamics, Aeronautics, and Flight Mechanics.* Wiley, Second Edition, 1995.

[63] J. G. Leishman, *Principles of Helicopter Aerodynamics with CD Extra.* Cambridge, U.K: Cambridge Univ. Press., 2006.

[64] [Online]. http://m-selig.ae.illinois.edu/props/volume-1/propDB-volume-1.html.

[65] S. J. McGilvray, "Attitude stabilization of a quadrotor aircraft," Master's thesis, Lakehead University, 2007.

[66] C. C. Foster and G. H. Elkaim, "Extension of a two-step calibration methodology to include nonorthogonal sensor axes," *Aerospace and Electronic Systems, IEEE Transactions on*, vol. 44, no. 3, pp. 1070–1078, 2008.

[67] M. Barczyk, *Nonlinear state estimation and modeling of a helicopter UAV*. PhD thesis, University of Alberta, 2012.

[68] [Online]. http://copter.ardupilot.com/wiki/esc-calibration/.

[69] H. K. Khalil and J. Grizzle, *Nonlinear systems*, vol. 3. Prentice hall New Jersey, 1996.

[70] J. Gallier and D. Xu, "Computing exponentials of skew-symmetric matrices and logarithms of orthogonal matrices," *International Journal of Robotics and Automation*, vol. 17, no. 4, 2002.

[71] A. Tayebi, "Correction to "inertial vectors measurements based velocity-free attitude stabilization "," *under preparation*, 2015.

[72] F. Zhao and B. van Wachem, "A novel quaternion integration approach for describing the behaviour of non-spherical particles," *Acta Mechanica*, vol. 224, no. 12, pp. 3091–3109, 2013.

[73] C. Finlay, S. Maus, C. Beggan, T. Bondar, A. Chambodut, T. Chernova, A. Chulliat, V. Golovkov, B. Hamilton, M. Hamoudi, *et al.*, "International geomagnetic reference field: the eleventh generation," *Geophysical Journal International*, vol. 183, no. 3, pp. 1216–1230, 2010.

[74] S. Maus, S. Macmillan, S. McLean, B. Hamilton, A. Thomson, M. Nair, and C. Rollins, "The US/UK world magnetic model for 2010-2015," *NOAA Technical Report NESDIS/NGDC*, 2010.